Dissertation
submitted to the
Combined Faculties of the Natural Sciences and for Mathematics
of the Ruperto-Carola University of Heidelberg, Germany
for the degree of
Doctor of Natural Sciences

Put forward by
Dipl.-Phys. Christoph S. Hofmann
Born in Freiburg im Breisgau, Germany
Oral examination: February 6th, 2013

Emergence of correlations in strongly interacting ultracold Rydberg gases

Referees:	**Prof. Dr. Matthias Weidemüller**
	Prof. Dr. Markus Oberthaler

Zusammenfassung:

Diese Doktorarbeit untersucht die experimentelle Anwendung stark wechselwirkender Rydberg-Atome als Mittel zur Erzeugung und zur Kontrolle von Korrelationen in Vielteilchensystemen. Eine neue Apparatur wurde gebaut, die die Erzielung hoher atomarer Dichten mittels Dipolfallen mit der Rydberg-Atom-Detektion sowohl durch Feldionisation als auch durch optische Untersuchung mittels elektromagnetisch induzierter Transparenz kombiniert. In der ersten Studie wird die wechselwirkungsinduzierte Anregung („Antiblockade“) von Rydberg-Atompaaren durch verstimmte Laseranregung gezeigt. Dies ermöglicht das Maßschneidern räumlicher Korrelationen und die Kontrolle von Wechselwirkungen zwischen Rydberg-Atomen. Anschließend werden die Auswirkungen von Rydberg–Rydberg-Wechselwirkungen und Korrelationen auf die spontane Evolution des Systems in ein ultrakaltes Plasma untersucht. Dabei sollten die anfänglichen Korrelationen zwischen den Rydberg-Atomen erhalten bleiben, was eine neue Möglichkeit zur Überwindung des unordnungsinduzierten Plasmaheizens und zur Realisierung neuartiger stark gekoppelter Plasmaregime bieten könnte. Abschließend wird die Rückwirkung von Rydberg–Rydberg-Wechselwirkungen auf propagierende Lichtfelder untersucht. Dissipative Wechselwirkungen zwischen Dunkelzustandspolaritonen haben ein stark nichtlineares optisches Verhalten und eine nicht-Poissonsche Statistik zur Folge, die die Emergenz von Korrelationen in atomaren Feldern und in Lichtfeldern widerspiegeln. Die Kombination dieser Experimente beleuchtet die Auswirkung von durch Rydberg-Wechselwirkungen hervorgerufenen Korrelationen auf verschiedenartige physikalische Systeme wie Atome, Ionen und Photonen.

Abstract:

This thesis experimentally explores the application of strongly interacting states of Rydberg atoms as means to introduce and control correlations in many-body systems. A new apparatus has been built, which combines high atomic densities possible using optical dipole traps with the ability to detect and probe Rydberg atoms via both field ionization detection and electromagnetically induced transparency. In the first study, the interaction induced excitation of Rydberg atom pairs (‘antiblockade’) is demonstrated using detuned laser excitation. This provides the possibility to engineer spatial correlations and to control interactions between Rydberg atoms. We then investigate the effects of Rydberg–Rydberg interactions and correlations on the spontaneous evolution of the system to an ultracold plasma. The initial correlations between Rydberg atoms should be preserved, suggesting a new route to overcome disorder-induced heating and to enter new strongly coupled regimes. Finally the back-action of Rydberg–Rydberg interactions on propagating light fields is explored. Dissipative interactions between dark-state polaritons give rise to a strongly nonlinear optical response and sub-Poissonian statistics of polaritons which reflect the emergence of correlations in both the atomic and light fields. Combined, these experiments help elucidate the effects of Rydberg induced correlations on diverse physical systems involving atoms, ions and photons.

This thesis is based on the following manuscripts and publications:

- **Combined ion and optical detection of Rydberg atoms in dense ultracold atomic gases**
  C. S. Hofmann, G. Günter, H. Schempp, N. L. M. Müller, A. Faber, H. Busche, M. Robert-de-Saint-Vincent, S. Whitlock, M. Weidemüller
  in preparation
- **Sub-Poissonian statistics of Rydberg-interacting dark-state polaritons**
  C. S. Hofmann, G. Günter, H. Schempp, M. Robert-de-Saint-Vincent, M. Gärttner, J. Evers, S. Whitlock, M. Weidemüller
  arXiv:1211.7265 (2012), submitted for publication
- **Spontaneous avalanche ionization of a strongly blockaded Rydberg gas**
  M. Robert-de-Saint-Vincent, C. S. Hofmann, H. Schempp, G. Günter, S. Whitlock, M. Weidemüller
  arXiv:1209.4728 (2012), accepted for publication in Physical Review Letters
- **Evidence of Antiblockade in an Ultracold Rydberg Gas**
  T. Amthor, C. Giese, C.S. Hofmann, M. Weidemüller
  Physical Review Letters **104**, 013001 (2010)

The author furthermore contributed to the following publications:

- **Versatile cold atom target apparatus**
  S. Götz, B. Höltkemeier, C. S. Hofmann, D. Litsch, B. D. DePaola, M. Weidemüller
  Review of Scientific Instruments **83**, 073112 (2012)
- **Interaction Enhanced Imaging of Individual Rydberg Atoms in Dense Gases**
  G. Günter, M. Robert-de-Saint-Vincent, H. Schempp, C. S. Hofmann, S. Whitlock, M. Weidemüller
  Physical Review Letters **108**, 013002 (2012)

- **High-precision semiconductor wavelength sensor based on a double-layer photo diode**
  T. Amthor, C. S. Hofmann, J. Knorz, M. Weidemüller
  Review of Scientific Instruments **82**, 093111 (2011)

- **Quantum interference in interacting three-level Rydberg gases: coherent population trapping and electromagnetically induced transparency**
  S. Sevinçli, C. Ates, T. Pohl, H. Schempp, C. S. Hofmann, G. Günter, T. Amthor, M. Weidemüller, J. D. Pritchard, D. Maxwell, A. Gauguet, K. J. Weatherill, M. P. A. Jones, C. S. Adams
  Journal of Physics B **44**, 184018 (2011)

- **Coherent Population Trapping with Controlled Interparticle Interactions**
  H. Schempp, G. Günter, C. S. Hofmann, C. Giese, S. D. Saliba, B. D. DePaola, T. Amthor, M. Weidemüller, S. Sevinçli, T. Pohl
  Physical Review Letters **104**, 173602 (2010)

- **Quantum Coherence in the Rubidium 5S - 5P - 5D Ladder System, Applications in Frequency Conversion, Imaging, and Squeezing**
  R. E. Scholten, S. C. Bell, D. V. Sheludko, J. D. White, L. D. Turner, T. Meijer, B. Smeets, M. Jeppesen, C. S. Hofmann, M. Jasperse
  Book chapter in: New Trends in Quantum Coherence and Nonlinear Optics; Nova Science Publishers Inc. 2009

- **State-selective imaging of cold atoms**
  D. V. Sheludko, S. C. Bell, R. Anderson, C. S. Hofmann, E. J. D. Vredenbregt, R. E. Scholten
  Physical Review A **77**, 033401 (2008)

Contents

List of Figures

Chapter 1

Introduction

Progress — not only in science — is intimately connected with the invention of new techniques and their further development. The advent of laser cooling and trapping [Ashkin, 1978; Raab *et al.*, 1987], rewarded with the Nobel prize in physics 1997 [Chu, 1998; Cohen-Tannoudji, 1998; Phillips, 1998], not only marked the beginning of a new era in atomic, molecular and optical physics but also in quantum physics. The ability to produce and manipulate dilute atomic vapors with temperatures just above the absolute zero point led to seminal discoveries in the past three decades. Ultracold temperatures were necessary to create and explore quantum-degenerate gases — new phases of matter — such as Bose-Einstein condensates [Anderson *et al.*, 1995; Davis *et al.*, 1995; Bradley *et al.*, 1995] and degenerate Fermi gases [DeMarco and Jin, 1999], which are today routinely available in laboratories around the world. The possibility to precisely control and tune interactions in ultracold gases furthermore allowed the preparation and investigation of intriguing many-body systems. Their complexity is characterized by the emergence of spatial and temporal correlations that arise when inter-particle interactions dominate the energy hierarchy [Bloch *et al.*, 2008]. Major examples of such phenomena are the superfluid to Mott-insulator quantum phase transition [Greiner *et al.*, 2002] or the fermionization of bosons in a Tonks-Girardeau gas [Kinoshita *et al.*, 2004; Paredes *et al.*, 2004].

So far the research on ultracold gases primarily focused on short-range interactions, but the extension to long-range interactions recently opened a new chapter in the study of many-body physics. Atoms excited to highly-lying electronic states, called Rydberg atoms, are ideal candidates to put this extension into effect, as they offer long-ranged attractive and repulsive interactions whose strength and character can be vastly tuned as a consequence of their huge polarizabilities. For neutral atoms Rydberg–Rydberg interactions possess the strongest inter-particle interaction, exceeding typical interactions in cold gases by several orders of magnitude. In these systems the laser excitation itself has the potential to create strongly correlated many-body states. The hallmark of many-body Rydberg physics is an excitation blockade, which due to the sizable interaction between Rydberg atoms inhibits the simultaneous laser excitation of multiple atoms within a critical radius, referred to as the blockade radius. The blockade effect and the concomitant exclusion volume crucially determine the excitation dynamics of an ultracold Rydberg gas, since the excitation is coherently shared amongst all atoms inside each blockade sphere, giving rise to collective excitation effects [Dicke, 1954]. These have been observed experimentally [Heidemann *et al.*, 2007; Gaëtan *et al.*, 2009; Urban *et al.*, 2009; Dudin *et al.*, 2012b; Maxwell *et al.*, 2012], paving the way towards quantum computation using ensembles of atoms [Lukin *et al.*, 2001; Saffman *et al.*, 2010]. Bulk properties of Rydberg gases are likewise influenced by the blockade phenomenon as evidenced by a strong suppression of excitation [Tong *et al.*, 2004; Singer *et al.*, 2004; Vogt *et al.*, 2006; Vogt *et al.*, 2007] and sub-Poissonian counting statistics [Reinhard *et al.*, 2008b; Viteau *et al.*, 2012; Hofmann *et al.*, 2012].

The latter is accompanied by the emergence of strong correlations which have received considerable attention in theoretical work [Robicheaux and Hernández, 2005; Stanojevic and Côté, 2010; Wüster *et al.*, 2010; Pohl *et al.*, 2010; Schachenmayer *et al.*, 2010; Ates and Lesanovsky, 2012; Breyel *et al.*, 2012]. Only recently a microscopic analysis of Rydberg interacting gases has become possible, unveiling the strongly correlated many-body states that emerge when atoms are resonantly excited to Rydberg states [Schwarzkopf *et al.*, 2011; Schauß *et al.*, 2012]. Using an all-optical imaging technique Schauß *et al.* could directly access spatial excitation patterns of up to five Rydberg atoms which are observed to arrange in well defined geometries imposed by the blockade radius but in random orientations [Schauß *et al.*, 2012]. A theoretical study recently predicted the dynamical formation of floating Rydberg excitation crystals also for off-resonant laser driving, allowing an adjustment of the lattice constants through the laser detuning [Gärttner *et al.*, 2012].

This is related to the so-called antiblockade phenomenon introduced by Ates *et al.*, who predicted that far-detuned laser excitation can serve as a means to overcome the excitation blockade and that atom pairs can selectively be excited at distances smaller than the blockade radius [Ates *et al.*, 2007a]. The experimental demonstration of the antiblockade is given in the present work and it is shown that by exploiting the blockade and antiblockade in a controlled way, spatial correlations can be imposed on the excited atoms in an otherwise randomly arranged ultracold gas [Amthor *et al.*, 2010]. Specific pair distances can thus be preferred or suppressed, which might be used in experiments requiring large numbers of atom pairs, e.g., as an initialization or detection step in quantum gate experiments.

Despite the achievable control, Rydberg–Rydberg interactions and their associated dynamics can have dramatic consequences on the stability of cold Rydberg gases, since mechanical forces given by the gradient of the interaction potential can lead to collisional ionization. These collisions occur on microsecond timescales [Amthor *et al.*, 2007b], which can cause the spontaneous evolution of a Rydberg gas into an ultracold plasma [Li *et al.*, 2004; Walz-Flannigan *et al.*, 2004; Morrison *et al.*, 2008]. Neutral ultracold plasmas — gases of unbound charged particles — form a research field in their own [Killian, 2007] as they offer an ideal laboratory setting to better understand exotic phases of matter such as dense astrophysical plasmas [Horn, 1991] or laser-induced plasmas [Remington *et al.*, 1999]. Experimental and theoretical progress in their investigation is driven by the potential to reach the so-called strongly coupled regime, in which the Coulomb interaction energy dominates the kinetic energy [Ichimaru, 1982; Killian *et al.*, 2007], giving rise to collective many-body effects [Fletcher *et al.*, 2006; Castro *et al.*, 2010; Twedt and Rolston, 2012] and sizable spatial correlations between particles. Reaching deep into the strongly coupled regime, however, has remained out of reach partially due to so-called disorder-induced heating, in which the Coulomb interaction energy of the initially randomly distributed particles is converted into kinetic energy [Murillo, 2001; Simien *et al.*, 2004; Pohl *et al.*, 2004a; Cummings *et al.*, 2005]. One promising approach to mitigate disorder-induced heating, is to form a plasma from a Rydberg gas, as its constituents can be easily ionized and strong Rydberg–Rydberg interactions naturally result in an initially spatially correlated state [Gericke and Murillo, 2003]. Such experiments were performed in the context of this thesis, in which it was shown for the first time that a strongly blockaded, repulsively interacting Rydberg gas can undergo a spontaneous avalanche ionization [Robert de Saint Vincent *et al.*, 2012]. The obtained results suggest that the initial correlations of the Rydberg ensemble should be imprinted onto the ions and persist through the avalanche, thereby potentially offering a new route to enter strongly coupled plasma regimes.

So far the discussion focused on Rydberg–Rydberg interaction effects on the matter degrees of freedom. In conjunction with these long-ranged interactions is a substantial back-action on the radiation field, which becomes evident when considering a full description of Rydberg atom–light interactions. Electromagnetically induced transparency (EIT) is a paradigm for such atom–light interfaces and is based on a quantum interference effect in which an otherwise absorbing medium is rendered transparent by an optical control field [Fleischhauer *et al.*, 2005]. Occurring in coherently driven three level systems, electromagnetically induced transparency has recently been used in combination with Rydberg states as a novel nondestructive Rydberg probing method [Mohapatra *et al.*, 2007] and as a sensitive electrometry technique [Kübler *et al.*, 2010; Tauschinsky *et al.*, 2010; Hattermann *et al.*, 2012; Sedlacek *et al.*, 2012]. Since the Rydberg state properties are directly mapped onto the light field, Rydberg EIT therefore provides a powerful alternative to field ionization detection. The combination of both techniques is put forward here and gives access to both microscopic and macroscopic properties of the system.

Qualitatively new effects arise when electromagnetically induced transparency is combined with Rydberg interactions, which has recently attracted significant attention in experimental work [Pritchard *et al.*, 2010; Schempp *et al.*, 2010] and theoretical studies [Møller *et al.*, 2008; Ates *et al.*, 2011; Sevinçli *et al.*, 2011a; Petrosyan *et al.*, 2011]. This is motivated by the appearance of a novel cooperative optical nonlinearity which is induced by Rydberg–Rydberg interactions and observed as a back-action on the probe field. The nonlinearity can be understood by the fact that the atoms in each blockade volume are in a coherent superposition in which only one atom can be excited to the Rydberg state and thereby contribute to the transparency, while the remaining atoms act as two-level atoms which couple resonantly to the probe field, leading to a suppression of transmission [Pritchard *et al.*, 2010]. The dynamic range of this optical nonlinearity is studied in the work presented here and it is shown that by increasing the number of atoms inside the blockade volume, the light transmission can be suppressed almost completely up to a regime in which only a few photons can freely propagate through the medium [Hofmann *et al.*, 2012].

In stark contrast to conventional optical materials, the Rydberg interaction-induced optical nonlinearity remains strong at the few-photon level giving rise to peculiar effects: when a light pulse — composed of individual photons — enters a Rydberg EIT medium, photonic excitations are temporarily transferred to Rydberg excitations through the formation of quasi-particles, called dark-state polaritons [Fleischhauer and Lukin, 2000]. These quasi-particles simultaneously possess properties of both photonic and atomic degrees of freedom which can be interchanged in a fully coherent and reversible process, as demonstrated in the present work in which the dynamics of individual dark-state polaritons is studied. This is possible through single-atom sensitive detection of the Rydberg population which gives direct access to the matter part of the polariton wavefunction inside the atomic cloud. In this case long-range interactions between Rydberg atoms give rise to an effective interaction blockade for dark-state polaritons, which is observed as a transition from

Poissonian to sub-Poissonian statistics for the polariton number, indicating the emergence of spatial and temporal correlations between dark-state polaritons [Hofmann *et al.*, 2012]. Amongst other recent results [Dudin and Kuzmich, 2012; Peyronel *et al.*, 2012; Maxwell *et al.*, 2012], these measurements mark first steps towards a promising and new research area of nonlinear Rydberg quantum optics, since the aforementioned quantum nonlinearity can also be viewed as photon blockade mechanism [Pritchard *et al.*, 2012]. This might open a promising avenue for realizing many-body phenomena with strongly interacting photons [Chang *et al.*, 2008; Sevinçli *et al.*, 2011b; Nikoghosyan *et al.*, 2012]. Other applications could go towards photonic quantum information processing [Lukin *et al.*, 2001; Friedler *et al.*, 2005; Gorshkov *et al.*, 2011; Shahmoon *et al.*, 2011].

Even though the wide range of phenomena connected with ultracold Rydberg atoms detailed above is not complete, it nonetheless highlights the richness of these systems. This thesis studies the application of strongly interacting states of Rydberg atoms as a means to introduce and control correlations in diverse systems including atoms, ions and photons.

The second chapter of this work gives a brief introduction to ultracold Rydberg gases and forms its basis connecting the most important properties and their consequences to the performed research. Chapter 3 describes a new experimental setup for the investigation of dense ultracold Rydberg gases which was designed and built within the framework of this thesis. It combines high atomic and optical densities with excellent control over electric fields as well as precise Rydberg atom detection. The fourth chapter discusses the experimental evidence of antiblockade in a dilute Rydberg gas and primarily focuses on two-body interaction effects that are used to directly manipulate the Rydberg pair distribution through the excitation of close neighboring pairs. When preforming experiments in dense atomic gases, the spontaneous avalanche ionization of a strongly blockaded Rydberg gas was discovered and physical processes that have relevance for the close-by research field of ultracold plasmas were investigated, which are described in Ch. 5. A very recent research topic is tackled in Ch. 6 in which both light and matter aspects of strongly interacting Rydberg dark-state polaritons in dense atomic gases are analyzed and compared to a state-of-the-art theoretical approach for the coupled atom–light system. The findings reveal that a rigorous many-body treatment of this problem, including the effects of the quantized electromagnetic field is still lacking. Finally, the last chapter summarizes the important results of this work and gives an outlook on future directions for this research, such as the direct observation of quantum correlations and the realization of new forms of quantum matter.

Chapter 2

Strongly interacting ultracold Rydberg gases

The exploration of Rydberg atoms is a self-contained research field of atomic physics which has been pursued for more than a century (for reviews see [Gallagher, 2008; Stebbings and Dunning, 2011]). The advent of laser-cooling has revived the interest in Rydberg atoms and has dramatically extended their context of investigation, leading to new developments which are summarized in recent monographs [Choi *et al.*, 2006; Gallagher and Pillet, 2008; Saffman *et al.*, 2010; Comparat and Pillet, 2010]. For this reason, only a brief overview of ultracold Rydberg gases is given here, which highlights the properties most relevant for this thesis. This introductory chapter starts with the basic properties of Rydberg atoms that can be explained with simple scaling laws. Sec. 2.2 discusses Rydberg–Rydberg atom interactions which due to their strong and long-range character lead to a diversity of intriguing many-body phenomena, which is studied in this thesis. Afterwards Rydberg atom–light interactions are detailed in Sec. 2.3, revealing that these interactions can cause a significant back-action onto the driving laser fields, which broadens the range of applications of Rydberg atoms to new areas such as nonlinear and quantum optics.

2.1 Alkali Rydberg atoms

Highly excited atoms have been studied since the 19th century. In 1885 Johann J. Balmer discovered converging line series in an atomic hydrogen spectrum which are now known as Balmer Series [Balmer, 1885]. Later Johannes Rydberg, generalized Balmer's discovery to many other chemical elements by giving the following formula for the wavenumbers of the observed series [Rydberg, 1890]

$$\Delta\nu = Ry\left(\frac{1}{m^2} - \frac{1}{n^2}\right) . \tag{2.1}$$

where m and n are integer numbers and Ry is today known as the Rydberg constant. Niels Bohr identified theses integer numbers as principal quantum numbers n [Bohr, 1913] and linked the Rydberg constant to fundamental constants as

$$Ry = \frac{Z^2 e^4 m_e}{2(4\pi\epsilon_0\hbar)^2} , \tag{2.2}$$

with Z the proton number, e the electron charge, m_e the electron mass, ϵ_0 the vacuum permittivity, and $\hbar$ the Planck constant.

Electronically excited alkali atoms have much in common with the simple hydrogen atom. Their single valence electron can be excited to a high-lying state — called Rydberg state — while the closed electron shells shield the core charge, giving rise to a net core charge of $Z = 1$. However for low orbital angular momentum states $\ell \leq 3$, the electrons can penetrate the finite size core and are thus exposed to core charges of $Z > 1$. This gives rise to a deviation of the core potential from a pure Coulombic potential at short range and lifts the ℓ-degeneracy known from the Hydrogen atom. The resulting increased binding energy W is

$$W = -\frac{Ry}{\mathsf{n}^{\star 2}} = -\frac{Ry}{(\mathsf{n} - \delta_\ell)^2} , \tag{2.3}$$

which is parametrized by the effective quantum number $\mathsf{n}^\star$, that is henceforth used throughout this thesis. Ry is the Rydberg constant which for Rubidium $Ry^{Rb} = 109736.605\,\mathrm{cm}^{-1}$ [Gallagher, 2008]. The quantum defect δ_ℓ — described by the empirical Rydberg-Ritz formula [Jastrow, 1948] — gives rise to a rich internal structure of alkali Rydberg atoms. $|S\rangle$ states have for instance the largest quantum defects ($\delta \approx 3$ for Rb[i]) since they have the strongest core penetration. The quantum defect decreases for larger angular momentum states and results in energetically isolates $|S\rangle$, $|P\rangle$ and $|D\rangle$ states, which are easily accessible in laser excitation. For $\ell > 3$ the quantum defect becomes negligible such that the core potential appears purely Coulombic giving rise to 'hydrogen-like' states, *i.e.* angular momentum states that are degenerate in the principal quantum number.

Although replaced by modern quantum mechanics, the Bohr model still gives quick access to the scalings of many characteristic properties of Rydberg atoms that

---

[i] The corresponding values for Rubidium have lately been determined accurately by [Li *et al.*, 2003; Han *et al.*, 2006].

Table 2.1: Some properties of Rydberg atoms and scalings with the effective principal quantum number $\mathsf{n}^\star = \mathsf{n} - \delta_\ell$. Adapted from [Gallagher, 2008].

Quantity	$\mathsf{n}^\star$ dependence
Electron binding energy W	${\mathsf{n}^\star}^{-2}$
Energy difference Δ between adjacent n-states	${\mathsf{n}^\star}^{-3}$
Ionizing field $\mathcal{E}^{(\infty)}$	${\mathsf{n}^\star}^{-4}$
Orbital radius r	${\mathsf{n}^\star}^{2}$
Geometrical cross-section σ_{geo}	${\mathsf{n}^\star}^{4}$
Dipole moment $\mu = \langle \mathsf{n}S \vert e\mathsf{r} \vert \mathsf{n}P \rangle$	${\mathsf{n}^\star}^{2}$
Radiative lifetime τ	${\mathsf{n}^\star}^{3}$
Polarizability α	${\mathsf{n}^\star}^{7}$

depend upon the effective principal quantum number $\mathsf{n}^\star = \mathsf{n} - \delta_\ell$ (see Table 2.1). The fact that most properties scale with high powers of $\mathsf{n}^\star$ explains the exaggerated features of Rydberg atoms which gives rise to interesting experimental consequences, which are discussed in this chapter.

Examples of simple scaling laws include the electron binding energy W which is proportional to ${\mathsf{n}^\star}^{-2}$ (see (2.1)) and the (classical) electric ionization field $\mathcal{E}^{(\infty)}$ which scales with ${\mathsf{n}^\star}^{-4}$. The quadratic $\mathsf{n}^\star$-scaling of the orbital radius r gives rise to large geometrical cross-sections $\sigma_{\text{geo}} \propto {\mathsf{n}^\star}^{4}$. Combined with the weak binding energies, this turns Rydberg atoms into very fragile objects that easily undergo collisional ionization [Percival and Richards, 1975; Olson, 1979; Barbier and Cheret, 1987], as will be discussed later.

The scaling laws also find their application in the prediction of dipole transitions strengths between atomic states. They occur due to coupling with the electric dipole moment $\mu = e\mathsf{r}$ of the valence electron. The according coupling strength between states $\vert \mathsf{n}\ell m_\ell \rangle$ and $\vert \mathsf{n}'\ell' m'_\ell \rangle$ is given by the dipole matrix element $\langle \mathsf{n}\ell m_\ell \vert \mu \vert \mathsf{n}'\ell' m'_\ell \rangle$ which is the overlap integral between the Rydberg state wavefunctions and the electric dipole moment. One can show that the scaling of the $\vert \mathsf{n}\mathrm{S} \rangle \leftrightarrow \vert \mathsf{n}\mathrm{P} \rangle$ transition matrix elements can be approximated by ${\mathsf{n}^\star}^{2}$ [Amthor, 2008]. As we will see in Sec. 2.2 this leads to very pronounced Rydberg–Rydberg interactions which give rise to a multitude of intriguing phenomena in Rydberg gases. Note that the matrix elements between neighboring Rydberg states are many orders of magnitude larger than the matrix elements to low-lying states. Their values scale as $C_\ell \, {\mathsf{n}^\star}^{-3/2}$ with ℓ-dependent transition strengths. For Rubidium $C_S = \sqrt{1/3} \cdot 4.508 \, ea_0$ and $C_D =$

$\sqrt{2/5} \cdot 8.475\, ea_0$, where a_0 is the Bohr radius [Deiglmayr *et al.*, 2006].

From the knowledge of the dipole matrix elements, it is possible to deduce the radiative lifetimes τ of the Rydberg states which in first order scale as $\mathsf{n}^{\star\,-3}$ [Gounand, 1979] and therefore range from several μs even up to ms, allowing comparatively long observation as well as interrogation times for experiments with Rydberg atoms. More involved, state dependent calculations of the effective lifetimes of different alkali atoms — accounting for blackbody radiation — can be found in [Beterov *et al.*, 2007; Beterov *et al.*, 2009a].

Finally the scaling law of the polarizability α can easily be derived since α is the sum of squares of the dipole matrix elements to neighboring states, divided by the energy difference of these states. The dipole matrix elements of neighboring levels scale like the orbital radius as $\mathsf{n}^{\star\,2}$. From (2.1) it follows, that the binding energy scales as $\mathsf{n}^{\star\,-2}$ resulting in a $\mathsf{n}^{\star\,-3}$ scaling of the energy difference Δ between adjacent n. The total scaling law for the polarizability is thus: $\alpha \propto (\mathsf{n}^{\star\,2})^2/\mathsf{n}^{\star\,-3} = \mathsf{n}^{\star\,7}$, which is in good agreement with an empirical scaling fitted to experimental data in [O'Sullivan and Stoicheff, 1985; O'Sullivan and Stoicheff, 1986].

One remarkable consequence of this scaling is the large susceptibility of Rydberg atoms to external electric fields $\mathcal{E}$, as for angular momentum states with $\ell \leq 3$ the Stark effect scales with $\Delta U = 1/2\, \alpha \mathcal{E}^2$. This turns Rydberg atoms into sensitive probes for electrometry applications [Osterwalder and Merkt, 1999; Tauschinsky *et al.*, 2010; Hattermann *et al.*, 2012]. The pronounced electric field sensitivity is not only a feature, but also implies experimental challenges making excellent electric field control a prime requirement for experiments with ultracold Rydberg atoms. For this reason a special electrode structure was designed within the framework of this thesis (see Sec. 3.6).

2.2 Rydberg–Rydberg atom interactions

An important theme in this thesis is the effect of strong Rydberg–Rydberg interactions on many-body system. Section 2.2.1 reveals that Rydberg interactions can be controlled in strength, sign and spatial dependence through the choice of state. On the one hand, for attractive interactions, this leads to ionizing collisions which are detailed in Sec. 2.2.2. On the other hand, given repulsive interactions, this results in an excitation blockade, which is the hallmark of strong Rydberg–Rydberg interactions and gives rise to a multiplicity of many-body effects. The blockade inhibits the simultaneous laser excitation of two atoms within a given distance due to the strong interaction between Rydberg atoms (Sec. 2.2.3). Associated with this is an exclusion volume (the blockade sphere) which critically determines the excitation dynamics of an ultracold Rydberg gas, giving rise to two phenomena which are central in this thesis: The considerable suppression of excitation discussed in Sec. 2.2.4 and the appearance of sub-Poissonian counting statistics detailed in Sec. 2.2.5.

2.2.1 Long-range interactions

Due to their large polarizability, Rydberg atoms exhibit strong dipole–dipole and van der Waals interactions over large distances. These interactions can be understood intuitively by considering two (classical) dipoles with dipole moments $\boldsymbol{\mu}_1$ and $\boldsymbol{\mu}_2$. Their interaction energy in atomic units is given by

$$U_{\mathrm{dd}}(R) = \frac{\boldsymbol{\mu}_1 \cdot \boldsymbol{\mu}_2}{|\mathbf{R}|^3} - 3\,\frac{(\boldsymbol{\mu}_1 \cdot \mathbf{R})\,(\boldsymbol{\mu}_2 \cdot \mathbf{R})}{|\mathbf{R}|^5}\,, \tag{2.4}$$

where $\mathbf{R}$ is the distance vector that connects the two dipoles. The second term on the right hand side in (2.4) accounts for the angular dependence of the interaction energy and is dropped for the following discussion[ii]. In the quantum mechanical description the dipoles are represented by dipole operators with matrix elements $\mu = \langle\varphi|\, e\mathsf{r}\, |\varphi'\rangle$ as discussed previously. For two atoms in the internal states $|\varphi_1\rangle$ and $|\varphi_2\rangle$ the Dipole interaction U_{dd} is then expressed as

$$U_{\mathrm{dd}}(R) \propto \frac{1}{R^3} \sum_{|\varphi_1\rangle,|\varphi_2\rangle} \langle\varphi_1|\, \mu_1\, |\varphi_1'\rangle\, \langle\varphi_2|\, \mu_2\, |\varphi_2'\rangle = \sum_{|\varphi_1,\varphi_2\rangle} \left\langle \varphi_1, \varphi_2 \right| \frac{\mu_1\,\mu_2}{R^3} \left| \varphi_1', \varphi_2' \right\rangle\,, \tag{2.5}$$

where — in principle — one has to sum over all internal states of the atoms. For simplicity, we restrict the discussion only to adjacent angular momentum states *e.g.* $|P\rangle$, $|S\rangle$, and $|P'\rangle$ as the dipole matrix elements between these states are the largest.

In the last step of (2.5), we changed from the atomic basis to the pair state basis in order to deduce the dipole–dipole-induced energy shift. The initial pair state $|SS\rangle$ is coupled by $U_{\mathrm{dd}}(R) = (\mu_1\,\mu_2)/R^3$ to the state $|PP'\rangle$, which is offset by the Förster defect $\Delta = U_{|P\rangle} + U_{|P'\rangle} - 2U_{|S\rangle}$ (see Fig. 2.1). In the pair basis $\{|SS\rangle\,, |PP'\rangle\}$, the complete Hamiltonian $\mathcal{H} = \mathcal{H}_{\mathrm{a}} + \mathcal{H}_{\mathrm{int}}$ describing the atomic system $\mathcal{H}_{\mathrm{a}}$ and the off-diagonal interaction part $\mathcal{H}_{\mathrm{int}}$ can then be written as:

$$\mathcal{H} = \begin{pmatrix} 0 & U_{\mathrm{dd}}(R) \\ U_{\mathrm{dd}}(R) & \Delta \end{pmatrix}\,. \tag{2.6}$$

[ii] This approximation is valid for S-states since they interact isotropically [Walker and Saffman, 2008].

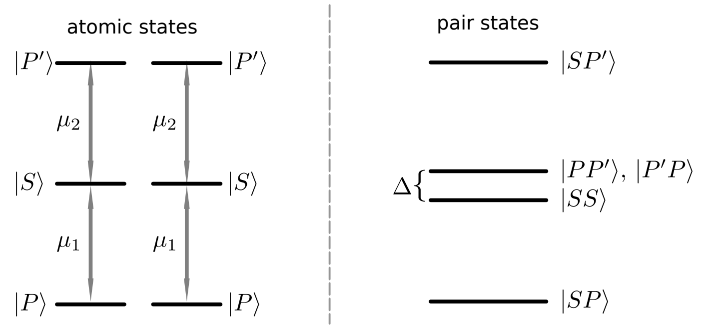

Figure 2.1: Origin of strong Rydberg–Rydberg interactions. The dipole matrix elements μ_1 and μ_2 couple between the Rydberg states $|S\rangle \leftrightarrow |P\rangle$ and $|S\rangle \leftrightarrow |P'\rangle$, respectively. In the pair state basis, the states $|SS\rangle$ and $|PP'\rangle$ only reveal a small energy defect Δ and are thus almost degenerate. The small Δ is responsible for the strong and long-range Rydberg–Rydberg interactions.

The according eigenenergies of the system are derived to be

$$U_\pm = \frac{\Delta}{2} \pm \sqrt{\left(\frac{\Delta}{2}\right)^2 + U_{\mathrm{dd}}^2(R)}\,. \tag{2.7}$$

We notice that the pair energy is dependent on the inter-atomic separation R, which gives rise to two regimes: At large inter-atomic separations the interaction is negligible ($U_{\mathrm{dd}}(R) \ll \Delta$) whereas it is dominating at short distance ($U_{\mathrm{dd}}(R) \gg \Delta$), resulting in interesting consequences on the interaction characteristics [Amthor *et al.*, 2009]:

(i) **van der Waals interactions** — At long range ($U_{\mathrm{dd}}(R) \ll \Delta$) a Taylor expansion of (2.7) gives

$$U_\pm = -\frac{\Delta}{2} \pm \left(\frac{\Delta}{2} + \frac{U_{\mathrm{dd}}^2(R)}{\Delta} + \cdots\right) , \tag{2.8}$$

such that the energy shift of the $|SS\rangle$ state is given by a second order effect in perturbation theory

$$\Delta U = -\frac{U_{\mathrm{dd}}^2(R)}{\Delta} = -\frac{(\mu_1\,\mu_2)^2\,/\,\Delta}{R^6} := \frac{-C_6}{R^6}\,. \tag{2.9}$$

This is the well-known van der Waals interaction energy, which has a very sensitive dependence upon the principal quantum number, because $\mu \propto \mathsf{n}^{\star 2}$ and $\Delta \propto \mathsf{n}^{\star -3}$ such that one arrives at a scaling of the interaction coefficient of $C_6 \propto \mathsf{n}^{\star 11}$. Simply doubling $\mathsf{n}^\star$ will thus increase the interaction strength by more than three orders of magnitude! Furthermore one can show that many-body interactions in the van der Waals regime are dominated by nearest neighbor interactions, which allows a two-body treatment of the many-body system [Amthor, 2008].

(*ii*) **Resonant dipole–dipole interactions** — When the energy difference Δ becomes negligible ($\Delta \to 0$), the system exhibits a pair state resonance, and (2.7) reduces to

$$U_{\pm} = \pm \frac{\mu_1 \, \mu_2}{R^3} := \pm \frac{C_3}{R^3} \, . \tag{2.10}$$

The interaction energy now depends on the distance as $1/R^{-3}$ and the associated dipole coefficient scales as $C_3 \propto \mathsf{n}^{\star 4}$, leading to the strongest possible interaction energies between two non-overlapping Rydberg atoms[iii]. Due to the R^{-3} scaling it is necessary to consider the complete many-body system. An in-depth discussion of the relative interaction contribution of surrounding atoms in the dipolar and van deer Waals regime is given in [Amthor, 2008].

The crossover between the van der Waals and the dipole interaction regime takes place when $U_{\mathrm{dd}}(\tilde{R}) \approx \Delta$, which is equivalent to the crossover radius $\tilde{R} = \sqrt[6]{|C_6|/\Delta} \propto \mathsf{n}^{\star 7/3}$ [Walker and Saffman, 2008].

Note that in most atomic systems one has only little influence on the pair state detuning Δ. However as a consequence of the anomalously large polarizabilities of Rydberg atoms, the Stark effect offers a simple means to tune sign and magnitude of the energy defect by applying only moderate electric fields. For some combinations of Rydberg states, even the case $\Delta = 0$ — a so-called Förster resonance — can be realized, leading to resonant dipole–dipole interactions for all R [Gallagher *et al.*, 1982; Vogt *et al.*, 2006; Ryabtsev *et al.*, 2007].

The sign and strength of the interactions are dominated by the pair states with the smallest energy defect Δ. For the $\left|\mathsf{n}S_{1/2}\right\rangle$ states of alkali atoms these are the $\left|\mathsf{n}P_{3/2}\right\rangle$ and $\left|(\mathsf{n}-1)P_{3/2}\right\rangle$ states and it turns out that the according C_6 coefficients are negative for all n, leading to repulsive interactions. $\left|\mathsf{n}D_{5/2}\right\rangle$ states have smaller energy defects and hence exhibit stronger interactions than $|S\rangle$ states with the same n. For $\left|D_{5/2}\right\rangle$ states of Rubidium there is a sign change of the C_6 coefficient from negative to positive, such that interactions for $\mathsf{n} \geq 43$ are predominantly attractive [Reinhard *et al.*, 2007]. $\left|\mathsf{n}D_{3/2}\right\rangle$ states of Rb show purely attractive interactions

---

[iii] This approximation is only valid down to the LeRoy-radius below which the exchange interaction of the electrons cannot be neglected anymore [Boisseau *et al.*, 2002].

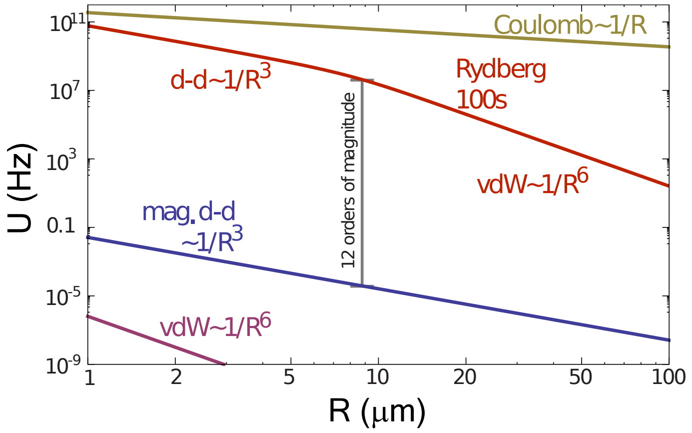

Figure 2.2: Comparison between different types of two-body interactions. The weakest interactions are experienced between ground state atoms and are of van der Waals (vdW) character (purple line). Atoms with magnetic dipole moments have considerable interactions and interact via dipole–dipole (d–d) interactions (blue line), which are orders of magnitude weaker than Rydberg–Rydberg interactions (here in state $|100\,S\rangle$,red line). At short range they are of d–d character and at long distances of vdW character. Only the Coulomb interaction between ions is stronger and of longer range (brown line). This figure is taken from [Saffman *et al.*, 2010] and replotted with permission of M. Saffman.

for $\mathsf{n} \geq 59$ [Maucher *et al.*, 2011]. A good overview of calculated dispersion C coefficients of alkali atoms can be found in [Singer *et al.*, 2005; Reinhard *et al.*, 2007; Walker and Saffman, 2008].

Figure 2.2 illustrates the magnitude of Rydberg–Rydberg interactions by comparing their distance dependent two-particle interaction strengths to various other interaction types. On the envisaged energy scale ground state atoms exhibit comparatively weak van der Waals interactions (R^{-6}). The range and strength of interacting ground state atoms could recently be extended by trapping species with dominating magnetic dipolar interactions (R^{-3}). This is realized with species like Chromium ($6\,\mu_B$, [Griesmaier *et al.*, 2005]) or lanthanides such as Erbium ($7\,\mu_B$, [Aikawa *et al.*, 2012]) and Dysprosium ($10\,\mu_B$, [Lu *et al.*, 2011]), that offer some of the largest magnetic dipole moments. These interactions are however still small as compared to Rydberg atom interactions shown in Fig. 2.2 for $|100\,\mathrm{S}\rangle$ Rydberg states. At short distances they are of very strong resonant dipole–dipole character (R^{-3}) and of van der Waals character (R^{-6}) at long range. The mentioned crossover length is in this case close to $\tilde{R} = 9.5\mu m$, and at this length scale the ratio of the Rydberg interaction to the ground state interaction is approximately 10^{12} [Saffman *et al.*, 2010]! Under certain conditions, as detailed in Ch. 5, Rydberg atoms will undergo a transition to ionic gases, featuring the strongest possible inter-particle interactions scaling with R^{-1}. Figure 2.2 moreover reveals two important consequences for the physics of Rydberg gases:

(i) **Interaction tuning by changing the atomic density** — So far we only considered the principal quantum number n as means to change the interaction energy between Rydberg atoms. However since the inter-atomic separation R scales with the atomic density as $n^{-1/3}$, we identify the density as another key parameter to tune Rydberg–Rydberg interactions. For van der Waals interactions we find the interaction energy to scale as n^2. It is in fact much easier to change the atomic density within subsequent experimental runs than the principal quantum number and Sec. 3.5.3 explains how we are able to vary the atomic density by *almost four orders of magnitude* with our experimental apparatus.

(ii) **Ultracold Rydberg gases are interaction dominated gases** — In a gas with atomic density n the van der Waals interaction per particle is given by $C_6 n^2$. For a typical density of $n = 10^{12}\,\mathrm{cm}^{-3}$ (mean distance $\approx n^{-1/3} = 1\,\mu\mathrm{m}$) and $C_6 \approx -\hbar \times 50\,\mathrm{GHz}\,\mu\mathrm{m}^6$ (for Rubidium atoms in the $|55\,S\rangle$ state), the pairwise interaction energy reaches $U \approx \hbar \times 50\,\mathrm{GHz}$. This has to be compared with the kinetic energy E_{kin} of the particles which is of the order of a few tens of kHz in an ultracold gas at μK temperatures. We thus find that ultracold Rydberg gases are entirely dominated by the Rydberg–Rydberg interactions ($U/E_{kin} \gg 1$), which in turn give rise to many-body effects.

2.2.2 Collisional ionization

Considerable mechanical forces given by the gradient of the interaction potentials are a direct consequence of long-range Rydberg–Rydberg interactions. Knuffman *et al.* showed that these forces lead to an acceleration of Rydberg atoms within a cold atomic gas [Knuffman and Raithel, 2006]. The attractive van der Waals interaction accelerates two nearest neighbor atoms towards each other, leading to collisions on microsecond time scales [Amthor *et al.*, 2007b]. Due to their considerable collisional cross-sections which are proportional to the geometrical cross-section $\sigma_{\mathrm{geo}} \propto \mathsf{n}^{\star 4}$ this immediately leads to rapid ionizing collisions [Olson, 1979; Vitrant *et al.*, 1982]. The associated mechanism is called Penning ionization and characterized by the binary process:

$$\mathrm{Ryd}(\mathsf{n}) + \mathrm{Ryd}(\mathsf{n}) \quad \longrightarrow \quad \mathrm{Ryd}(\mathsf{n}') + \mathrm{ion} + \mathrm{e}^- , \tag{2.11}$$

where n and n' label the initial and final principal quantum number, respectively. The $\mathsf{n}' < \mathsf{n}$ are distributed over a range of principal quantum numbers with a maximum at $\mathsf{n}'_{\mathrm{max}} = \mathsf{n}/\sqrt{2}$ being imposed by energy conservation [Robicheaux, 2005]. Relying on binary collisions between attractively interacting Rydberg atoms, Penning ionization provides an ideal means to map out Rydberg pair distributions since the nearest neighbor distance is unambiguously encoded in the collision time. We will use this sensitive technique in Ch. 4 in order to gain spatial information circumventing the need for a spatially resolved measurement.

In a sufficiently dense many-body system Penning ionization can even trigger an ionization avalanche as electrons get trapped by the attractive potential of the inertial ions [Robinson *et al.*, 2000; Walz-Flannigan *et al.*, 2004; Li *et al.*, 2004; Li *et al.*, 2005]. This ultimately leads to an intriguing phenomenon, the formation of an ultracold plasma [Killian, 2007]. Interestingly, we found that under certain conditions also *repulsively* interacting Rydberg atoms can undergo this plasma transition as will be shown in Ch. 5. The seed ionization process is in this case partly attributed to ionizing collisions with atoms in the ground and intermediate states [Barbier and Cheret, 1987; Kumar *et al.*, 1999], which lead to a gradual increase in the number of charged particles in the system and to a density dependent ionization onset time.

2.2.3 Excitation blockade

Probably the most prominent consequence of the pronounced Rydberg–Rydberg interaction is an excitation blockade, which is the inhibition of multiple Rydberg excitations within a mesoscopic ensemble of atoms. In a seminal proposal Lukin *et al.*, suggested to use this effect for quantum information processing in mesoscopic atomic ensembles [Lukin *et al.*, 2001]. Fueled by the first experimental evidence of the excitation blockade [Singer *et al.*, 2004; Tong *et al.*, 2004] many experimental and theoretical studies of this effect have been put forward which are reviewed in [Comparat and Pillet, 2010].

The basic idea of the excitation blockade mechanism is illustrated in Fig. 2.3 (a) and can be understood in a pair picture, in which each Rydberg atom is considered as a two level atom with ground state $|g\rangle$ and Rydberg state $|r\rangle$. A laser with coupling strength Ω drives the transition $|g\rangle \rightarrow |r\rangle$. The energies of the pair states $|gg\rangle$ and $|gr\rangle$ remain almost unshifted because of the small polarizability of the ground state atom (compare Fig. 2.2). However, due to the strong Rydberg–Rydberg interaction, the transition $|gr\rangle \rightarrow |rr\rangle$ depends sensitively on the inter-particle distance R. The radius R_{bl} below which the doubly excited state is suppressed is called blockade radius and introduces a natural length scale to the system. It is defined as the distance between two atoms at which the Rydberg interaction energy equals the excitation bandwidth Ω:

$$C_6 n^2 = \frac{C_6}{R^6} = \hbar\Omega \tag{2.12a}$$

$$\Leftrightarrow \quad R_{\mathrm{bl}} = \sqrt[6]{\frac{|C_6|}{\hbar\Omega}} \propto \mathsf{n}^{\star\,11/6}\,. \tag{2.12b}$$

The fact that the Rydberg–Rydberg interaction is orders of magnitude stronger than the Rabi coupling of the Rydberg atoms typically results in μm-sized blockade radii. For instance the $\left|55\,S_{1/2}\right\rangle$ state interaction with a $C_6 = -\hbar \times 50\,\mathrm{GHz}\,\mu\mathrm{m}^6$ and $\Omega = 1\,\mathrm{MHz}$ would yield a blockade radius of $R_{\mathrm{bl}} \approx 6\,\mu\mathrm{m}$. This would correspond to a critical Rydberg density $n_r \propto R_{\mathrm{bl}}^{-3} \approx 4.5 \times 10^9\,\mathrm{cm}^{-3}$, which has to be compared to typical ground state densities n in ultracold gases, which can be tuned from 10^9 to $10^{14}\,\mathrm{cm}^{-3}$ (see Sec. 3.5). Dependent on the ground state density the Rydberg excitation can be strongly blockaded and only one atom out of approximately n/n_r atoms is excited to a Rydberg state as illustrated in Fig. 2.3 (b).

The excitation blockade is also reflected in the Rydberg pair correlation function $g^{(2)}(R)$ as shown in a simplified picture in Fig. 2.3 (c). The Rydberg pair correlation function is defined as the probability that two atoms separated by a distance R are both excited to Rydberg states, divided by the square of the probability that an individual atom is excited [Bellac *et al.*, 2004]. The blockade effect imposes a characteristic correlation length scale given by the blockade radius, such that $g^{(2)}(R)$ is essentially zero for small separations $< R_{\mathrm{bl}}$ and is approaching one at long range, (where the atoms are uncorrelated,) resembling a gas of hard sphere particles. Note, that only a very simplified picture of these correlations was given here. More sophisticated theoretical treatments obtain qualitatively similar correlation functions, suggesting indeed that a gas composed of Rydberg atoms can in first approximation be treated as a gas of hard spheres (see next section), whose mutual exclusion impose strong correlations on the gas [Robicheaux and Hernández, 2005; Stanojevic and Côté, 2010; Ates and Lesanovsky, 2012]. Very recently $g^{(2)}(R)$ could be mapped out experimentally using an all-optical detection technique [Schauß *et al.*, 2012].

2.2.4 A classical hard sphere model

For macroscopic samples subjected to strong local Rydberg interactions, it is often instructive to use the concept of a ‘blockade sphere’ defining an exclusion volume

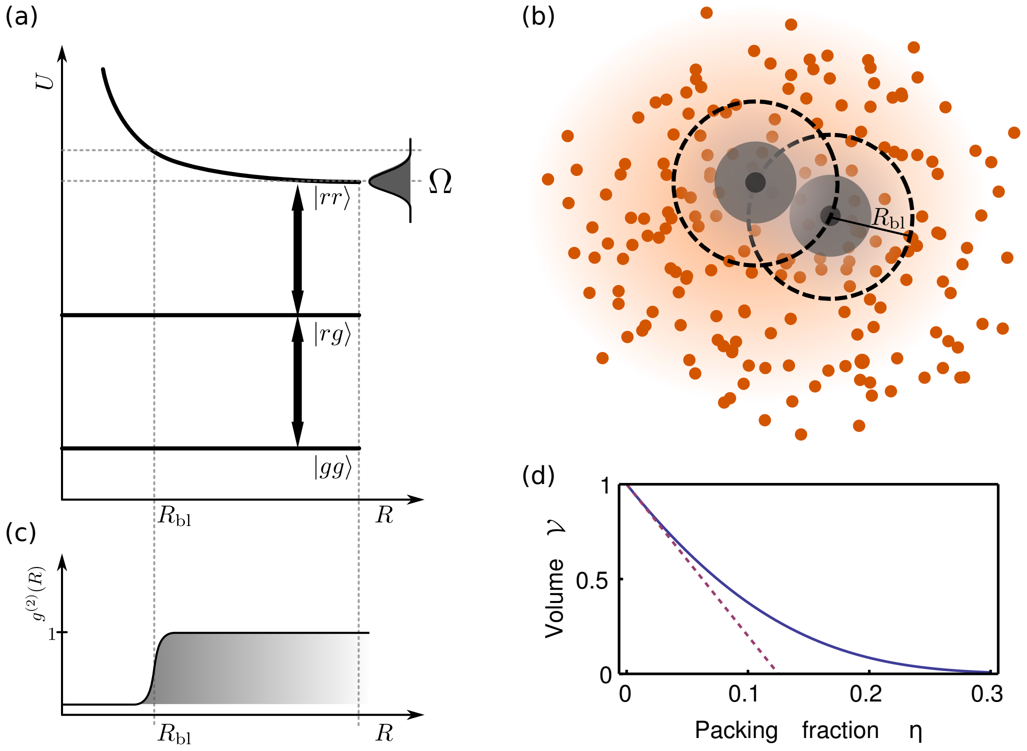

Figure 2.3: Illustration of the excitation blockade mechanism. (a) Pair state energies as a function of inter-atomic separation R. The pair state $|rr\rangle$ is subjected to strong Rydberg–Rydberg interactions and is thus only resonant with the excitation bandwidth Ω within a window of inter-atomic separations. (b) For resonant excitation the blockade radius R_{bl} defines a 'blockade sphere' (dashed circle) in which the excitation blockade only allows for one Rydberg excitation. The associated excitation suppression can be described by packing of hard spheres of radius $R_{\mathrm{bl}}/2$ (solid circles). (c) The pair correlation function $g^{(2)}(R)$ is another representation of the excitation blockade. (d) Fractional available volume $\mathcal{V}$ as a function of the packing fraction η. The solid line shows $\mathcal{V}$ for the random sequential addition of hard spheres which is used to describe the Rydberg excitation suppression in Sec. 2.2.4.

around each excited atom, as illustrated in Fig. 2.3 (b). Using classical hard-objects models and thereby considering the excitation volume as an arrangement of densely packed hard spheres quickly yields a qualitative understanding of a number of phenomena observed in dense Rydberg gases. Assuming the Rydberg density n_r and the ground state n_g, the classical Rydberg excitation dynamics can for instance be described by a simple rate equation

$$\dot{n_r} = A\mathcal{V}\, n_{\mathrm{g}} - B\, n_r\,, \tag{2.13}$$

where A and B are the excitation and de-excitation rate, respectively. For a two level system with negligible loss $A = B$. To account for the excitation blockade, A is multiplied by the fractional available volume $\mathcal{V}$, which is accessible to the center of a subsequently placed blockade sphere with volume $V_{\mathrm{bl}} = 4/3\,\pi R_{\mathrm{bl}}^3$. For an empty excitation volume $\mathcal{V} = 1$, whereas $\mathcal{V} \to 0$ for a densely packed arrangement of hard spheres. A first simple approximation, is given by assuming that each Rydberg atom excludes a volume V_{bl} such that $\mathcal{V} = (1 - n_r\, V_{\mathrm{bl}})$. Furthermore $n_{\mathrm{g}} = n - n_r$, with the total density n. Solving for the steady state of (2.13) one obtains

$$n_r\, V_{\mathrm{bl}} = 1 + \frac{n\, V_{\mathrm{bl}}}{2} - \sqrt{1 + \left(\frac{n\, V_{\mathrm{bl}}}{2}\right)}\,, \tag{2.14}$$

which has two interesting limiting cases:

(*i*) At low densities $n \to 0$, we find $n_r = n/2$, such that the Rydberg atom number increases linearly with the atomic density.

(*ii*) Taylor expanding (2.14) for the high density limit ($n \gg n_r$), leads to $n_r\, V_{\mathrm{bl}} = 1 - 1/(n\, V_{\mathrm{bl}})$, revealing a 'saturation' Rydberg density $n_{\mathrm{r,crit}} = V_{\mathrm{bl}}^{-1}$. As demonstrated shortly this gives rise to a dramatic suppression of excitation, which is a distinguishing manifestation of the excitation blockade and leads to low Rydberg densities.

In Fig. 2.3 (b) we see that each blockade sphere is associated with an exclusion sphere of radius R_{bl} (depicted by the dashed circle), which cannot be occupied by the center of another sphere. Equivalently the configuration can be described by hard spheres with radius $R_{\mathrm{bl}}/2$ (drawn as filled circle). We use the dimensionless packing fraction η — the volume fraction that is occupied by spheres — to quantify the packing. For the case described above $\eta = n_r V_{\mathrm{HS}} = 1/8\, n_r V_{\mathrm{bl}}$ which approaches 1/8 for $n_r \to n_{\mathrm{r,crit}}$ as indicated by the dashed line in Fig. 2.3 (d).

A better description of a gas of hard spheres can be obtained by considering the random sequential addition of hard spheres, which is a fundamental model for the irreversible filling of a volume with impenetrable particles [Talbot *et al.*, 1991]. This concept has for instance been used to model ion implantation in semiconductors [Roman and Majlis, 1983] or to describe liquids, granular materials, powders or colloid systems [Parisi and Zamponi, 2010]. The random sequential addition process is described by an 'inclusion–exclusion' relation of the fractional available volume

$$\mathcal{V} = 1 - \mathcal{V}_1 + \mathcal{V}_2 - \mathcal{V}_3 + \cdots , \tag{2.15}$$

whereof $\mathcal{V} \approx 1 - \mathcal{V}_1 = (1 - n_r\, V_{\text{bl}})$ was previously treated as simplest approximation for the excitation dynamics of a Rydberg gas. Using a virial-like expansion for the fractional available volume for the random sequential addition of hard spheres, Talbot *et al.* pointed out that

$$\mathcal{V}(\eta) = \exp\left\{ -\frac{8\eta - 9\eta^2 + 3\eta^3}{(1-\eta)^3} \right\} , \tag{2.16}$$

which corresponds to the well known Carnahan-Starling expression for hard spheres [Carnahan and Starling, 1969]. The fractional available volume described by (2.16) is shown as solid line in Fig. 2.3 (d). We see that this treatment yields $\eta > 1/8$ and consequently predicts achievable Rydberg densities n_r slightly larger than V_{bl}^{-1}. A series expansion of (2.16) in lowest order of η yields $\mathcal{V} = 1 - 8\eta$, which was mentioned above and is shown as dashed line in Fig. 2.3 (d).

Figure 2.4 shows a typical measurement of the excitation suppression of $|55\,S\rangle$ Rydberg atoms as a function of atomic density. The two measurements in Fig. 2.4 were done after different expansion times of the gas and their difference reflects the influence of the excitation volume size. The squares ($200\,\mu$s expansion time) were obtained for in ellipsoidal excitation volume with Gaussian widths $\sigma_x \approx 40\,\mu$m, $\sigma_y \approx 27\,\mu$m, $\sigma_z \approx 27\,\mu$m, whereas the circles ($50\,\mu$s expansion time) were obtained for a volume defined by $\sigma_x \approx 40\,\mu$m, $\sigma_y \approx 16\,\mu$m, $\sigma_z \approx 16\,\mu$m. The Rydberg atom number is corrected by an anticipated detection efficiency of 40% and is in good agreement with the stationary solution of the rate equation model (2.13), using (2.16) and a blockade radius of $R_{\text{bl}} = 5\,\mu$m (solid lines). To fit the data only the absolute Rydberg atom number has been used as free parameter. The ratio between the fit parameter of each dataset is ≈ 2.7 which is in good agreement with the ration between the two excitation volumes ≈ 2.8. The dashed line indicates the anticipated Rydberg atom number ($200\,\mu$s expansion time) for the neglect of interactions.

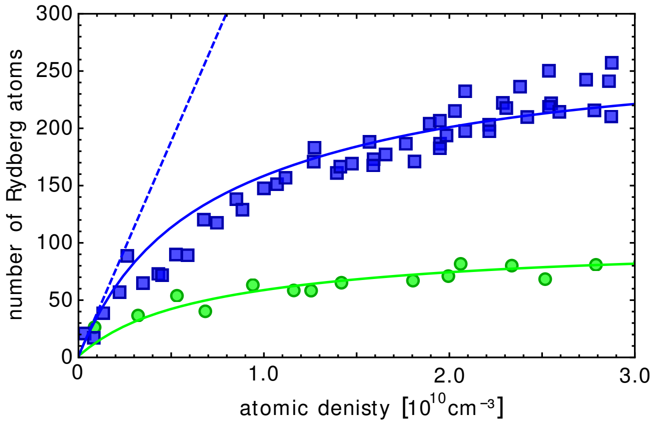

Figure 2.4: Measurement of interaction-induced Rydberg excitation suppression. The plot shows the $|55\,S\rangle$ Rydberg atom number (scaled by the 40% detection efficiency) as a function of the atomic density in the excitation volume. It compares two sets of experiments done for different time-of-flights (squares $\equiv$ $200\,\mu$s; circles $\equiv$ $50\,\mu$s). The solid lines are fits to the data using the stationary solution of the rate equation model (2.13) using (2.16). The dashed line indicates the Rydberg atom number for the neglect of interactions.

The formalism developed here will be used in Ch. 5 to describe the excitation dynamics of a strongly blockaded Rydberg gas prior to its spontaneous avalanche ionization.

2.2.5 Rydberg excitation number statistics

The blockade sphere picture developed in the last section suggested that for high densities the number of Rydberg excitations in the gas is determined by the number of spheres that fit into the excitation volume. In the dense packing limit, the number of Rydberg excitations is fixed and therefore only subjected to minor fluctuations between consecutive experimental runs. This can be seen in the transition from a weakly interacting to a strongly blockaded regime, which is accompanied by a fundamental change in the number distributions of Rydberg excitations from Poissonian to sub-Poissonian character [Cubel Liebisch *et al.*, 2005]. This crossover can be quantified by the Mandel Q parameter [Mandel, 1979]

$$Q = \frac{\langle N_r^2\rangle - \langle N_r\rangle^2}{\langle N_r\rangle} - 1\,, \tag{2.17}$$

where N_r denotes the number of detected Rydberg atoms. Values of $Q > 0$ correspond to super-Poissonian, $Q = 0$ to Poissonian and $Q < 0$ to sub-Poissonian distributions. The latter are evidenced by a characteristic narrowing of the Rydberg excitation number distribution. The extreme, a number- or Fock-state with $Q = -1$ is characterized by the absence of fluctuations. The degree of sub-Poissonian character is thus a measure for the blockade effectiveness.

The Mandel Q parameter can also be related to the spatial correlation function $g^{(2)}(R)$ by

$$Q = 4\pi\, n_r \int \left(\frac{N-1}{N}\, g^{(2)}(R) - 1 \right) R^2 dR\,, \tag{2.18}$$

with N being the total atom number in the excitation volume[iv] [Wüster *et al.*, 2010]. Even though (2.18) is only valid for homogeneous densities and isotropic interactions, it nonetheless underlines the fact that sub-Poissonian counting statistics are intimately connected with the emergence of spatial correlations, reflected by $g^{(2)}(R)$. Based on similar arguments Breyel *et al.* recently developed a statistical method of detecting 'Rydberg crystallization' [Breyel *et al.*, 2012] as discussed in [Gärttner *et al.*, 2012; Ates and Lesanovsky, 2012].

Prior to this thesis there have been two experimental studies that revealed a change in the counting statistics when entering the strong blockade regime. [Reinhard *et al.*, 2008b] exploited a Förster-resonance involving $\left|45D_{5/2}\right\rangle$ states to reach the strong interaction regime and very recently [Viteau *et al.*, 2012] observed sub-Poissonian excitation statistics for attractive interactions with $\left|71D_{3/2}\right\rangle$ states. We address this topic from a slightly different view angle in Ch. 6, where we for the first time provide experimental evidence of sub-Poissonian statistics of Rydberg-interacting dark-state polaritons, which are quasi-particles composed of matter and light [Hofmann *et al.*, 2012].

2.3 Rydberg atom–light interfaces

So far the discussion primarily focused Rydberg–Rydberg interaction effects on the atomic degrees of freedom. In conjunction with these long-ranged interactions is a substantial back-action on the radiation field, which can be explained by considering Rydberg atom–light interactions. The dynamics of such a system — formed by three-level atoms and two coherent optical driving fields — can be described using coupled differential equations, called optical Bloch equations. They are introduced in Sec. 2.3.1 and form the basis of many physical aspects discussed in this thesis. For instance they describe electromagnetically induced transparency [Fleischhauer *et al.*,

---

[iv] A rigorous derivation of Eq. 2.18 can be found in the appendix A of [Ates, 2009].

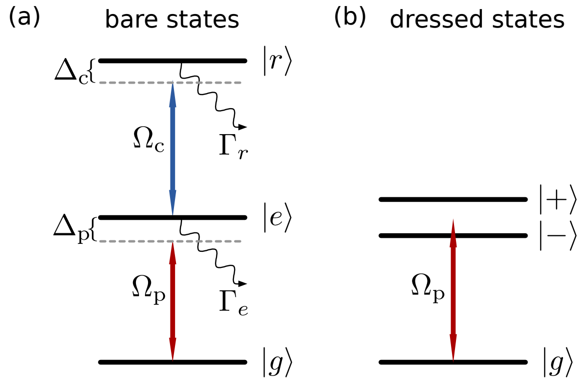

Figure 2.5: Bare and dressed states of a three-level atom. (a) shows a ladder scheme with a ground state $|g\rangle$, a short-lived intermediate state $|e\rangle$, and a (meta) stable state $|r\rangle$ driven by a probe laser (Rabi frequency Ω_{p}) and a coupling laser (Rabi frequency Ω_{c}), respectively. Single photon detunings are indicated by $\Delta_{\mathrm{p,c}}$ and the respective decays are given by $\Gamma_{e,r}$. (b) On resonance ($\Delta_{\mathrm{p}} = 0$) the coupling laser induces a destructive interference of excitation pathways through the doublet of dressed states $|\pm\rangle$. This figure is adapted from [Fleischhauer *et al.*, 2005].

2005], which is a prototypical atom–light interface that is explained in Sec. 2.3.2. Qualitatively new physical effects, discussed in Sec. 2.3.3, arise if one of the coupled energy levels is a Rydberg level which is subjected to sizable and long-range Rydberg–Rydberg interactions. Section 2.3.4 discusses the extension of Rydberg electromagnetically induced transparency to the few-photon level, at which it is characterized by the propagation of coupled excitations of atoms and light, called dark-state polaritons [Fleischhauer and Lukin, 2000].

2.3.1 Optical Bloch equations

Here the Rydberg atom is treated as three-level atom in a ladder-type configuration composed of the ground state $|g\rangle$, the intermediate state $|e\rangle$, and the Rydberg state $|r\rangle$, and depicted in Fig. 2.5 (a). The atom is interacting with two near-resonant laser fields. The lower transition is coherently driven by a *probe laser* with Rabi frequency Ω_{p} and laser detuning Δ_{p}, while the upper transition is coherently driven by a *coupling laser* with Rabi frequency Ω_{c} and a laser detuning Δ_{c}. In the present work we are using Rubidium atoms which have the following level structure:

$$\left|5S_{1/2},\, F=2\right\rangle \quad \xrightarrow[\lambda_{\mathrm{p}}=780\,\mathrm{nm}]{\Omega_{\mathrm{p}}} \quad \left|5P_{3/2},\, F=3\right\rangle \quad \xrightarrow[\lambda_{\mathrm{c}}=480\,\mathrm{nm}]{\Omega_{\mathrm{c}}} \quad |\mathsf{n}\ell\rangle\ , \tag{2.19}$$

with $\ell = 0$ or 2 for $\left|\mathsf{n}S_{1/2}\right\rangle$ or $\left|\mathsf{n}D_{3/2,\,5/2}\right\rangle$ states, respectively.

With the exception of Sec. 2.3.4, both laser fields are considered to be classical light fields, since the majority of atom–light interaction phenomena can be described quantitatively using a semiclassical analysis. We furthermore make the rotating wave approximation through which the atom–light interaction Hamiltonian $\mathcal{H}_{\mathrm{al}}$ of the system is expressed in the rotating frame as the sum of the diagonal atomic Hamiltonian $\mathcal{H}_{\mathrm{a}}$ and the off-diagonal laser coupling Hamiltonian $\mathcal{H}_{\mathrm{l}}$:

$$\mathcal{H}_{\mathrm{al}} = \mathcal{H}_{\mathrm{a}} + \mathcal{H}_{\mathrm{l}} = \frac{\hbar}{2} \begin{pmatrix} 0 & \Omega_{\mathrm{p}} & 0 \\ \Omega_{\mathrm{c}} & 2\Delta_{\mathrm{p}} & \Omega_{\mathrm{c}} \\ 0 & \Omega_{\mathrm{c}} & 2\left(\Delta_{\mathrm{p}} + \Delta_{\mathrm{c}}\right) \end{pmatrix} \tag{2.20}$$

Real atomic systems are subjected to incoherent processes such as the spontaneous emission of photons which cannot be included in (2.20) as an unitary process [Pritchard, 2012]. Instead it is appropriate to use the density matrix formalism to derive a master equation which allows the inclusion of dissipative processes. These processes are described by the so-called Lindblad superoperator $\mathcal{L}(\rho)$, which affects the atomic populations (diagonal elements) and dephases the coherence terms (off-diagonal elements) [Lindblad, 1976]

$$\mathcal{L}(\rho) = \sum_k C_k \rho C_k^\dagger - \frac{1}{2} \sum_k C_k^\dagger C_k \rho + \rho C_k^\dagger C_k \,. \tag{2.21}$$

Here, $\rho = \rho_{ij}$ with $i, j = \{g, e, r\}$ is the 3×3 density matrix of the atom–light system and k is the summation index summing over all possible decay channels of the system, while the collapse operators C_k account for the decay in these channels. In our case they have the form [Haroche and Raimond, 2006]

$$C_{\mathrm{e}} = \sqrt{\Gamma_e}\, |g\rangle \langle e| \,, \tag{2.22a}$$

$$C_{\mathrm{r}} = \sqrt{\Gamma_r}\, |e\rangle \langle r| \,, \tag{2.22b}$$

with the intermediate state decay rate Γ_e and the Rydberg state decay rate Γ_r. Besides the dephasing of the system through spontaneous emission, there are also dephasing mechanisms due to the finite laser linewidths γ_{p} and γ_{c} of the probe and the coupling laser, respectively. These effects can be accounted for by an additional empirical Lindblad operator $\mathcal{L}_{\mathrm{d}}(\rho)$. Since the laser linewidths only affect the coherences while leaving the populations unchanged, the dephasing Lindblad operator is off-diagonal. A derivation and detailed discussion of $\mathcal{L}_{\mathrm{d}}(\rho)$ can be found in § 4.1.1 of [Pritchard, 2012]. Finally the time evolution of the density matrix is calculated using the Liouville-von Neumann equation in the Lindblad form

$$\dot{\rho} = \frac{i}{\hbar} \left[\rho, \mathcal{H}\right] + \mathcal{L}(\rho) + \mathcal{L}_{\mathrm{d}}(\rho) \,. \tag{2.23}$$

The resulting coupled differential equations are commonly referred to as *optical Bloch equations.* For the *noninteracting* three-level atom one obtains six independent coupled differential equations, whereupon three of them are describing the population evolution of the atomic states $|g\rangle$, $|e\rangle$, and $|r\rangle$, while the remaining differential equations identify the dynamics of the coherences. The optical Bloch equations are used throughout this thesis, to describe both the optical response of Rydberg and ground state atomic gases, probed by absorption imaging, as well as the Rydberg population directly accessed by field ionization measurements.

The optical response of atomic systems to the probe laser, is determined by the refractive index $\mathfrak{n} = \sqrt{1+\chi}$. The complex part of the susceptibility χ is responsible for the probe beam absorption by the medium while the real part describes the associated relative phase changes experienced by the light field, when passing through the medium. Thus, we are primarily interested in the susceptibility which is proportional to the density matrix element ρ_{eg}. It has the form [Fleischhauer *et al.*, 2005]

$$\chi(\Delta_\mathrm{p}) = \frac{n|\mu_{eg}|^2}{\epsilon_0 \hbar}\frac{1}{\Omega_\mathrm{p}}\rho_{eg} := a\frac{1}{\Omega_\mathrm{p}}\rho_{eg}\,, \tag{2.24}$$

with the vacuum permittivity ϵ_0 and the optical density a.

To get a qualitative understanding of the complex susceptibility it is instructive to solve for the steady state of optical Bloch equations, which we obtain be equating the left hand side of (2.23) with zero. We further assume negligible dephasing such that $\mathcal{L}_\mathrm{d}(\rho)$ in (2.23) can be dropped. In the weak probe limit for which $\Omega_\mathrm{p} \ll \Omega_\mathrm{c}, \Gamma_e$, one then obtains an analytic expression for χ [Günter *et al.*, 2012]

$$\chi(\Delta_\mathrm{p}) = a\frac{i\Gamma_e}{\Gamma_e - 2i\Delta_\mathrm{p} + \frac{\Omega_\mathrm{c}^2}{\Gamma_r - 2i(\Delta_\mathrm{p}+\Delta_\mathrm{c})}}\,. \tag{2.25}$$

In the absence of the coupling laser (*i.e.* $\Omega_\mathrm{c} = 0$) the system reduces to a two-level (2lv) system with the spectral absorption profile

$$\mathrm{Im}\left\{\chi^{(2\mathrm{lv})}(\Delta_\mathrm{p})\right\} = \mathrm{a}\,\frac{\Gamma_\mathrm{e}^2}{\Gamma_\mathrm{e}^2 - 4\Delta_\mathrm{p}^2}\,, \tag{2.26}$$

which describes a Lorentzian lineshape with the natural linewidth Γ_e.

The next section is devoted to the intriguing effects that arise from the addition of the coupling laser which renders the system more complex but also dramatically enriches the atom–light interaction effects possible with three-level systems. Both the complex part of the susceptibility, describing the medium absorption, and the real part, determining the refractive properties, will be discussed in more detail.

2.3.2 Electromagnetically induced transparency

In the simple case of a three-level atom coherently coupled to two laser fields, interference between excitation pathways [Fano, 1961] has profound consequences for the propagation of the applied optical fields as well as for the atomic state evolution and gives rise to a range of remarkable phenomena. For instance this leads to electromagnetically induced transparency (EIT), in which the presence of the coupling laser can render an otherwise absorbing medium transparent [Harris, 1997; Marangos, 1998; Fleischhauer *et al.*, 2005], and to coherent population trapping (CPT) into a quantum superposition of the atomic states which is independent of the intermediate level [Alzetta *et al.*, 1976; Gray *et al.*, 1978]. For noninteracting atomic gases these phenomena can be understood as single atom effects and have been studied intensively, as they provide a powerful tool for precision spectroscopy [Santra *et al.*, 2005] and nonlinear optics [Harris *et al.*, 1990].

This quantum interference effect is general to three-level systems and is observable in lambda-type, vee-type and ladder systems, provided that the previously introduced state $|r\rangle$ is (meta)stable[v]. The introduction given here is kept general but the end of this section will focus on the special case of Rydberg-EIT which is studied in the context of this thesis. To understand the origin of this phenomenon, it is helpful to investigate the nature of the three dressed eigenstates of the atom–light interaction Hamiltonian introduced in (2.20). Following Bergmann *et al.*, we will express them in terms of so-called mixing angles θ and ϕ that depend on the Rabi frequencies $\Omega_{\mathrm{p,c}}$ and the probe laser detuning Δ_{p} with respect to the intermediate state [Bergmann *et al.*, 1998; Fleischhauer *et al.*, 2005]. On the two photon resonance ($\Delta_{\mathrm{p}} + \Delta_{\mathrm{c}} = 0$) the mixing angles are of the following form

$$\tan\theta = \frac{\Omega_{\mathrm{p}}}{\Omega_{\mathrm{c}}}\,, \tag{2.27a}$$

$$\tan 2\phi = \frac{\sqrt{\Omega_{\mathrm{c}}^2 + \Omega_{\mathrm{p}}^2}}{\Delta_{\mathrm{p}}}\,. \tag{2.27b}$$

The laser-dressed eigenstates can then be written as:

$$|+\rangle = \sin\theta\,\sin\phi\,|g\rangle + \cos\phi\,|e\rangle + \cos\theta\,\sin\phi\,|r\rangle\ , \tag{2.28a}$$

$$|-\rangle = \sin\theta\,\cos\phi\,|g\rangle - \sin\phi\,|e\rangle + \cos\theta\,\cos\phi\,|r\rangle\ , \tag{2.28b}$$

$$|d\rangle = \cos\theta\,|g\rangle - \sin\theta\,|r\rangle\ . \tag{2.28c}$$

---

[v] With lifetimes of several tens of microseconds, Rydberg states $|r\rangle$ are considered stable on the timescales investigated in this thesis.

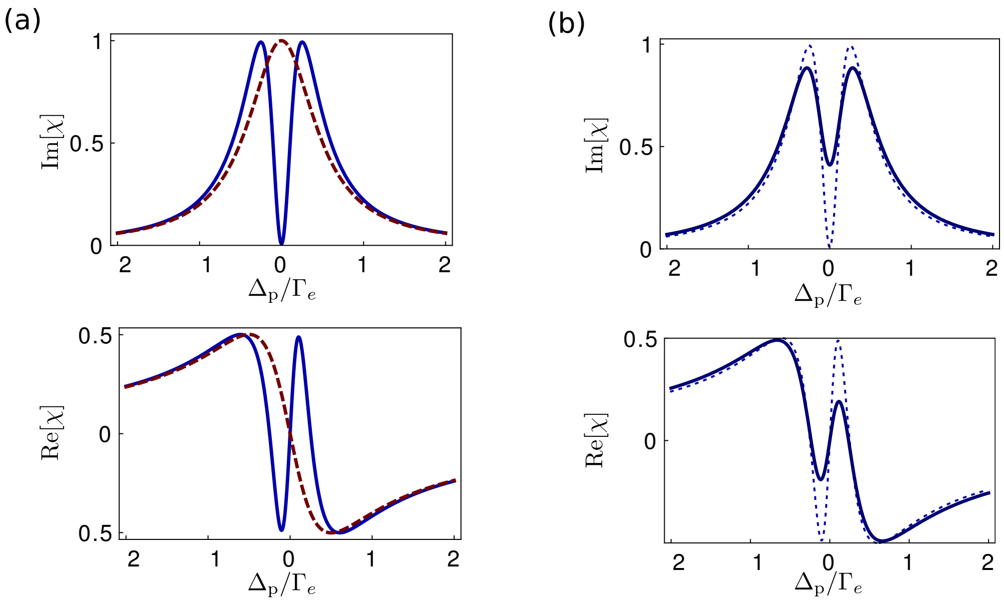

Figure 2.6: Electromagnetically induced transparency. Real and imaginary part of the complex susceptibility χ as a function of the probe laser detuning Δ_p. (a) The optical Bloch equations are numerically solved for the parameters $\Omega_\mathrm{c} = \Gamma_e/2$, $\Omega_\mathrm{p} = \Gamma_e/10$, $\Gamma_r = 0$, $\Delta_\mathrm{c} = 0$. The dashed lines show the optical response of a two-level atom. (b) Influence of finite laser linewidths. The dashed lines are computed with the same parameters as in (a). The solid lines include finite laser linewidth $\gamma_\mathrm{c} = \gamma_\mathrm{p} = 0.04\,\Gamma_e$.

The eigenstates $|\pm\rangle$ contain contributions from all three bare states, in contrast to $|d\rangle$ which has no contribution of the rapidly decaying intermediate atomic state $|e\rangle$ and is thus immune to radiative decay. For the same reason $|d\rangle$ does not couple to the light field and is therefore called a dark state. The transparency induction becomes apparent in the weak probe limit ($\Omega_\mathrm{p} \ll \Omega_\mathrm{c}$). When the probe laser is tuned to resonance ($\Delta_\mathrm{p} = 0$), then the mixing angle $\phi = \pi/4$ such that $|\pm\rangle = 1/\sqrt{2}(|r\rangle \pm |e\rangle)$. In this case the probe laser couples equally well to the $|e\rangle$ component of these two states. As the $|e\rangle$ components in the two states have opposite signs, both excitation pathways will interfere destructively, leading to a cancellation of the optical response on the bare state resonance [Fleischhauer *et al.*, 2005]. Since the $|\pm\rangle$ states are prone to radiative decay ($|e\rangle \rightarrow |g\rangle$), the system is accompanied by an evolution into the dark state $|d\rangle$, which in the weak probe limit ($\theta \rightarrow 0$) coincides with the ground state $|g\rangle$. The EIT effect is visualized in Fig. 2.6 (a), which presents the full optical response — the imaginary and the real part of χ — of a coherently driven three-level system in the weak probe limit. The plotted spectra are numerical solutions to the optical Bloch equation introduced in (2.23) neglecting $\mathcal{L}_\mathrm{d}(\rho)$. The upper part of

Fig. 2.6 (a) compares the normalized absorption of a two-level system (dashed line, compare to (2.26)) with that of a three-level system (solid line) as a function of the probe laser detuning $\Delta_{\rm p}$. It becomes apparent that the presence of the coupling laser dramatically changes the medium properties on resonance from maximum opacity to complete transparency. This effect is associated with a narrow transparency window which becomes narrower with smaller $\Omega_{\rm c}$, resulting in a subnatural linewidth for properly chosen laser parameters.

The lower part of Fig. 2.6 (a) shows the accompanying effects on the refractive properties of the medium which are determined by the real part of the complex susceptibility. Close to resonance we find that the dispersion variation of a three-level system (solid line) markedly differs from the well known anomalous dispersion of two-level systems (dashed line). Instead there is a *normal dispersion* coinciding with the transparency window. Interestingly, the optical response passes through zero, while the slope of the dispersion is steep. This has direct consequences on the propagation velocity of light passing through the EIT medium, as the group velocity is dependent on the dispersion gradient [Fleischhauer *et al.*, 2005]. This fact will be revisited in Sec. 2.3.4 as it has important consequences for the physics dark-state polaritons discussed in Ch. 6.

The idealized picture introduced above becomes more realistic, when including dephasing mechanisms of the two driving lasers. To illustrate the influence of finite laser linewidths, a numerical solution of the complete optical Bloch equations now including $\mathcal{L}_{\rm d}(\rho)$ (see Eq. 2.23) is shown in Fig. 2.6 (b). The upper part of Fig. 2.6 (b) shows an absorption spectrum with included laser linewidth[vi] of $\gamma_{\rm p}/2\pi = \gamma_{\rm c}/2\pi = 0.04\Gamma_e$. We see that dephasing significantly reduces the transparency and slightly broadens the spectrum. The transparency reduction is due to an admixture of the decaying state $|e\rangle$ to the dark state $|d\rangle$ induced via laser dephasing [Pritchard, 2012]. The transparency imperfection is accompanied by a decrease of the normal dispersion as shown in the lower graph of Fig. 2.6 (b). This effect in turn counters the group velocity reduction.

Related phenomena

There are other atom–light interaction effects that are intimately connected with electromagnetically induced transparency. These are stimulated Raman adiabatic passage (STIRAP), coherent population trapping (CPT) and the Autler-Townes

---

[vi] For Rubidium with $\Gamma_e/2\pi = 6.1\,\text{MHz}$, the chosen example corresponds to a laser linewidth $\gamma_{\rm p}/2\pi = \gamma_{\rm c}/2\pi \approx 250\,\text{kHz}$.

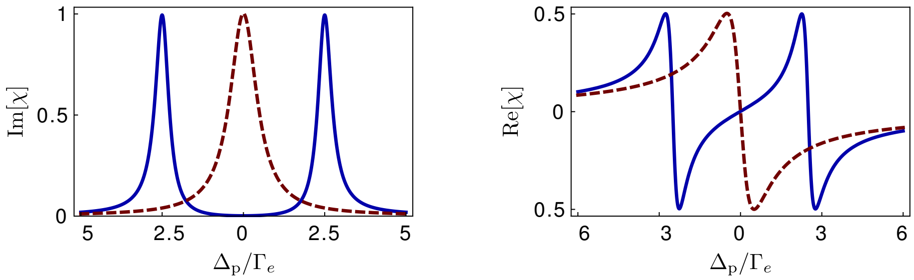

Figure 2.7: Autler-Townes splitting. When the coupling Rabi frequency Ω_c exceeds the intermediate state natural linewidth Γ_e, the absorption profile splits into two distinct lines. This is illustrated for the parameters $\Omega_\mathrm{c} = 5\,\Gamma_e$, $\Omega_\mathrm{p} = \Gamma_e/10$, $\Delta_\mathrm{c} = 0$, and $\Gamma_r = 0$. The latter three parameters are the same as in Fig. 2.6 and the dashed lines again show the two-level response ($\Omega_\mathrm{c} = 0$).

effect. Only the latter two are detailed here, as they are relevant for work presented in this thesis.

(i) **Autler-Townes splitting** — When the coupling Rabi frequency is increased even further, such that $\Omega_\mathrm{c} > \Gamma_e$, the absorption profile splits into two distinct lines corresponding to $|\pm\rangle$, with the energies $\hbar\omega_\pm = \hbar/2(\Delta_\mathrm{p} \pm \sqrt{\Delta_\mathrm{p}^2 + \Omega_\mathrm{p}^2 + \Omega_\mathrm{c}^2})$ [Fleischhauer *et al.*, 2005]. This effect is known as *Autler-Townes splitting* [Autler and Townes, 1955; Cohen-Tannoudji, 1996]. It is depicted in Fig. 2.7, where it is compared to the optical response of a two-level atom. The Autler-Townes effect is related to EIT but the Fano interference connected to EIT becomes negligible for large Ω_c. A recent detailed discussion highlighting the differences between EIT and the Autler-Townes splitting can be found in [Anisimov *et al.*, 2011]. We will exploit the Autler-Townes splitting in Ch. 4, as a means to realize an interaction-induced resonant excitation, to give experimental evidence for the antiblockade effect.

(ii) **Coherent population trapping** — Earlier it was mentioned that the $|\pm\rangle$ states are subjected to radiative decay ($|e\rangle \rightarrow |g\rangle$), which can pump population into the dark state $|d\rangle$. As the dark state does not couple to the light field, the population will remain trapped in this quantum superposition of the atomic states. This phenomenon is called *coherent population trapping* (CPT) and was first observed by [Alzetta *et al.*, 1976; Arimondo and Orriols, 1976] and is reviewed in [Arimondo, 1996]. Dependent on the laser parameters this superposition state can contain a sizable Rydberg population which can be measured by means of field ionization [Schempp *et al.*, 2010].

2.3.3 Interaction effects on Rydberg electromagnetically induced transparency

More recently, it has been recognized that the combination of EIT and highly excited Rydberg states opens up new perspectives [Mohapatra *et al.*, 2007]. Theoretically, strongly interacting Rydberg atoms driven in an EIT-configuration were shown to enable the generation of many-atom entanglement [Müller *et al.*, 2009] and of non-classical light [Gorshkov *et al.*, 2011; Sevinçli *et al.*, 2011b; Petrosyan *et al.*, 2011]. Meanwhile experiments have been undertaken to study first effects of Rydberg–Rydberg atom interactions on EIT [Weatherill *et al.*, 2008; Mohapatra *et al.*, 2008; Raitzsch *et al.*, 2009; Pritchard *et al.*, 2010] and CPT [Schempp *et al.*, 2010].

To see how Rydberg–Rydberg interactions affect the previously discussed atom–light interaction phenomena like EIT, CPT or the Autler-Townes effect, it is instructive to describe the system as an interacting two-atom system. In the atom pair basis $\{|gg\rangle, |ge\rangle, |eg\rangle, |ee\rangle, |gr\rangle, |rg\rangle, |er\rangle, |re\rangle, |rr\rangle\}$ the atom–light interaction Hamiltonian $\mathcal{H}_{\text{al}}$ introduced in (2.20) is then expressed as a 9×9 matrix. To account for the Rydberg–Rydberg interaction, the Hamiltonian is extended by a Rydberg interaction Hamiltonian $\mathcal{H}_{\text{int}}$ of the form $\mathcal{H}_{\text{int}} = U_{\text{int}}(R)\,|rr\rangle\langle rr|$, where $U_{\text{int}}(R) = -C_6/R^6$ is the van der Waals interaction between two Rydberg atoms. To obtain the *two-atom* optical Bloch equations, the Lindblad superoperator $\mathcal{L}(\rho)$ and the laser dephasing operator $\mathcal{L}_{\text{d}}(\rho)$ have to be adapted accordingly, which finally leads to 45 independent coupled differential equations for the density matrix elements of the Rydberg interacting atom–light system.

The two-atom optical Bloch equations will be used in Ch. 4 because they allow for a simple distinction between noninteracting pair states with single Rydberg contribution ($|gr\rangle, |rg\rangle, |er\rangle$, and $|re\rangle$) and interacting Rydberg pair states ($|rr\rangle$). In this way interaction effects on the Rydberg population can be distilled out which is used to model an interaction-induced asymmetry of the two Autler-Townes components. The latter turns out to be a manifestation of the antiblockade.

For two interacting atoms, the Rydberg–Rydberg interaction has already profound consequences on the atom dark state $\left|d^{(2)}\right\rangle$. Due to the interactions it cannot be expressed as a simple product state of two single atom dark states $\left|d^{(2)}\right\rangle \neq |d\rangle \otimes |d\rangle$, where $|d\rangle$ was introduced in (2.28). As pointed out by Møller *et al.*, the two interacting atoms, nevertheless, possess two dark states $\left|d^{(2)}\right\rangle$, where one of them has the form [Møller *et al.*, 2008]

$$\left|d^{(2)}\right\rangle = \frac{(\cos^2\theta - \sin^2\theta)\,|gg\rangle - \sin\theta\,\cos\theta(|gr\rangle + |rg\rangle) + \sin^2\theta\,|ee\rangle}{\sqrt{\cos^4\theta + 2\sin^4\theta}}\,. \tag{2.29}$$

These entangled dark states are dissipative due to the admixture of the intermediate, decaying state $|e\rangle$, but are still significantly populated by optical pumping. Interestingly, they do not contain the state $|rr\rangle$ and are thus immune to interactions. As a consequence, the dark-state resonance does not shift with increasing interaction which affects both the Rydberg-CPT line and the light transmission on the EIT resonance.

We have experimentally investigated this effect in the case of coherent population trapping with controlled inter-particle interactions, for which we observed a non-shifted dark-state resonance without significant broadening [Schempp *et al.*, 2010]. For sizable Rydberg population ($\Omega_\mathrm{p} > \Omega_\mathrm{c}$) we have measured the narrow Rydberg excitation line arising from CPT by directly probing the Rydberg population ($\propto \rho_{rr}$) with field ionization. Similar effects were at the same time seen in a Rydberg EIT medium subjected to long-range interactions, for which measurements of the probe laser transmission in the weak excitation regime ($\Omega_\mathrm{p} < \Omega_\mathrm{c}$) gave direct information about the probe beam optical susceptibility χ [Pritchard *et al.*, 2010]. At higher atom densities both experiments furthermore discovered a diminishing contrast of the dark resonance, the reason of which will be explained shortly.

When the atomic density is increased, the system undergoes a transition from an interacting pair system to a multiparticle system, in which cooperative effects start to play a role, as more and more atoms accumulate within a blockade sphere. This emphasizes that a more sophisticated many-body theory is required. Indeed we found out that the occurrence of entangled dark states in the two-body model already suggests that the interaction-induced correlations between the atoms cannot be accounted for by a mean-field model which would predict both a broadening and a shift of the dark-state resonance [Schempp *et al.*, 2010]. For atomic densities of $n = 10^{10}\,\mathrm{cm}^{-3}$ and a blockade radius of $R_\mathrm{bl} = 6\,\mu\mathrm{m}$ Pritchard *et al.* found quantitative agreement between the experiment and a three-atom cooperative model which can be understood as three-body optical Bloch equations [Pritchard *et al.*, 2010]. Our experimental findings were explained with a reduced density matrix expansion developed by S. Sevinçli and T. Pohl. The theory, accounting for the dynamics of inter-particle correlations within a blockade sphere, provides an accurate description of the excitation dynamics for the investigated atomic density range from $n \approx 7 \times 10^8\,\mathrm{cm}^{-3} - 7 \times 10^9\,\mathrm{cm}^{-3}$ [Schempp *et al.*, 2010].

The dark state expressed in (2.29) also reveals another interesting feature which was pointed out in [Pritchard *et al.*, 2010]. $\left|d^{(2)}\right\rangle$ suggests that the system is in a superposition in which due to the excitation blockade only one atom can be excited to the Rydberg state and thereby solely contributes to the transparency. The other

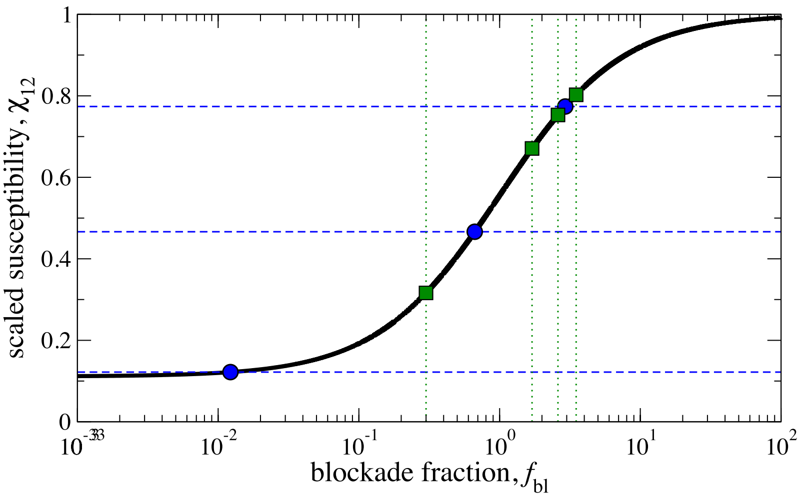

Figure 2.8: Universal relation between the scaled susceptibility $\tilde{\chi} = \chi/\chi^{(2\mathrm{lv})}$ and the fraction f_{bl} of interaction-blocked Rydberg excitations. The horizontal and vertical lines mark the measurements of the blockade fraction (dotted lines), [Schempp *et al.*, 2010] and of the probe beam transmission (dashed lines), [Pritchard *et al.*, 2010], respectively. The squares and circles only highlight the intersection with the theory curve, but *do not* represent data points. The figure is taken from [Sevinçli *et al.*, 2011a] and replotted with permission of S. Sevinçli.

atom acts as a two-level atom which resonantly couples to the probe laser, resulting in a transparency reduction on resonance. The blockade forms a collective state for which the single Rydberg excitation is shared between the two atoms. As more atoms are included in the blockade sphere, the single excitation is shared across a larger number of atoms, further suppressing the transmission on resonance.

This effect is illustrated in Fig. 2.8 which is taken from a joint publication with Sevinçli *et al.* and shows the dependence of the the scaled susceptibility $\tilde{\chi} = \chi/\chi^{(2\mathrm{lv})}$ upon the blockade fraction $f_{\mathrm{bl}} = n_r^{(0)}/n_r - 1$ [Sevinçli *et al.*, 2011a]. Here $\chi^{(2\mathrm{lv})}$ expresses the susceptibility of a two-level (2lv) atom, while $n_r^{(0)}$ describes the Rydberg density for vanishing interactions. The solid line in Fig. 2.8, which is the result of a Monte-Carlo rate equation approach developed by C. Ates, S. Sevinçli, and T. Pohl, connects both our CPT measurements [Schempp *et al.*, 2010], as well as the EIT measurements by [Pritchard *et al.*, 2010]. The theory furthermore suggests a simple universal relationship between the scaled susceptibility and the blockade fraction [Ates *et al.*, 2011]

$$\tilde{\chi} = \frac{f_{\mathrm{bl}} + \tilde{\chi}^{(0)}}{1 + f_{\mathrm{bl}}}\,, \tag{2.30}$$

were $\tilde{\chi}^{(0)}$ denotes the scaled susceptibility for noninteracting atoms arising from the finite linewidth of the excitation lasers (compare to Fig. 2.6 (b)). Most importantly, the strong Rydberg–Rydberg atom interactions result in huge dissipative optical nonlinearities, demonstrating the great potential of Rydberg-EIT media for applications in quantum optics [Sevinçli *et al.*, 2011b; Pritchard *et al.*, 2012].

An experimental verification of this universal scaling behavior is extremely challenging, since it asks for the comparison of two *locally* measured quantities, the scaled susceptibility $\tilde{\chi}$ and the blockade fraction f_{bl}. The latter is difficult to measure as a Rydberg population measurement via field ionization is always connected to an ensemble averaged measurement, as will be emphasized in Sec. 3.7.2, when investigating the combined ion and optical detection of Rydberg atoms. We will however experimentally demonstrate the optical nonlinerity in Ch. 6, where we analyze the transparency of a Rydberg EIT medium, varying the atomic density over almost four orders of magnitude, thereby accumulating more and more atoms inside the blockade spheres. We will show that the measurements are in good agreement with Monte-Carlo simulations which include the attenuation of the probe light as it propagates through the cloud.

2.3.4 Dark-state polaritons

In Sec. 2.3.2 it was mentioned that concomitant to the transparency there is a sizable linear dispersion, which can lead to a substantial reduction of the group velocity resulting in slow light. This was impressively demonstrated in a sodium BEC allowing a velocity reduction of a light pulse down to 17 m/s [Hau *et al.*, 1999]. The physics of slow light propagation in EIT media is associated with the existence of quasi-particles called *dark-state polaritons*, which can be understood in a quantum mechanical picture in which the probe field is treated quantum mechanically and assumed to be composed of individual photons [Mazets and Matisov, 1996; Fleischhauer and Lukin, 2000]. In the presence of a strong coupling field, a single probe photon will be partially converted into a collective excitation of the medium and forms a dark-state polariton [Fleischhauer and Lukin, 2002]

$$|D,1\rangle = \cos\vartheta\,|G,1\rangle - \sin\vartheta\,|R,0\rangle\ , \tag{2.31}$$

where the collective quantum states involving N atoms and the light field are

$$|R,0\rangle = \frac{1}{\sqrt{N}}\sum_i |g_1,\cdots,r_i,\cdots,g_N\rangle\,|0\rangle\ , \tag{2.32a}$$

$$|G,1\rangle = |g_1,\cdots,r_i,\cdots,g_N\rangle\,|1\rangle\ . \tag{2.32b}$$

The mixing angle

$$\tan\vartheta = \frac{\sqrt{n\sigma c\Gamma_e}}{\Omega_\mathrm{c}} = \sqrt{\mathfrak{n}_\mathrm{g}}\,, \tag{2.33}$$

determines the properties of the polariton depending on the atom density n, the resonant scattering cross-section $\sigma = 3\lambda^2/2\pi$ and the speed of light c.

Outside the medium (*i.e.* $n = 0$ and hence $\vartheta = 0$) the polariton possesses entirely photonic character and therefore travels with the speed of light. This changes as soon as the polariton enters the medium where it experiences the large linear dispersion. The finite atomic density n of the medium changes the mixing angle such that the polariton looses part of its electromagnetic nature while acquiring matter-like character. It propagates through the atomic medium with negligible loss and reduced group velocity

$$v_\mathrm{g} = \frac{c}{1+\mathfrak{n}_\mathrm{g}} \approx c/\tan^2\vartheta\,, \tag{2.34}$$

which is proportional to the magnitude of its photonic component [Lukin and Imamoglu, 2001]. Once the dark-state polariton has left the medium it is accelerated back to the speed of light and has again purely photonic character.

For typical densities reached in ultracold gases, the polariton is almost entirely matter-like and it seems natural that it can adopt matter properties. For instance it becomes a 'mass-like' particle which provides an intuitive picture for the dramatically reduced group velocity $v_\mathrm{g} \ll c$. Other examples for the adoption of matter properties are for instance, the imprint of a magnetic moment onto a light field [Karpa and Weitz, 2006] or the realization of giant electro-optical effects based on the exaggerated polarizability of Rydberg atoms [Mohapatra *et al.*, 2008]. Qualitatively new effects are expected when coupling light to a strongly interacting atomic system. Polariton–polariton interactions mediated by the atomic admixture can lead to highly nonlinear and nonlocal effects [Sevinçli *et al.*, 2011b] as well as the emergence of correlations in both the atomic and the light fields [Gorshkov *et al.*, 2011; Petrosyan *et al.*, 2011; Peyronel *et al.*, 2012]. In Ch. 6 we will discuss the experimental realization of strongly interacting Rydberg dark-state polaritons whereby the blockade effect gives rise to dissipative hard-core interactions between dark-state polaritons.

Chapter 3

Experimental Setup and Rydberg atom detection

This chapter is based on the following manuscript:

Combined ion and optical detection of Rydberg atoms in dense ultracold atomic gases
C.S. Hofmann, G. Günter, H. Schempp, N. L. M. Müller, A. Faber, H. Busche,
M. Robert-de-Saint-Vincent, S. Whitlock, M. Weidemüller
in preparation

Recent developments in the physics of ultracold Rydberg gases demand a high level of experimental sophistication combining high atomic and optical densities with excellent control of external fields and precise Rydberg atom detection. This chapter describes our new experimental system which was designed and built in the framework of this thesis. The key components of the setup, which are specific to Rydberg physics are outlined in Sec. 3.1 and detailed in the subsequent sections. The system operates at fast duty cycles thanks to a high flux cold atom source (Sec. 3.3) and a three beam optical dipole trap (Sec. 3.4). The latter permits accurate tuning of atomic densities and efficient all-optical preparation of Bose-Einstein condensates as detailed in Sec. 3.5. The centerpiece of the apparatus is an electrode structure that surrounds the Rydberg gas and allows for precise electric field control and field ionization of Rydberg atoms combined with subsequent charged particle detection as explained in Sec. 3.6. Owing to its high degree of optical access, the system also renders the spatially resolved optical probing of Rydberg state properties possible, by making use of Rydberg state EIT. The combination of these two detection

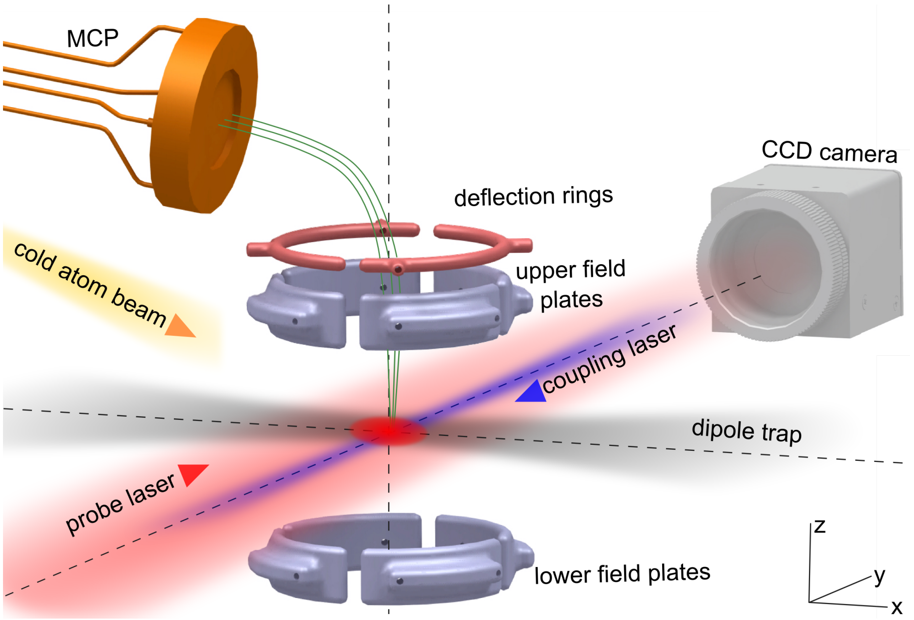

Figure 3.1: Experimental system for Rydberg physics in dense ultracold atomic gases. (a) A high flux cold atom beam loads a magneto-optical trap (not shown). The pre-cooled atoms are subsequently transferred into an optical dipole trap for evaporative cooling. After trap release the atoms are excited to high-lying Rydberg states by a $780\,\mathrm{nm}$ probe laser and a counter-propagating $480\,\mathrm{nm}$ coupling laser. An electrode structure is used for precise electric field control and for field ionization of Rydberg atoms. Guiding fields produced by two deflection rings direct the resulting ions (green trajectories) onto a micro-channel plate (MCP) detector. Optical detection with a CCD camera done in parallel provides complementary information, using Rydberg-EIT.

techniques has not been realized previously. It provides a powerful new tool giving complete access to macroscopic as well as microscopic properties of strongly interacting Rydberg gases, as discussed in Sec. 3.7.

3.1 Experimental system for dense ultracold Rydberg gases

The key components of our new experimental system are summarized in the schematic diagram depicted in Fig. 3.1. The fact that Rydberg atoms are sensitive to stray fields caused by the presence of even a few ions [Comparat and Pillet, 2010] has to be considered in the implementation of the cold atom source of the experiment: it is advantageous to isolate the cold atom source from the main experimental chamber.

This is particularly simple with two-dimensional magneto-optical traps (2D-MOTs), since the cooling mechanism and the transmission through the differential pumping tube are exclusive to the designated atomic species [Dieckmann *et al.*, 1998]. Thus 2D-MOTs are entirely ion free sources, making them ideally suited for experiments with Rydberg atoms. Providing atom beams with similar atom fluxes as Zeeman slowers, they have the major advantage that they are compact and can be implemented at nearly any orientation angle with respect to the magnetic gradient fields of the magneto-optical trap (MOT). This provides a simple means to maximize the optical access to the science chamber. Exploiting transversal cooling, 2D-MOTs furthermore provide slow atomic beams of minimum divergence and high beam luminosity which set the basis for experiments with high repetition rates, as the MOT loading time can be significantly shortened.

Once the MOT is loaded, the pre-cooled atoms are directly transferred into an optical dipole trap to all-optically prepare dense atomic samples [Grimm *et al.*, 2000], which are then laser excited to Rydberg states. To study their mutual interactions, it is necessary to vary their average inter-atomic separation (compare Fig. 2.2). This is done by forced evaporative cooling which allows for precise density and temperature tuning of atomic gases and permits Bose-Einstein condensation, if required. As compared to magnetic traps [Löw *et al.*, 2007; Dubessy *et al.*, 2012], dipole traps are unrestricted to the used spin states and offer fast experimental duty cycles as well as instant trap switch-off. Moreover optical dipole traps permit flexible trap geometries and have only minor effect on the optical access.

In Sec. 2.1 it was mentioned that Rydberg atoms experience sizable Stark shifts $\Delta U = \alpha\mathcal{E}^2/2$ in electric fields $\mathcal{E}$ because their atomic polarizability α scales with the principal quantum number as $\mathsf{n}^{\star 7}$. The $|55S\rangle$ Rydberg state, used most frequently in this thesis, for instance exhibits a polarizability of $\alpha \approx -100\mathrm{MHz}/(\mathrm{V/cm})^2$ [O'Sullivan and Stoicheff, 1985] and an intrinsic linewidth of $\approx 2\pi \times 10\,\mathrm{kHz}$ [Beterov *et al.*, 2009b]. Thus an electric field of $\mathcal{E} = 1\mathrm{V/cm}$ already causes a lineshift exceeding more than 600 linewidths. On the one hand the electric field sensitivity of Rydberg atoms naturally asks for precise field control as a prime requirement of a Rydberg apparatus. On the other hand the application of moderate electric fields offers exceptional manipulation possibilities ranging from the tuning of interactions with Förster resonances [Vogt *et al.*, 2006; Westermann *et al.*, 2006; Ryabtsev *et al.*, 2010; Nipper *et al.*, 2012; Gurian *et al.*, 2012] or the induction of permanent electric dipole moments with homogeneous fields [Vogt *et al.*, 2007] to the realization of spatially resolved Stark shifts with gradient fields [Mülken *et al.*, 2007]. That is why a specially designed electrode structure fulfilling the above requirements was designed. The electrode structure, shown in Fig. 3.1, also allows for field ionization of Rydberg atoms and subsequent charged particle detection, which is so far the most frequently used Rydberg detection technique.

The good optical access of our setup qualifies for optical absorption imaging with a charged coupled device (CCD) camera. We extend this well established technique to the probing of Rydberg states by exploiting Rydberg state electromagnetically induced transparency as introduced in Sec. 2.3.3. This is possible because EIT allows to map the properties of the Rydberg state onto the light field, giving rise to a spatially resolved information which not only provides a local probe but also offers a powerful tool to analyze hundreds of EIT-systems (mapped onto hundreds of pixels) in parallel. *Combined* with field ionization, this makes for an ideal tool for accessing microscopic and macroscopic properties as well as the dynamics of strongly interacting Rydberg gases.

After having outlined the most important features of the new setup, the core components are now detailed in the sections below.

3.2 Vacuum system

The technical realization of our new experimental apparatus is shown in Fig. 3.2 which gives an overview over the vacuum system and the periphery of the science chamber. The vacuum system is designed as a dual chamber system in which the atom source (①) is pressure separated form the science chamber (②), which encloses the electrode structure. The science chamber is based on a commercial 'spherical square' stainless steel chamber[i] which provides excellent optical access thanks to eight openings perpendicular to the symmetry plane of the chamber, which is chosen as horizontal plane of our experiment. The openings are sealed with diffusion bonded nonmagnetic viewports[ii]. To eliminate thermal lensing in high power laser applications, Suprasil 3001 is chosen as viewport glass, which has nearly no OH absorption bands up to 2600 nm [Carpenter *et al.*, 2012]. In particular at the dipole trap wavelength 1064 nm the absorption is as low as 0.25 ppm/cm. All windows are anti reflection coated at the principal wavelengths of our experiment (780 nm, 480 nm, and 1064 nm) to reduce reflection.

To achieve ultra high vacuum with a pressure $< 1 \times 10^{-11}$ mbar, we use custom-made nonevaporable getter coating [Benvenuti *et al.*, 1999] in combination with a

---

[i] Kimball Physics; 8 Multi-CF Spherical Square MCF800-SS204040.16

[ii] The viewports are manufactured by UKAEA.

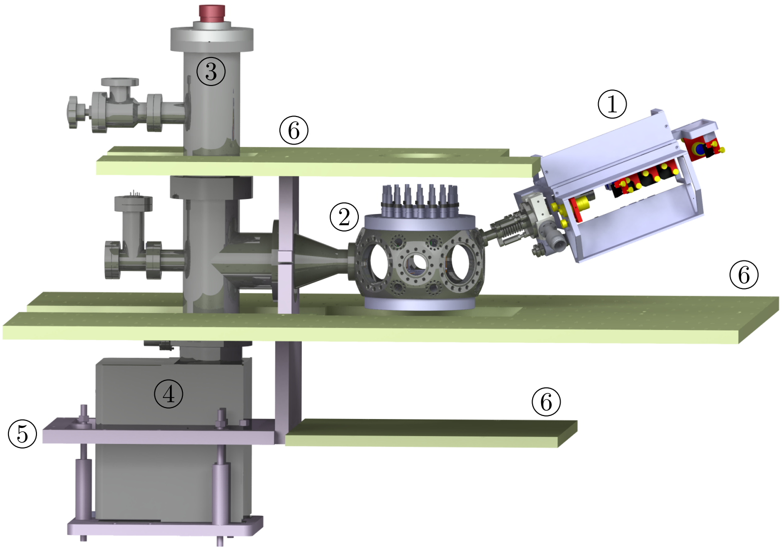

Figure 3.2: Technical overview over the vacuum chamber. The system is designed as dual chamber vacuum system with the atom source ①, the science chamber ② and the titan sublimation pump ③ and the 125 l ion pump ④. A mounting structure ⑤ is recessed into the optical table (not shown) and supports the entire setup. Optical breadboards ⑥ are used to mount the optical elements.

titanium sublimation pump[iii] (③) and a continuously operated 125 l/s ion getter pump[iv] (④) to evacuate the chamber periphery. A mounting structure (⑤) which is recessed into the optical table supports the vacuum system in its center of mass and in the same time provides anchorage points for optical breadboards (⑥) on which all optical elements are mounted.

3.3 Cold atom source

Our 2D-MOT is housed in a 140 × 35 × 35 mm glass cell[v] and is pressure separated from the science chamber by a differential pumping stage. Dispensers inside the glass cell provide a Rubidium background vapor, whose vapor pressure is adjustable via the applied dispenser current. The dispensers[vi] are 98% isotope enriched with ^{87}Rb to minimize the ^{85}Rb vacuum contamination in the glass cell. To maintain good optical access to the science chamber, the 2D-MOT is attached under an angle

---

[iii] Agilent Technologies; TSP Cartridge Filament Source

[iv] Agilent Technologies; VacIon Plus 150 Ion Pump StarCell

[v] The glass cell is AR coated (780 nm) on the outer cell walls and manufactured by Japan Cell.

[vi] Alvatec; ALVASOURCES – Chormate-free metal vapor sources, AS-3-Rb87(98%)-20-F

of 20° with respect to the horizontal plane of the experiment. We designed a compact $200 \times 200 \times 350$ mm fiber based cage system to minimize the space consumption of the 2D-MOT. It is depicted in Fig. 3.3 (a) and provides 780 nm laser light and magnetic quadrupole fields required for two-dimensional cooling and trapping. Adjustment bellows, connecting the glass cell and the science chamber, can be used to align the atom beam with respect to the science chamber center, without changing any optical alignment.

The cage system is divided in two perpendicular cooling planes which intersect in the symmetry axis of the glass cell. A cross-section through one of these planes is shown in Fig. 3.3 (b) which shows the fiber coupler, the polarization optics, and the retro-reflection optics for the realization of three equally spaced cooling regions. The multiple-stage design is similar to a design by Ramirez-Serrano *et al.* and effectively works as one long trap region [Ramirez-Serrano *et al.*, 2006]. We verified this with atom trajectory simulations revealing that atoms in one trapping region are efficiently coupled into adjacent regions, while atoms with higher velocities can also be captured by passing through more than one trapping region [Höltkemeier, 2011]. A second fiber coupler is used to generate a 7 mm diameter pushing beam, which propagates along the symmetry axis and guides the pre-cooled atoms through the 800 μm exit hole of the differential pumping stage into the science chamber.

Figure 3.4 illustrates the realization of the magnetic trapping fields. Following Tiecke *et al.*, we use permanent neodymium bar magnets that are arranged in two units with six magnets to provide a two-dimensional quadrupolar field which extends over the total length of the three trapping regions (see Fig. 3.4 (a)) [Tiecke *et al.*, 2009]. Both bar magnet units lie in a plane which bisects the two laser cooling planes as illustrated in Fig. 3.4 (b). The separation between the two units can be incrementally decreased to change the field gradient from ≈ 13 G/cm to ≈ 20 G/cm as shown in Fig. 3.4 (c). Best results were obtained with a field gradient of 16 G/cm which is constant over ≈ 10 cm, covering all three cooling regions.

The 2D-MOT described here, has been rigorously characterized in the framework of two Diploma-Theses [Höltkemeier, 2011; Busche, 2011]. B. Höltkemeier primarily focused on the properties of the cold atomic beam, since a 2D-MOT can also serve as a novel target for recoil ion momentum spectroscopy experiments as described in our recent publication [Götz *et al.*, 2012]. The second Diploma-Thesis by H. Busche investigated the MOT loading characteristics in detail, such that only its most important aspects are summarized here. For routine operation we use the following parameters that have been optimized for maximum MOT loading rates. We typically use 80 mW total cooling laser power and 3 mW total repumping laser

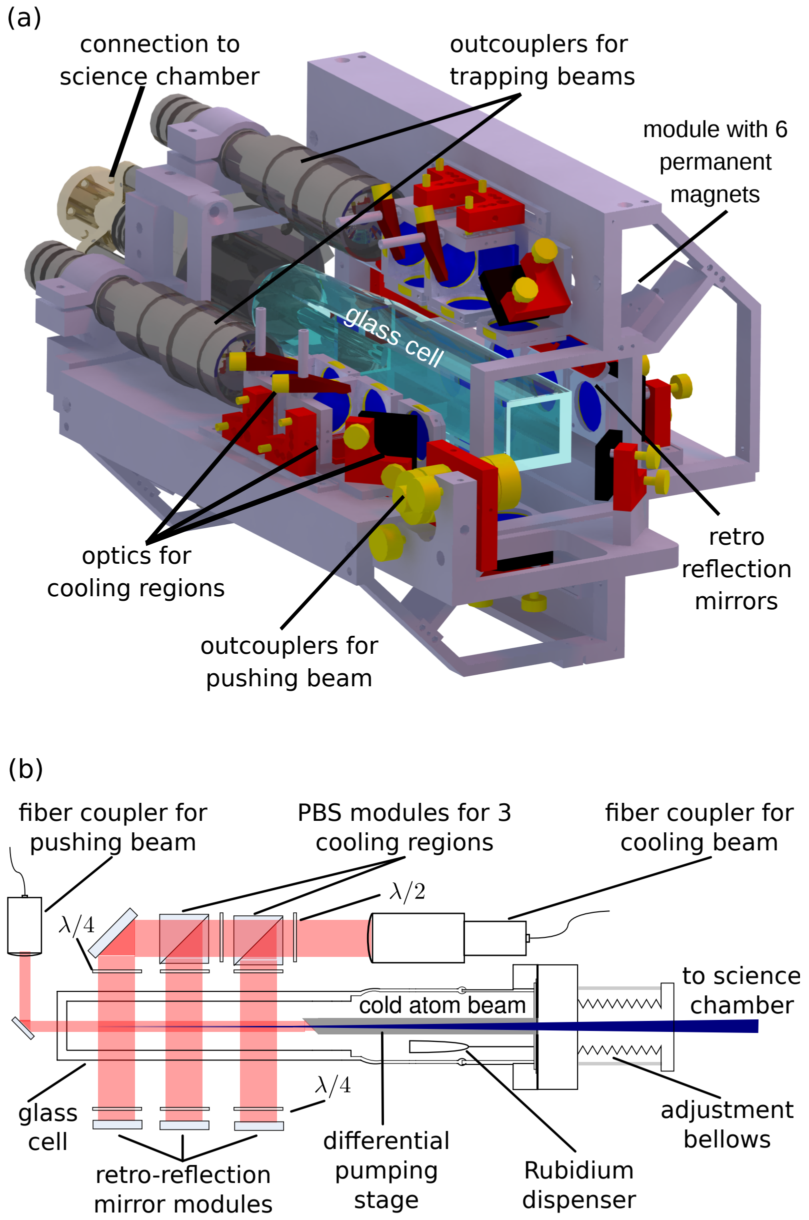

Figure 3.3: Technical overview over the 2D MOT cage system (a) The glass cell is surrounded by an attachable and externally adjustable, fiber based 2D-MOT cage system. It provides polarization and retro-reflection optics as well as permanent magnets for three cooling regions. A cross-section through one of the cooling planes is shown in (b). Dispensers provide Rubidium vapor for laser cooling. Polarizing beam splitters (PBS) and waveplates ($\lambda/2$, $\lambda/4$) divide cooling light from a fiber coupler into three cooling regions. A fiber based pushing beam directs the resultant cold atomic beam through the differential pumping stage towards the science chamber.

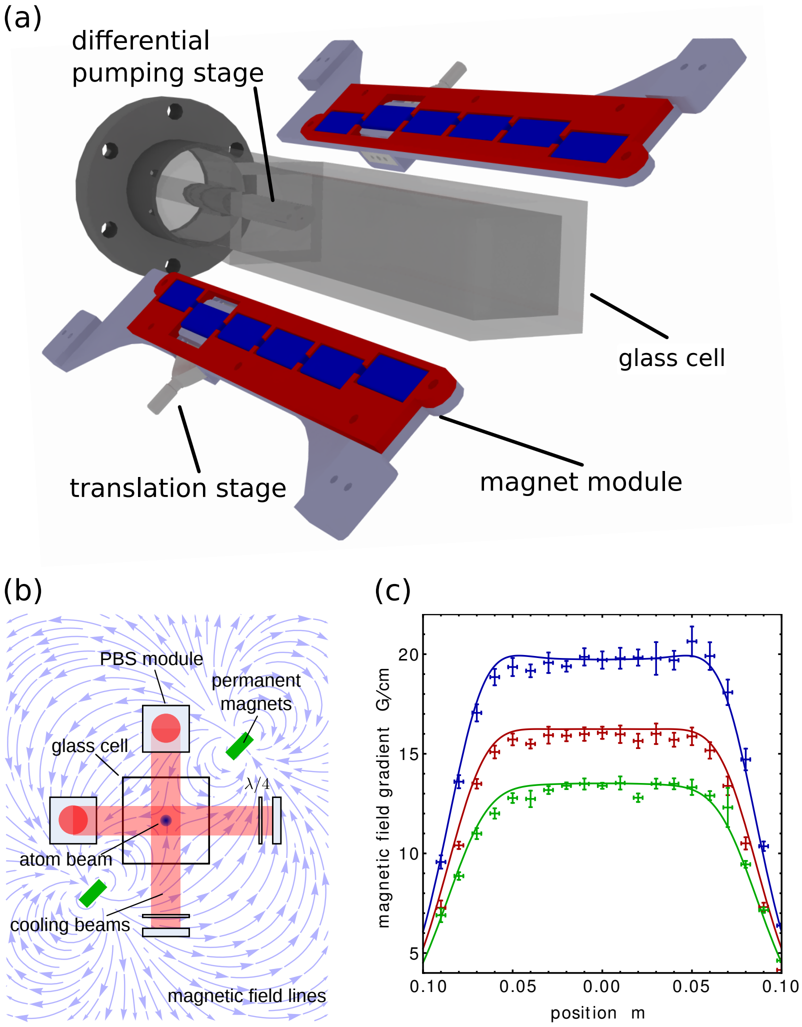

Figure 3.4: Magnetic field design of the 2D-MOT. (a) Technical drawing of the bar magnet units. The cage system is not shown for clarity. (b) cross-section through a plane perpendicular to the symmetry axis of the glass cell, illustrating the magnetic quadrupole field which is indicated by the blue arrows. (c) Magnetic field gradients as a function of symmetry axis position. The three measurements correspond to three different separations between the two bar magnet units. Horizontal error bars represent a positioning uncertainty due to the Hall probe thickness, while vertical error bars correspond to 95% confidence intervals of the linear fit determining the field gradient. Solid lines represent calculated gradients for a magnetization of $9.1\,\mathrm{A/m}$.

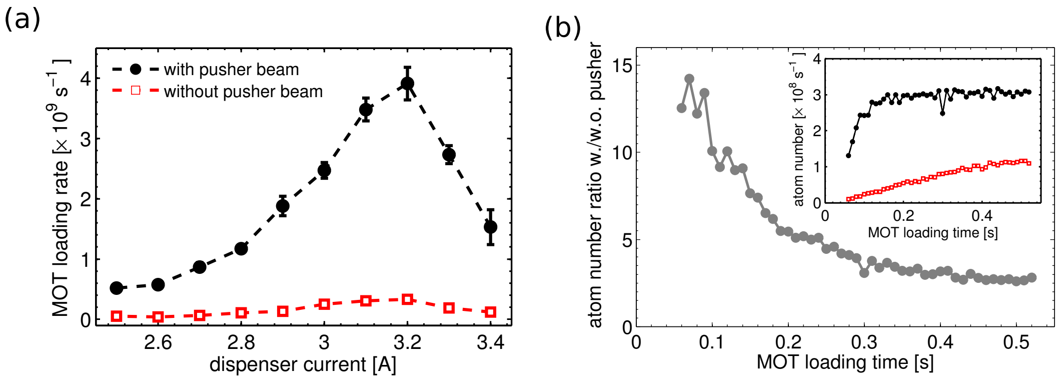

Figure 3.5: 2D-MOT performance. (a) Dependence of the loading rate on the ^{87}Rb dispenser current. The maximum loading rate of $(3.9 \pm 0.5) \times 10^9 \mathrm{s}^{-1}$ is reached for a current of $3.2\,\mathrm{A}$. We observe a loading rate increase of a factor 12 ± 2 when operating the 2D-MOT with pushing beam. All measurements were taken after $0.1\,\mathrm{s}$ of MOT loading. (b) MOT loading dynamics. The main graph shows performance increase through pushing beam operation. The according MOT loading curves with and without pushing beam operation are shown in black and red, respectively, in the inset. All lines plotted through the data are guides to the eye.

power. The circularly polarized cooling laser is $9\,\mathrm{MHz}$ ($\approx 1.5\,\Gamma_e$) red detuned from the $\left|5S_{1/2}, F=2\right\rangle \rightarrow \left|5P_{3/2}, F=3\right\rangle$ cooling transition and the co-propagating repumping laser is resonant with the $\left|5S_{1/2}, F=1\right\rangle \rightarrow \left|5P_{3/2}, F=2\right\rangle$ transition. A detailed description of our laser system can be found in [Busche, 2011] and the used laser locking schemes are described in [Schnellbächer, 2010]. The atom flux is further increased by separately adjusting the pushing beam detuning to redirect atoms traveling away from the science chamber. At the expense of comparatively high laser pushing beam powers ($40\,\mathrm{mW}$), we use a pusher beam detuning of $-43\,\mathrm{MHz}$ ($\approx 7\,\Gamma_e$) with respect to the cooling transition, which allows us to address atoms with velocity classes in the range of $[0, -45\,\mathrm{m/s}]$ that would otherwise not contribute to the atom flux [Höltkemeier, 2011].

Figure 3.5 illustrates the performance of the 2D-MOT which was evaluated with absorption images taken at different times throughout the MOT loading phase. Figure 3.5 (a) shows the MOT loading rate determined during the first $100\,\mathrm{ms}$ of MOT loading as a function of the Rubidium dispenser current. Changing the dispenser current offers a simple way to control the Rubidium vapor pressure, which strongly influences the atomic flux and in turn the MOT loading rate. A maximum loading rate of $(3.9 \pm 0.5) \times 10^9\,\mathrm{s}^{-1}$ (black data points) is found for a dispenser current of $3.2\,\mathrm{A}$, while the flux is throttled for higher dispenser currents. This is consistent with [Dieckmann *et al.*, 1998; Schoser *et al.*, 2002; Catani *et al.*, 2006; Chaudhuri *et al.*, 2006] who identified background gas collisions as a cause for this flux decrease. The red data points in Fig. 3.5 (a) reveal that the use of the pusher beam improves the flux by a factor of 12 ± 2 ($\equiv$ ratio of both measurements). The influence of the pushing beam is further elucidated in the main graph of Fig. 3.5 (b) which shows the ratio between a MOT loading curve using the pushing beam (black data points in the inset) and a MOT loading curve without the pushing beam (red data points in the inset). The pushing beam is identified to cause a performance increase by more than one order of magnitude for loading times shorter than 0.1 s and to be less efficient for longer loading times. For this reason, we typically load the MOT only for 0.2 s within which we trap $\approx 3 \times 10^8$ atoms under optimum conditions.

3.4 Optimized three beam optical dipole trap

Once the atoms are trapped in the magneto-optical trap, they are transferred into an optical dipole trap, which is superimposed with the MOT beams as illustrated in Fig. 3.6 (a). The optical dipole trap is designed as a horizontally oriented three beam trap, whose geometry is optimized for large trapping volumes and tight confinement [Faber, 2011]. To fulfill these seemingly incompatible requirements, we decouple the loading from the evaporation process [Weber *et al.*, 2002; Clément *et al.*, 2009; Jacob *et al.*, 2011]. We use a large crossed reservoir trap with optimized beam waists to directly load pre-cooled atoms from the MOT and an independently controlled, tightly focused dimple trap to ensure high collision rates for efficient evaporative cooling. The dipole trap is generated from a 1 W single frequency solid-state laser[vii] at 1064 nm (spectral linewidth (over 100 ms) $\simeq$ 1 kHz), which is amplified to 50 W by a fiber amplifier[viii], preserving the spectral properties. Note that we do not apply active intensity stabilization of the dipole trap laser system.

The cigar-shaped reservoir trap is realized by imaging the Bragg diffraction pattern of an acousto-optic modulator (AOM) onto the atoms (see Fig. 3.6 (b)), using an optimized $4f$ imaging system. The imaging lenses were chosen such that the path length is shorter than $4f$, still guaranteeing a true (amplitude and phase) image of the object plane [Faber, 2011]. With this imaging trick we obtain two horizontally polarized Gaussian laser beams of 120 μm waist, which are crossed under an angle of 5.4°, and frequency shifted by the AOM frequency ν_{AOM} (typically 80 MHz)

[vii] InnoLight; Mephisto 1000

[viii] Nufern; NuAMP single frequency monolithic PM fiber amplifier NUA-1064-PD-0050-A0

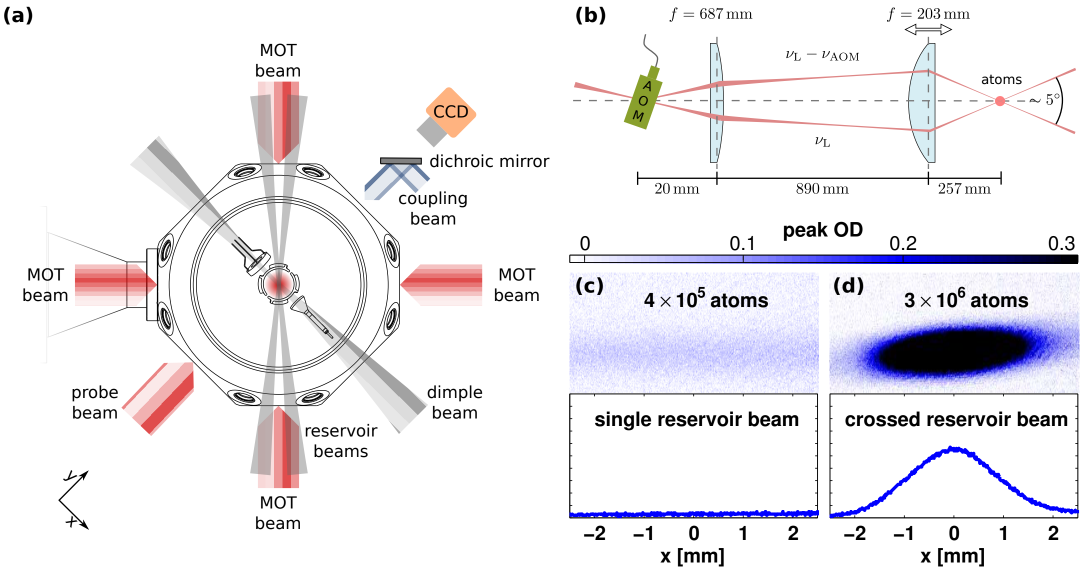

Figure 3.6: Optimized three beam optical dipole trap. (a) Top view on science chamber illustrating the beam geometry. 3 mutually orthogonal pairs of counter propagating beams ($\lambda = 780\,\mathrm{nm}$) are used for the magento-optical trap (MOT). 2 reservoir beams and a dimple beam realize the dipole trap ($\lambda = 1064\,\mathrm{nm}$). Probe ($\lambda = 780\,\mathrm{nm}$) and coupling ($\lambda = 480\,\mathrm{nm}$) laser are aligned perpendicular to the dimple beam. Thanks to a dichroic mirror, the probe light can be detected on a CCD camera. For clarity optical elements are not shown. (b) Schematic of the reservoir trap. An adjustable (double arrow) imaging system with a ≈ 0.3 magnification is used to image the diffraction pattern of an acousto-optic modulator (AOM) onto the atom cloud. (c) & (d) show absorption images of a single beam (AOM off) and crossed (AOM on) reservoir trap, respectively after $2\,\mathrm{ms}$ of free expansion. The according integrated density distributions are shown below. Using the same allover laser beam power ($21.5\,\mathrm{W}$) in both scenarios the crossed beam trap confines almost one order of magnitude more atoms.

to prevent laser beam interference. The usage of the AOM does not only simplify the crossing alignment but also allows for dynamical power balancing of the two intersecting reservoir arms. Most importantly the crossed geometry leads to a significant enhancement of confinement along the symmetry axis of the reservoir. A dramatic consequence of this is illustrated in Fig. 3.6 (c) & (d), where we compare the performance of a single beam reservoir to a crossed beam reservoir, which are both operated with the *same* total laser power of $\approx 21.5\,\mathrm{W}$. We observe an atom number increase and an accordingly higher density increase of almost one order of magnitude from 4×10^5 to 3×10^6 (a detailed description of the loading of the dipole trap will be given in Sec. 3.5.1). This approach seems to be more efficient than the confinement improvement with a weak hybrid trap [Zaiser *et al.*, 2011]. For a typical laser power of 10.7 W in each reservoir beam we obtain a maximum reservoir depth of $U_{0,\mathrm{res}} \approx k_B \times 145\,\mu\mathrm{K}$.

A third independently controlled, vertically polarized laser beam with a waist of $23\,\mu\mathrm{m}$ is used as a 'dimple' beam which crosses the reservoir axis under an angle of 45°, thereby creating an anisotropic ellipsoidal trapping potential. With a typical laser power of 2 W, we create an additional potential depth of $U_{0,\mathrm{dimple}} \approx k_B \times 350\,\mu\mathrm{K}$, such that a major fraction of the atoms in the reservoir is transferred into the dimple trap. An important feature of the combined trap is that the confinement along the weak axis of the dimple is strongly increased by the presence of the reservoir throughout the evaporation process.

3.5 Preparation of dense ultracold gases

Dense atomic or even quantum degenerate gases in flexible geometries have become a key ingredient in Rydberg physics as they not only provide a tuning knob for inter-atomic interactions but also procure large optical densities which in turn are important for nonlinear optics using cold Rydberg gases [Pritchard *et al.*, 2012]. Our solution to these requirements is described in this section which gives details about the evaporative cooling (Sec. 3.5.1), the rapid production of Bose-Einstein condensates (Sec. 3.5.2) and about the precise atomic density tuning over almost four orders of magnitude (Sec. 3.5.3).

3.5.1 Characterization of the evaporative cooling ramp

Our experimental loading cycle is summarized in Fig. 3.7. It is optimized to maximize the atom number in the reservoir trap and typically begins with a 200 ms

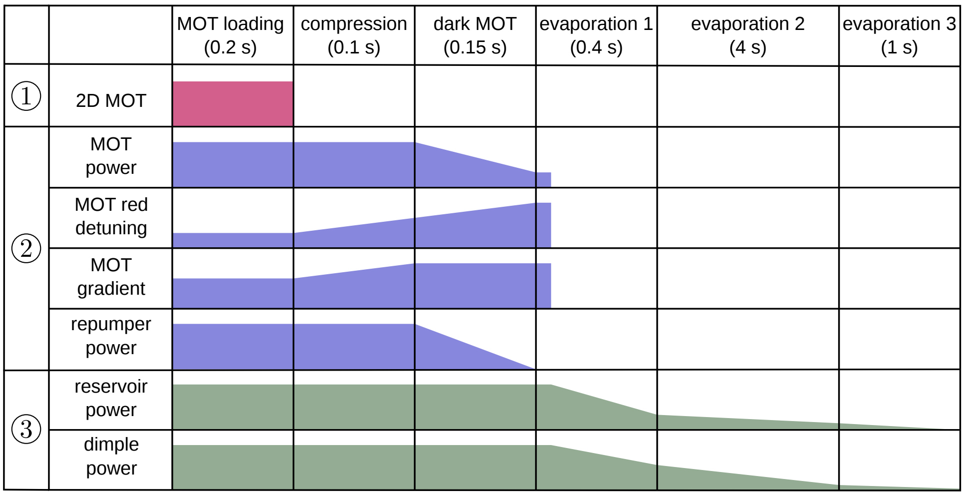

Figure 3.7: Typical experimental cycle for the preparation of dense ultracold gases. Three tools are needed for realizing dense samples in fast duty cycles: ① a high flux atoms source (2D-MOT), ② a magneto-optical trap (MOT) and ③ an optical dipole trap. The cycle begins with 2D-MOT operation. The MOT is used to create pre-cooled samples within three cooling phases. Colder temperatures and denser samples are obtained by evaporative cooling in the dipole trap, done in three optimized stages.

MOT loading phase. Thanks to the high flux 2D-MOT we trap 3×10^8 atoms in the magneto-optical trap, while the three beam optical dipole trap is already switched on. The optimized MOT parameters are 125 mW total cooling power, a red detuning of 19 MHz ($\approx 3\,\Gamma_e$), and a magnetic field gradient of 10.5 G/cm. The 2D-MOT is then switched off and the MOT is slightly compressed within 200 ms by a rise of the magnetic field gradient to 14 G/cm and an increased red detuning of 25 MHz ($\approx 4\,\Gamma_e$). To further boost the density of the atomic cloud and hence to optimize the loading of the optical dipole trap [Kuppens *et al.*, 2000], we use a 150 ms temporal dark MOT phase at constant magnetic field gradient [Townsend *et al.*, 1996]. During this phase, the detuning of the MOT cooling light is changed to -48 MHz ($\approx 8\,\Gamma_e$) and the total cooling power is weakened to 11 mW. In the same time the power of the repumping laser is reduced from 140 μW to 1 μW, yielding a sizable population of the lower hyperfine ground state $|5S_{1/2}, F = 1\rangle$. To minimize atom loss due to hyperfine changing collisions in the dipole trap, we finally pump all atoms into the $|5S_{1/2}, F = 1\rangle$ manifold by turning off the repumping laser 2 ms before the end of the dark MOT phase. At this point, about 5×10^6 atoms have been transferred into the reservoir trap at a temperature of approximately 50 μK. This is an ideal starting point for evaporative cooling [Ketterle and van Druten, 1996].

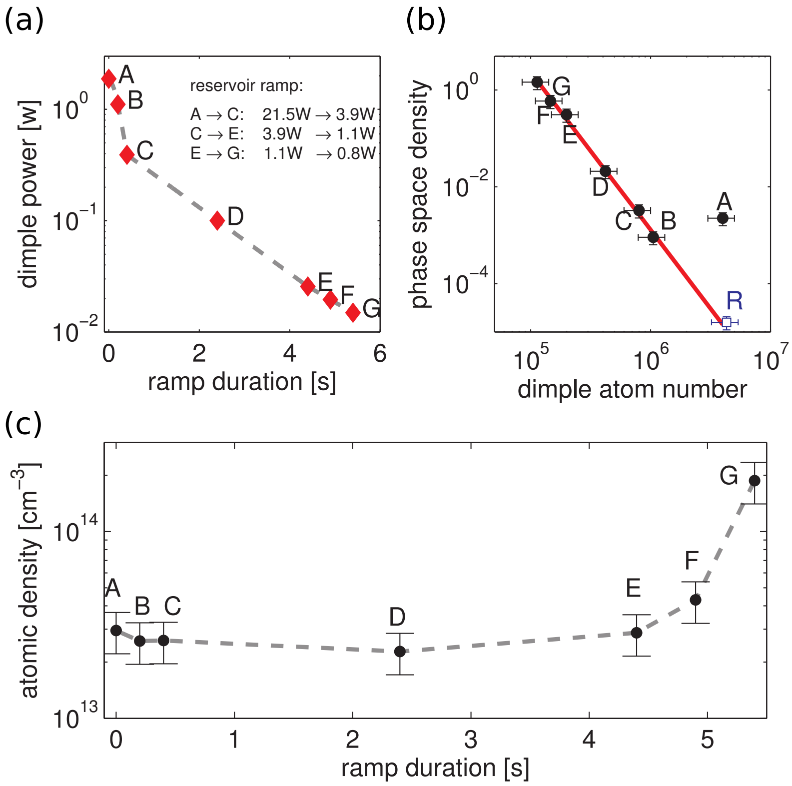

Figure 3.8: Optimized evaporative cooling ramp. (a) Adiabatic lowering of the dimple trap power. The evaporative cooling ramp is characterized at the points 'A-G'. The inset shows the according reservoir ramp. (b) Inferred phase space density ϱ_0 versus dimple atom number. The solid line is a power law fit to point 'B-G' amounting to a cooling efficiency of $\gamma_{evap} = 3.3 \pm 0.3$. The open square corresponds to the exclusive use of the reservoir trap. (c) Shows the evolution of the atomic density (in situ) in the combined trap during the evaporation ramp. The dashed lines serve as guide to the eye.

After 40 ms of free evaporation we start a forced evaporation phase by adiabatically lowering the depth of the reservoir and the dimple trap. As the rethermalization time slows down during the forced evaporation due to the reduction of the collision rate, it is favorable to lower the trap depth at decreasing pace dU_0/dt to keep the evaporation efficiency constant [O'Hara *et al.*, 2001]. We achieve this with a sequence of three exponential ramps (see Fig. 3.8: A → C, C → E, E → G) with durations of 0.4 s, 4 s, and 1 s respectively. Their time constants have been optimized experimentally for the highest gain in phase space density ϱ_0 [Faber, 2011]. We obtain optimum results for a dimple power reduction by two orders of magnitude, while the reservoir power is only reduced by a factor of ≈ 25. The presence of a strong reservoir beam is necessary to provide a high confinement along the weak axis of the dimple throughout the evaporation process.

To characterize the evaporation ramp we first investigate the temperature drop as a function of the number of atoms which remain in the dimple trap. We find that the temperature drops by a factor of ≈ 100 while the atom loss only amounts to one order of magnitude. The temperature reduction is for our experiment characterized by $\dot{T}/T = (2.3 \pm 0.3)\,\dot{N}/N$. We assume a harmonic potential to calculate the atomic density

$$n_0 = N\overline{\omega}^3 (m\lambda_{\mathrm{dB}}/h)^3\,, \tag{3.1}$$

where $\overline{\omega}$ is the geometrical mean of the calculated trapping frequencies. With the temperature T and particle number N at hand it is possible to deduce the phase space density

$$\varrho_0 = n_0 \lambda_{\mathrm{dB}}^3 \propto N T^{-3}\,. \tag{3.2}$$

Here λ_{dB} is the thermal deBroglie wavelength. The black squares (A-G) in Fig. 3.8 (b) show ϱ_0 as a function of N. As compared to the exclusive use of the reservoir (blue square (R)), we win approximately two orders of magnitude in phase space density when confining the atoms in the combined trap [ix]. For later evaporation times (B-G), we observe an increase in phase space density with decreasing atom number at a constant cooling efficiency

$$\gamma_{evap} = -\frac{\mathrm{Ln}[\varrho_0/\varrho_0']}{\mathrm{Ln}[\mathrm{N}/\mathrm{N}']} = 3.3 \pm 0.3\,, \tag{3.3}$$

as extracted from the solid line in Fig. 3.8 (b). This is in good agreement with similar systems: $\gamma_{evap} = 3.5$ [Lauber *et al.*, 2011], $\gamma_{evap} = 2.8 \pm 0.5$ [Clément *et al.*, 2009]. We furthermore obtain a truncation parameter of $\mathcal{T} = U_0/k_B T = 5.8$ during most of the evaporation, which is a typical value for the evaporation in an optical dipole trap. The critical phase space density is reached with $\approx 1 \times 10^5$ atoms in the dipole trap. Thus the ratio of the atom number at the start of evaporation to the atom number at the BEC transition $N(t=0)/N_c \approx 40$, which is in good agreement with [Lauber *et al.*, 2011]. Figure 3.8 (c) shows the evolution of the atomic density (in situ) during the evaporation ramp. The combined trap allows us to maintain a high density throughout the evaporation, since the confinement along the symmetry axis of the trap is almost kept constant. After trap release, the density can be continuously decreased by changing the time-of-flight of the gas, as will be discussed in Sec. 3.5.3.

[ix] The reservoir phase space density was calculated using a total reservoir laser power of 21.5 W.

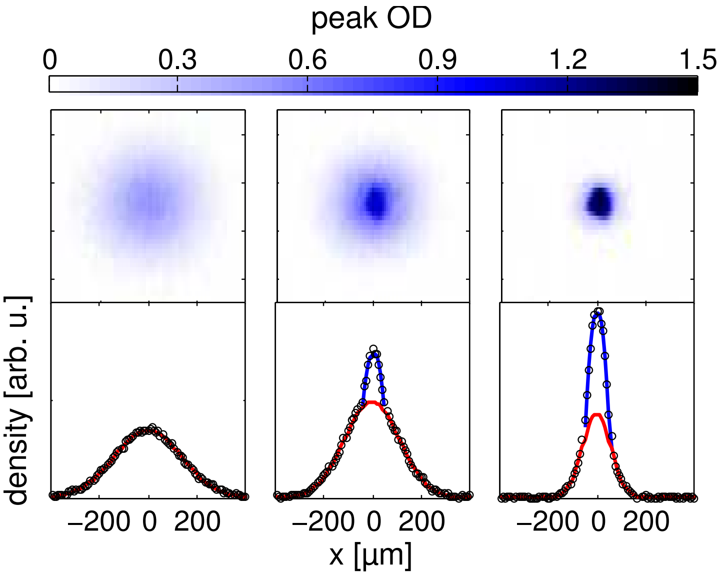

Figure 3.9: Bose-Einstein condensation transition. Upper row: Absorption images of a thermal gas and two partially condensed gases, taken during the evaporation ramp after a time-of-flight of 22 ms. Lower row: Corresponding integrated atomic density distributions (points). The second and third profile clearly show a bimodal structure evidencing the onset of Bose-Einstein condensation. The red lines represent Gaussian fits to the thermal fraction of the gas, whereas the blue lines are integrated Thomas Fermi profiles quantifying the condensed fraction.

3.5.2 Bose-Einstein condensation

To achieve Bose-Einstein condensation, the dimple trap depth is decreased further. At a trap depth of approximately 700 nK, the critical temperature $T_c = 260\,\mathrm{nK}$ is reached and the gas undergoes the transition to a Bose-Einstein condensate [Anderson *et al.*, 1995; Davis *et al.*, 1995]. This transition is shown in Fig. 3.9 which depicts absorption images of three different atom clouds, that have been released at different stages of the evaporation phase and expanded for a time-of-flight of 22 ms. The first column shows a thermal gas while the second column indicates the onset of condensation evidenced by the bimodal density distribution [Castin and Dum, 1996]. The trap typically holds $\approx 1 \times 10^5$ atoms at this point. Further evaporation leads to an almost pure condensate with $\approx 2 \times 10^4$ atoms (see third column in Fig. 3.9). Our condensates are spinor condensates with relative abundance of 0.5, 0.3, and 0.2 in the $|m_F = -1\rangle$, $|m_F = 0\rangle$, and $|m_F = +1\rangle$ magnetic states of the $\big|5S_{1/2}, F = 1\big\rangle$ manifold, respectively, which could be purified with a spin distillation technique to obtain a BEC in a single $|m_F\rangle$ state [Couvert *et al.*, 2008]. The best number achieved was $\approx 2 \times 10^5$ atoms at the transition point and $\approx 6 \times 10^4$ atoms in a nearly pure condensate. Our shortest *total* cycle time which still produced a BEC with $\approx 8 \times 10^3$ atoms was around 4.5 s. As the spatial extent of these BECs is smaller than typical blockade radii (*e.g.* $R_{\mathrm{bl}}(|55S\rangle) \approx 5\,\mu$m) it should be possible to realize fully blocked samples that only allow for the accommodation of a single Rydberg excitation.

3.5.3 Precise atomic density tuning

Another aspect in the preparation of ultracold atom samples for Rydberg physics is the accurate tuning of atomic density. For different temperatures and atom numbers this can be done through ballistic expansion, which is one of the most important means to control the interaction strength between subsequently excited Rydberg atoms (compare Fig. 2.2). As exemplified here, this technique permits to bridge almost four orders of magnitude in density as illustrated in Fig. 3.10 (a), which shows data extracted from 91 absorption images of cold atom clouds, that have been recorded after different expansion times ranging from 0.01 to 4.51 ms. In this case the sample was always prepared at a temperature of $T = 6.2\,\mu$K and consisted of $\approx 2.5 \times 10^4$ atoms. The data is compared to a ballistic expansion model which nicely reproduces the extracted densities at long time-of-flights, but significantly deviates for times shorter than 1 ms. The discrepancy results from the finite resolution of the imaging system ($\approx 12\,\mu$m Rayleigh criterion), which overestimates the cloud dimensions shortly after trap release. We estimate the in situ $1/e^2$ radii of the ellipsoidal cloud to be $r_{\mathrm{axial}} \approx 56\,\mu$m and $r_{\mathrm{radial}} \approx 2\,\mu$m which — for Rydberg excitations after short expansion times — gives rise to quasi-one-dimensional Rydberg gases since the radial cloud dimension r_{radial} is smaller than typical blockade radii $R_{\mathrm{bl}}(|55S\rangle) \approx 5\,\mu$m. The cloud dimensions change according to the data shown in the inset of Fig. 3.10 (b) and correspond to a three-dimensional gas for long time-of-flights.

The cloud expansion also affects the atom number inside the excitation volume, which is defined by the intersection of the two excitation lasers that illuminate the cloud along its radial direction. Figure 3.10 (b) illustrates the according atom number decrease from 20×10^3 to 2×10^3 for an elliptical excitation beam with dimensions $\approx 50 \times 100\,\mu$m (both FWHM). The underestimation of the atom number for time-of-flights < 1 ms once again results from the finite resolution of the imaging system. The experimental settings and the cloud characterization detailed here are an important component of the experiments described in Ch. 6.

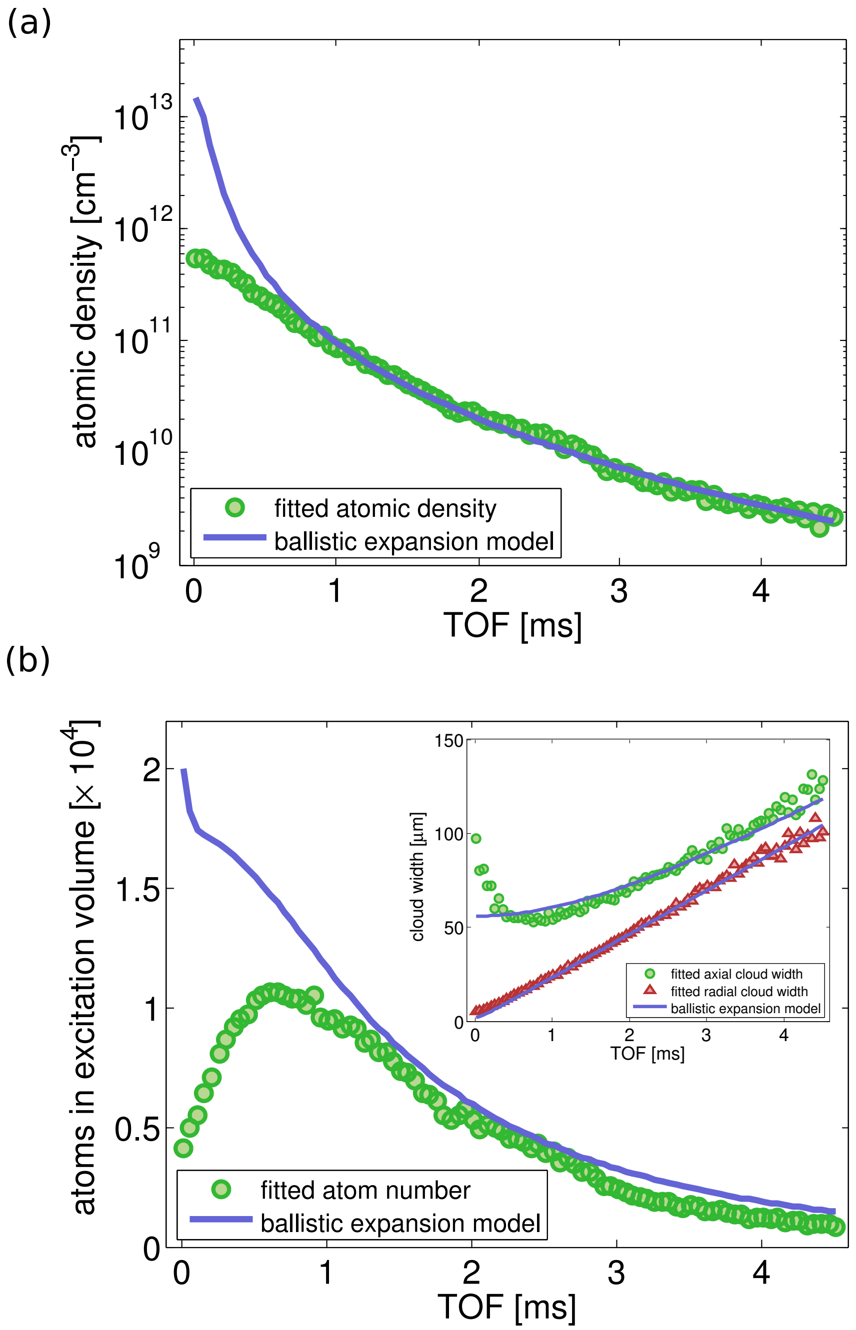

Figure 3.10: Atom cloud parameters as a function of expansion time. (a) Atomic density evolution of a $6.2\,\mu\mathrm{K}$ atom cloud. The data are extracted from 91 absorption images taken at different time-of-flights (TOF). (b) The main graph illustrates the atom number inside the Rydberg excitation volume, characterized by an elliptic excitation beam cross-section ($\approx 50 \times 100\,\mu\mathrm{m}^2$) and the radial cloud length. The inset shows the according cloud dimensions. The solid lines are solutions to a ballistic expansion model accounting for the in situ $1/e^2$ cloud radii $r_{\mathrm{axial}} \approx 56\,\mu\mathrm{m}$ and $r_{\mathrm{radial}} \approx 2\,\mu\mathrm{m}$.

Control of density changes can also be accomplished by optical pumping, whereby the density of atoms in the $|5S, F=2, m_F=2\rangle \equiv |g\rangle$ is accurately prepared. In this case, the time-of-flight can be kept constant in order to maintain the size of excitation volume. This approach was used to alter the Rydberg interaction in the experiments described in Ch. 5.

3.6 Electric field control

At the center of the science chamber is a specially designed stainless steel electrode assembly shown in Fig. 3.11, which was manufactured in the mechanical workshop of our institute. The electrode structure was partly conceived in the framework of a Masters-Thesis and is described in detail in [Müller, 2010]. It is laid out not to affect the optical access and allows for the realization of versatile electric field configurations.

(*i*) It is for example possible to carry out three dimensional stray field compensation with an anticipated background field of $\lesssim 5\,\mathrm{mV/cm}$ as simulated by [Müller, 2010]. This electric field stability is precise enough to hold Stark shifts of Rydberg states with principal quantum numbers up to $\mathsf{n}^\star \approx 120$ below 1 MHz as the required stability typically scales with $0.01(100/\mathsf{n}^\star)^{7/2}$ V/cm [Saffman *et al.*, 2010].

(*ii*) Another aspect is the application of precisely controlled homogeneous fields or gradient fields [Müller, 2010].

(*iii*) Of equal importance is the application of large electric fields (up to $\gtrsim 1.2\,\mathrm{kV/cm}$) that are used to field ionize the Rydberg atoms for charged particle detection as detailed in the next section.

(*iv*) Finally it can realize electric field ramps for state-selective detection [Walz-Flannigan *et al.*, 2004; Westermann *et al.*, 2006; Reinhard *et al.*, 2008a].

The electrode structure is attached to the science chamber with a DN160CF to DN63CF reducing flange with 18 SHV connections (⑧) as shown in Fig. 3.11 (b). An electrically grounded supporting structure (①) holds in total ten individually addressable electrodes in place, which are used to control the electric field landscape at the position of the atoms. The electrodes are divided into two deflection half rings (②) and eight field plates as illustrated in Fig. 3.11 (a). The field plates are situated at the extremes of a virtual cylindrical volume of height 44 mm and diameter 34 mm

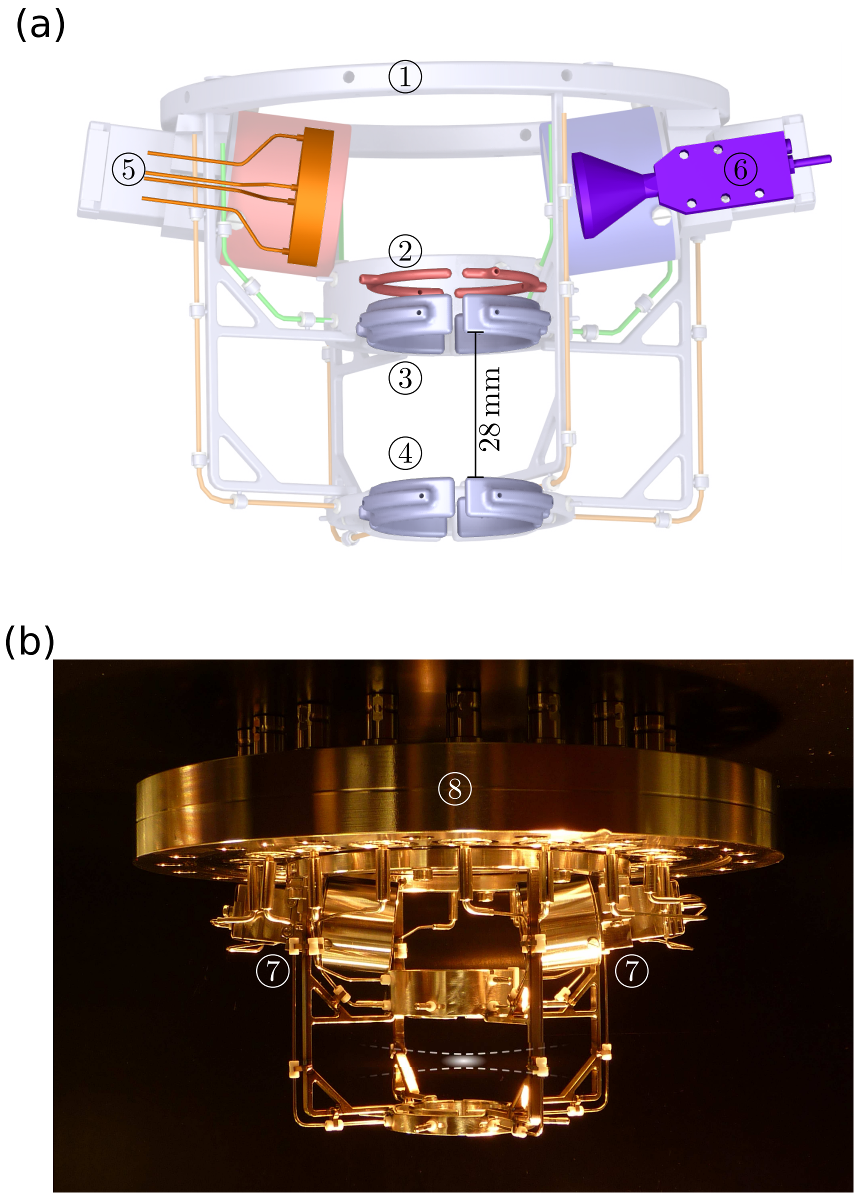

Figure 3.11: Electrode assembly for electric field control and for field ionization of Rydberg atoms. (a) Schematic drawing of the electrode assembly. A grounded supporting structure ① holds two deflection rings ② as well as four upper ③ and four lower ④ field plates in place, that are used to control the electric field landscape at the position of the atoms. Charged particle detection is possible with either a micro-channel plate (MCP) ⑤ or a channel electron multiplier (CEM) ⑥ detector. (b) Photograph of the stainless steel structure which also shows the Faraday cages ⑦ that surround the detectors and the vacuum flange ⑧ with 18 high voltage connections. The position of the atom cloud and the orientation of the dipole trap are sketched on the photograph.

and are arranged such that four field plates are situated 'above' (③) and 'beneath' (④) the Rydberg gas, respectively. Each field plate resembles a quarter cylinder segment with an inner radius of 15 mm, a height of 8 mm and a wall thickness of 2 mm. The shape and separation of the field plates were optimized with extensive SIMION-simulations to achieve the best electric field homogeneities at the position of the gas. The simulated field deviations are $< 5‰$ in a volume of $1\,\mathrm{mm}^3$ [Müller, 2010].

We use bipolar high voltage switches (Behlke) with an effective rise time of $\approx 300\,\mathrm{ns}$ to dynamically control the electric fields and to perform field ionization of Rydberg atoms. Half-ring-shaped deflection electrodes (②) are used to guide the produced ions on a curved trajectory into either a micro-channel plate (MCP; ⑤) detector or a channel electron multiplier (CEM; ⑥) as shown in Fig. 3.11 (a). The CEM and the Chevron-MCP both have a circular detection area of $180\,\mathrm{mm}^2$. The two detectors are mirror-symmetrically installed above the upper field plates to maintain optical access in the horizontal plane of the experiment. To minimize the stray fields caused by their $\approx 2\,\mathrm{kV}$ bias voltages, both detectors are mounted inside Faraday cages (see ⑦ in photograph in Fig. 3.11 (b)). As the detector has no direct line of sight to the trapping region, we obtain absolutely background-free detection signals.

3.7 Rydberg atom detection

The most frequently used Rydberg atom detection technique is field ionization in combination with charged particle detection by micro channel plates. Being by its nature globally invasive, the technique usually reveals insight to averaged ensemble properties. It thereby requires involved extensions to infer spatial information from the sample [van Ditzhuijzen *et al.*, 2006]. Spatial correlations in dilute Rydberg gases could only recently be studied with a combination of field ion microscopy method and a MCP-based imaging detector [Schwarzkopf *et al.*, 2011].

An alternative approach is optical detection which progressed recently. A destructive technique was pursued by Schauß *et al.*, who used a down-stimulation of Rydberg atoms to ground state atoms which, could subsequently be detected using fluorescence imaging, giving direct access to spatial excitation patterns of up to five Rydberg atoms [Schauß *et al.*, 2012]. Non-destructive optical probing of Rydberg states was pioneered by C.S. Adams and coworkers, detecting Rydberg EIT with conventional photodiodes [Mohapatra *et al.*, 2007; Pritchard *et al.*, 2010] and was lately extended to spatially resolved detection with CCD cameras [Tauschinsky *et al.*, 2010; Hattermann *et al.*, 2012; Hofmann *et al.*, 2012]. We recently proposed a novel all-optical and non-destructive imaging method, which can be readily implemented in current experiments and is aimed to resolve individual Rydberg atoms [Günter *et al.*, 2012].

In this section we focus on the combination of both field ionization assisted Rydberg detection as well as spatially resolved optical probing using Rydberg state electromagnetically induced transparency.

3.7.1 Field ionization and few ion counting

Rydberg atoms can be detected by applying large state-dependent ionization fields, ranging from $\mathcal{E}^{(\infty)} \approx 700\,\mathrm{V/cm}$ for $\mathsf{n} = 30$ to $\mathcal{E}^{(\infty)} \approx 6\,\mathrm{V/cm}$ for $\mathsf{n} = 100$, that convert Rydberg atoms to ions. The ions are afterwards detected on a micro-channel plate detector (MCP) giving rise to time-resolved ion traces which are recorded on a fast oscilloscope with a time resolution of 0.1 ns. The observed pulse height distribution typically spans between 0.03V and approximately 0.6V.

Dependent on the density of ion events, we apply two different analysis methods to extract the Rydberg population. For large ion numbers typically exceeding ≈ 20 ions it is not possible to resolve single ions, therefore the ion traces are integrated. On the contrary, in the few ion regime in which we clearly distinguish discrete voltage pulses from a background noise level, ion counting becomes feasible since the probability of two overlapping events is negligible ($< 1\%$), as shown in Fig. 3.12. To count individual ions, we employ a sparse spike deconvolution of the signal which is based on an orthogonal matching pursuit (OMP) algorithm [Rebollo-Neira and Lowe, 2002]. The basic idea of this algorithm is to represent each ion trace $\mathcal{I}(t)$ as a weighted sum $\mathcal{I}(t) = \sum_{i=0} c_i a_i(t)$ of functions $a_i(t)$ that belong to an over-complete dictionary. Here t is the arrival time, i indexes the dictionary elements $a_i(t)$ that have been chosen to match the signal, and c_i are their weighting factors. For a given dictionary, the algorithm first searches for the $a_i(t)$ that has the largest inner product with $\mathcal{I}(t)$ (i.e. the locally optimal choice), and then computes the residual of the chosen dictionary element and the signal. This is repeated until the residual falls below the detection threshold τ ($0.02\,V$ for the presented data), resulting in a satisfactory signal decomposition. To define a dictionary element $a_i(t)$ we fit a generalized peak function to 250 isolated single ion events, each of them being the most prominent peak of an ion trace. The median of each of the fit parameters is then used as an input parameter for the generalized peak function thus describing the

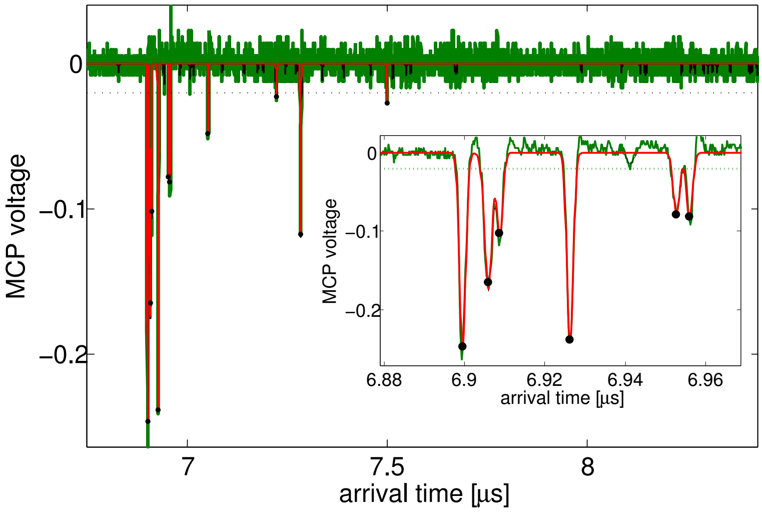

Figure 3.12: Ion detection signal demonstrating single ion sensitivity. The main figure depicts an ion trace (green). The red line shows a sparse spike deconvolution of the signal, which is used to model the data. To count the number of detected ions, the derivative of the smoothed signal is taken and the number of sign changes are counted (from negative to positive), if the according peak position falls below the -0.02 V detection threshold (dotted line). The inset shows a detail of this ion trace. Black points indicate peak positions of identified ion events.

ideal single ion event $a_i(t)$. In particular we obtain a pulse width of 1.1 ns (FWHM). The dictionary elements are equitemporally spaced by 0.2 ns which is comparable to the oscilloscope resolution and the dead time of a single MCP channel. As illustrated by the inset of Fig. 3.12, the OMP algorithm is used to smooth the ion traces in order to suppress fluctuations which occur on timescales faster than our MCP temporal resolution. We then take the derivative of the decomposed signal and count the number of sign changes (from negative derivatives to positive derivatives), which in turn corresponds to the number of detected ions. From the ion-pulse-height-distribution of the resultant ion trace, we infer a counting efficiency of 0.9, which combined with the MCP detection efficiency (≈ 0.6), angular responsivity (≈ 0.9) and guiding efficiency (≈ 0.6) gives an estimate of the overall efficiency of $\mathcal{D} \approx 0.4$.

3.7.2 Combined ion and optical detection of Rydberg atoms

The previously introduced Rydberg detection technique is now extended to optical probing of Rydberg states using Rydberg state electromagnetically induced transparency (see Sec. 2.3.2) which is demonstrated with the *combined* application of these techniques. In the experiments detailed here, we chose the three-level ladder system depicted in Fig.3.13 (a), with: $|g\rangle \equiv \left|5S_{1/2}, F=2\right\rangle$, $|e\rangle \equiv \left|5P_{3/2}, F=3\right\rangle$, and $|r\rangle \equiv \left|40S_{1/2}\right\rangle$. For simplicity we restrict ourselves to a regime of experimental parameters in which Rydberg–Rydberg interaction effects on the EIT [Pritchard *et al.*, 2010; Schempp *et al.*, 2010; Sevinçli *et al.*, 2011a] can be neglected. This is ensured by the preparation of dilute clouds with atomic peak densities of $n_0 = 2.2\times10^9\,\mathrm{cm}^{-3}$, containing $N \approx 2.4\times10^5$ atoms which are distributed over an elliptical volume characterized by $r_{\mathrm{radial}} = 75\pm3\,\mu$m and $r_{\mathrm{axial}} = 280\pm10\,\mu$m. The Rydberg state is reached via resonant two photon excitation, in which the 480 nm coupling laser (see Fig. 3.13 (a)) is frequency stabilized using frequency modulation spectroscopy involving Rydberg EIT in a room temperature vapor cell [Abel *et al.*, 2009; Müller, 2010]. The weak 780 nm probe laser covering the first excitation step homogeneously illuminates the atom cloud, while the counter propagating coupling beam is focused onto a small circular region (diameter $\approx 50\,\mu m$) defining the excitation volume. Both lasers have opposite circular polarization such that a three level scheme can be prepared by optical pumping in a magnetic bias field. The probe light is collected on a CCD camera for optical detection (see Fig. 3.1) during the 100 μs excitation time. The imaging system has a 3.6-fold magnification and an optical resolution of $\approx 12\ \mu m$ (Rayleigh criterion).

The mapping of the Rydberg state properties onto the light field can directly be seen on the recorded absorption images: on the two photon resonance we observe a local transparency due to the presence of the coupling beam (see Fig. 3.13 (b)). To quantify the transparency in the excitation volume, we postprocess all absorption images using a fringe-removal algorithm to reduce the imaging noise [Ockeloen *et al.*, 2010] and fit a double peak function $\mathcal{G}(x,y) = \mathcal{G}_{\mathrm{cloud}}(x,y) - \mathcal{G}_{\mathrm{EIT}}(x,y)$ to each post-processed image. The profile of the atom cloud is described by a Gaussian $\mathcal{G}_{\mathrm{cloud}}(x,y)$ and its extrapolation allows us to infer the local optical density at the position of the excitation volume. A second Gaussian fit $\mathcal{G}_{\mathrm{EIT}}(x,y)$, defined to be centered around $(0,0)$, analyses the reduction of the optical density due to the presence of the coupling laser. In particular we conclude from Fig. 3.13 (b) that the coupling beam causes a $\approx 75\%$ reduction of the two level absorption in the excitation volume.

Before we turn off the excitation lasers, we ramp up the electric fields to $\mathcal{E} \approx 250\,\mathrm{V/cm}$ within 300 ns, which serves two purposes: On the one hand side it freezes the Rydberg excitation dynamics and on the other hand it field ionizes Rydberg atoms, resulting in a destructive measurement of the dark-state population [Schempp *et al.*, 2010]. The ionization fields have been tailored such that the produced ions are guided towards the MCP detector. A corresponding ion trace is shown in Fig. 3.13 (c)

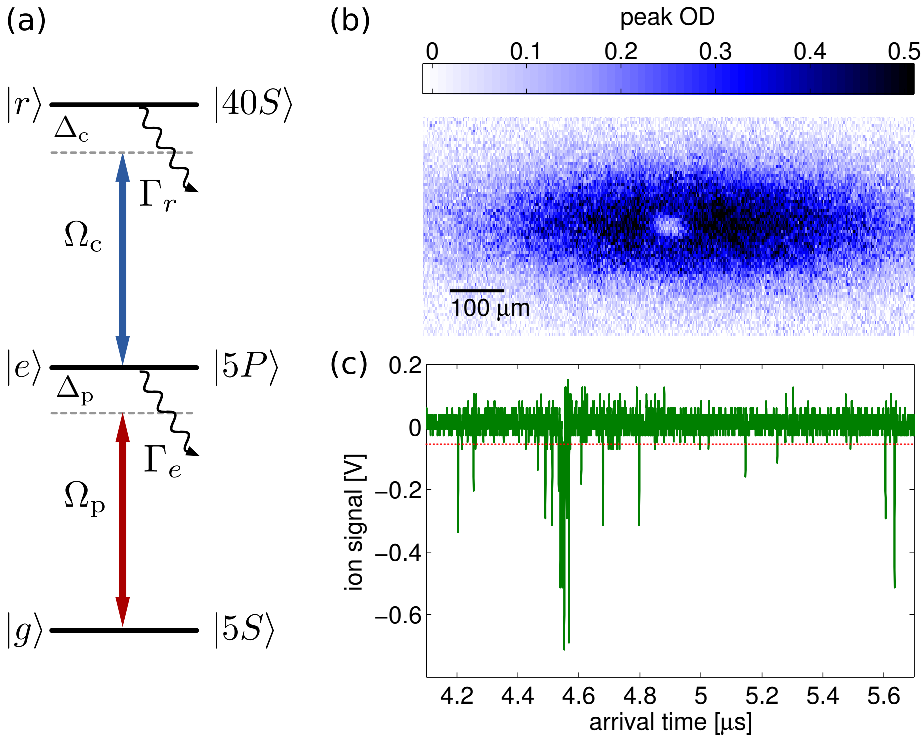

Figure 3.13: Rydberg EIT as a tool for combined Rydberg state detection by optical imaging and field ionization. (a) Energy level diagram with Ω_p (Ω_c) the Rabi frequency and Δ_p (Δ_c) the laser detuning of the 780 nm probe (480 nm coupling) laser. Γ_e and Γ_r are spontaneous decay rates of the intermediate state $|e\rangle$ and the Rydberg state $|r\rangle$, respectively. (b) Absorption image of the atomic cloud after a free expansion of $600\,\mu$s. The presence of the resonant coupling beam induces a transparency of $\approx 75\%$ in the center of the excitation volume. (c) Ion detector signal of the field ionized Rydberg ensemble recorded during the *same* experimental run.

and reveals that most of the ions arrive in a bunch after a time-of-flight of $\approx 4.5\,\mu$s. In the measurements presented here we typically collect more than ≈ 50 ions which give rise to overlapping ion pulses, such that we relate the Rydberg population to the integrated MCP signal.

To study the interplay of the two detection techniques we investigate Rydberg EIT by probing the spectral response of the EIT medium. This is done by scanning the frequency of the weak 780 nm probe laser. By locally analyzing the absorption images from a single frequency scan we simultaneously obtain the two spectra shown in Fig. 3.14 (a). The red data points are deduced from $\mathcal{G}_{\text{cloud}}(0,0)$ and correspond to the two level response of the atoms. The EIT window, illustrated by the blue data

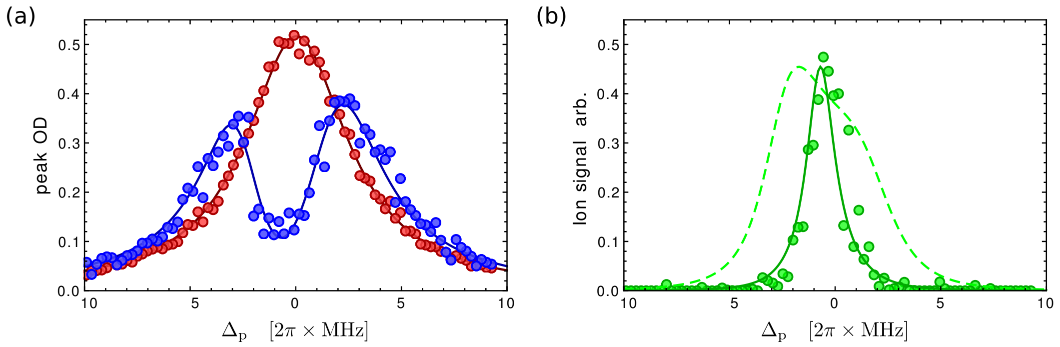

Figure 3.14: Combined optical and ion detection. (a) The two level response (red) and the EIT spectrum (blue) agree well with a fit to the imaginary part of the optical susceptibility (solid lines), revealing a local coupling Rabi frequency $\Omega_c/2\pi = (4.8 \pm 0.2)\,\mathrm{MHz}$. (b) Field ionization spectrum (green) measured in the *same* scan. The dashed line is a numerical solution to the optical Bloch equation using Ω_c, which fails to describe the data. Since field ionization is a macroscopic ensemble averaged measurement, the effective Rabi frequency, averaged over the coupling beam profile has to be used to reproduce the measurement (solid line).

points is inferred from $\mathcal{G}_{\mathrm{cloud}}(0,0) - \mathcal{G}_{\mathrm{EIT}}(0,0)$. The spectral probe laser response of the medium is given by the imaginary part of the optical susceptibility χ. In the weak probe limit (i.e. $\Omega_p < \Omega_c \,\&\, \Gamma_e$) this is given by the analytic expression [Günter *et al.*, 2012]

$$\chi = a \frac{i\Gamma_e}{\frac{\Omega_c^2}{\Gamma_r - 2i\Delta} + \Gamma_e - 2i\Delta_p} \,. \tag{3.4}$$

Here, a is the peak optical density and Γ_r is the combination of the spontaneous decay rate of the Rydberg state and a laser-induced dephasing rate. $\Delta = \Delta_p + \Delta_c$ is the two photon detuning. As discussed in Sec. 2.3.2, for $\Omega_c = \Gamma_r = 0$, i.e. no coupling to the Rydberg state, the imaginary part of the optical susceptibility encapsulates the Lorentzian response of the two level system, which agrees well with the red data points in Fig. 3.14 (a). From the fit we obtain a spontaneous decay of the intermediate state of $\Gamma_e/2\pi = 5.9 \pm 0.1\,\mathrm{MHz}$ which is in agreement with the natural linewidth of the $|5P_{3/2}\rangle$ state of ^{87}Rb. Using this and the fitted Δ_p as input parameters we fit the full expression of the imaginary part of the optical susceptibility to the EIT spectrum shown in Fig. 3.14 (a). This way we obtain for the two local peak Rabi frequencies $\Omega_c/2\pi = 4.8 \pm 0.2\,\mathrm{MHz}$ and $\Omega_p/2\pi = 2.2 \pm 0.3\,\mathrm{MHz}$, and the decay rate of the Rydberg state $\Gamma_r/2\pi = 0.9 \pm 0.2\,\mathrm{MHz}$.

The field ionization spectrum recorded during the *same* scan (Fig. 3.14 (b)) provides direct access to the Rydberg population. The dashed line shows a numerical solution to the optical Bloch equation using the parameters determined above as input parameters. We note that the predicted resonance feature is significantly broader ($\approx 5.5\,\mathrm{MHz}$) than the measured spectrum, which only has a width of $\approx 1.7\,\mathrm{MHz}$. The discrepancy lies in the nature of the two detection techniques and can be understood by bearing in mind that the field ionization is a macroscopic, integrated measurement, whereas the optical technique gives access to microscopic properties of the system due to its spatial resolution. In particular a *local* Rabi frequency Ω_c was used to reproduce the optical spectra shown in Fig. 3.14 (a), which results in the prediction of a power-broadened field ionization resonance and is hence inappropriate to explain the macroscopic measurement shown in Fig. 3.14 (b). Instead it is necessary to account for the spatially varying intensity distribution of the focused blue coupling beam which redounds to a spatially dependent steady state Rydberg population. Spatially averaging over the Gaussian coupling beam profile finally gives perfect agreement with the field ionization spectrum.

3.7.3 Spatially resolved optical Rydberg state probing

The previous section revealed that Rydberg EIT in combination with absorption imaging offers an ideal tool to optically investigate microscopic properties of the Rydberg gas. This is possible by analyzing the images not only in the very center of excitation volume but throughout the coupling beam profile using ≈ 1000 camera pixels. Since the coupling laser intensity and the atomic density are spatially dependent, this constitutes effectively ≈ 1000 parallel measurements. This is demonstrated in Fig. 3.15 showing the spatially resolved analysis of a probe frequency scan, which was acquired in the noninteracting regime involving $|55S\rangle$ Rydberg states. Clouds of typically 1.7×10^5 atoms have been released from the dipole trap to expand to almost spherically symmetric clouds ($r_\mathrm{radial} = 106 \pm 8\,\mu\mathrm{m}$, $r_\mathrm{axial} = 145 \pm 13\,\mu\mathrm{m}$) with atomic peak densities of $n_0 = (5.0 \pm 0.1) \times 10^9\,\mathrm{cm}^{-3}$. These cloud dimensions ensure that the atomic density and the probe Rabi frequency are approximately constant within the excitation volume, such that the intensity of the focused coupling beam is the only spatially varying quantity giving rise to a spatially dependent spectral EIT response. For each camera pixel i it is thus possible to extract a local coupling Rabi frequency $\Omega_\mathrm{c}^{(i)}$ which is in turn related to the local coupling beam intensity by $I^{(i)} \propto \left(\Omega_\mathrm{c}^{(i)}\right)^2$. Such a spatially resolved EIT analysis is illustrated in Fig. 3.15 (a) showing 500 EIT spectra, recorded in parallel which have been extracted from 81 absorption images acquired during a probe laser frequency scan covering a range of

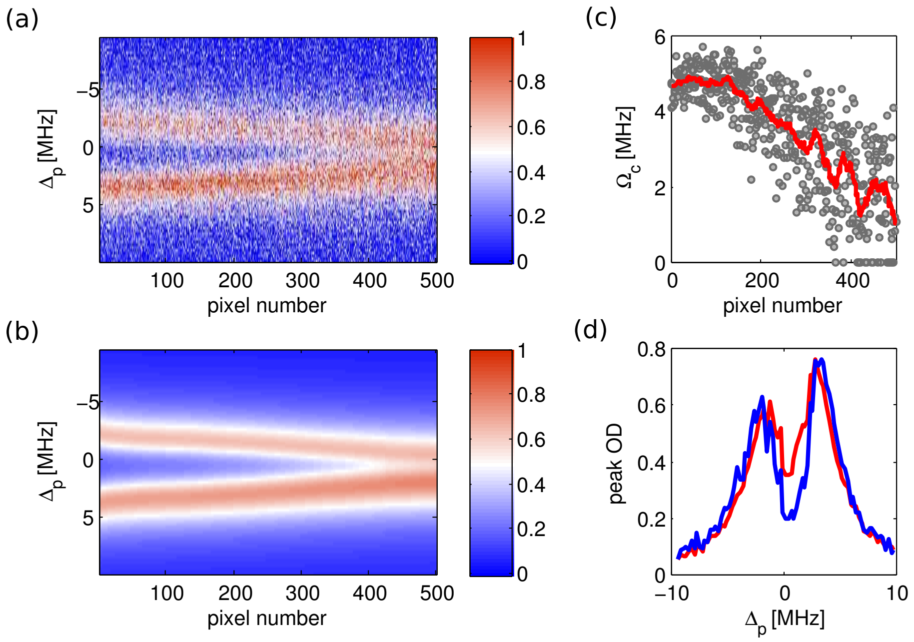

Figure 3.15: Spatially resolved optical Rydberg state probing. (a) 500 simultaneously recorded $|55S\rangle$ Rydberg EIT spectra extracted from 500 camera pixels inside the transparency region. The colorbar represents the peak optical density (OD). The according fitted optical response with global input parameters $\Gamma_\mathrm{p}/2\pi = 5.6\,\mathrm{MHz}$, $\Gamma_\mathrm{c}/2\pi = 1.6\,\mathrm{MHz}$ and $\Delta_\mathrm{c}/2\pi = -0.7\,\mathrm{MHz}$, but free $\Omega_\mathrm{c}^{(i)}$ is depicted in (b), whereas (c) shows the fitted $\Omega_\mathrm{c}^{(i)}$ for each pixel. The red line is a moving average over the gray data points with a window size of 20 pixels. (d) The blue (red) curve shows an averaged EIT spectrum generated from the first 100 (500) pixels in (a).

$\Delta_\mathrm{p}/2\pi = \pm 10\,\mathrm{MHz}$. All pixels have been sorted according to their distance to the center of the transparency region. The measurements nicely agree with a fit using the imaginary part of Eq. (3.4), as demonstrated in Fig. 3.15 (b). To extract $\Omega_\mathrm{c}^{(i)}$, we used the following separately determined global input parameters $\Gamma_\mathrm{p}/2\pi = 5.6\,\mathrm{MHz}$, $\Gamma_\mathrm{c}/2\pi = 1.6\,\mathrm{MHz}$ and $\Delta_\mathrm{c}/2\pi = -0.7\,\mathrm{MHz}$. Figure 3.15 (c) shows the local coupling Rabi frequency is versus pixel indices, where higher pixel indices correspond to spatial regions further away from the coupling beam center. We find that $\Omega_\mathrm{c}^{(i)}$ decreases for increasing pixel numbers, which is expected as the laser beam intensity decreases radially. Figure 3.15 (c) also reveals the existence of a region corresponding to $\gtrsim 100$ pixels in which the determined local coupling Rabi frequencies are almost constant with an averaged Rabi frequency of $\tilde{\Omega}_\mathrm{c}^{(i)} = 4.3 \pm 0.5\,\mathrm{MHz}$. An EIT spectrum averaged over the respective first 100 spectra is shown in Fig. 3.15 (d) as blue line. Averaging over the first 500 spectra, thereby including the inhomogeneity of Rabi frequencies,

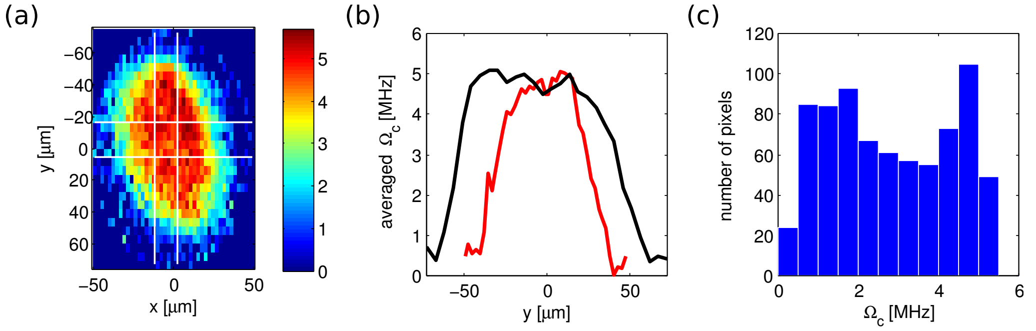

Figure 3.16: Reconstructed coupling beam profile. (a) The 'landscape' of local Rabi frequencies $\Omega_c^{(i)}$ is reconstructed from ≈ 1000 camera pixels and is proportional to the square root of the coupling beam intensity distribution. The white lines enclose regions of interest, used to generate the beam cross-sections shown in (b). The vertical cross-section (black line) is averaged over 6 columns of pixels, while the horizontal cross-section (red line) is averaged over 4 rows of pixels. A histogram of the local Rabi frequencies $\Omega_c^{(i)}$ is shown in (c).

significantly decreases the contrast of the EIT window, as demonstrated by the red solid curve in Fig. 3.15 (d).

To minimize this inhomogeneity problem, we employed a diffractive optical element (DOE), which is designed to convert a Gaussian beam profile into a flat-top beam profile, as described in detail in [Reetz-Lamour *et al.*, 2008]. To quantify the DOE performance, we assigned each local Rabi frequency to the corresponding pixel position. This way it is possible to generate a coupling Rabi frequency landscape, which is proportional to the square root of the coupling beam intensity profile. An example — extracted from the above mentioned measurements — is shown in Fig. 3.16 (a), which reveals an elliptical beam profile whose averaged cross-sections in horizontal and vertical direction suggest an almost top-hat-shaped Rabi frequency distribution with horizontal and vertical diameters (FWHM) of $\approx 60\,\mu$m and $\approx 100\,\mu$m, respectively (Fig. 3.16 (b)). Such reconstructed beam profiles were used to optimize the position of the DOE to ensure maximum homogeneity of the coupling beam. This is favorable since the local steady state Rydberg population ($\propto \Omega_p^2/(\Omega_c^{(i)})^2$) as well as the excitation dynamics vary significantly throughout the excitation volume as a consequence of the spatially changing coupling beam profile. A histogram of the local Rabi frequencies of the reconstructed beam profile is depicted in Fig. 3.16 (c), which shows a local minimum at intermediate $\Omega_c^{(i)}$ and a second maximum at larger $\Omega_c^{(i)}$, as expected for an almost top-hat-shaped beam profile.

Chapter 4

Evidence of antiblockade in an ultracold Rydberg gas

This chapter is based on the following publication[i]:

Evidence of Antiblockade in an Ultracold Rydberg Gas
T. Amthor, C. Giese, C. S. Hofmann, M. Weidemüller
Physical Review Letters **104**, 013001 (2010)

The excitation blockade is one of the most striking effects originating from strong Rydberg–Rydberg interactions in *resonantly* driven systems. Early experiments investigated the bulk properties of Rydberg blockaded gases revealing substantial Rydberg excitation suppression [Tong *et al.*, 2004; Singer *et al.*, 2004; Vogt *et al.*, 2006; Vogt *et al.*, 2007], collective excitation effects [Heidemann *et al.*, 2007], or sub-Poissonian counting statistics [Reinhard *et al.*, 2008b; Viteau *et al.*, 2012]. Only recently a microscopic analysis of Rydberg interacting gases has become possible, unveiling the strongly correlated many-body states emerging when atoms are transferred to Rydberg states [Schwarzkopf *et al.*, 2011; Schauß *et al.*, 2012]. Using an all-optical imaging technique Schauß *et al.* directly accessed the spatial excitation patterns of up to five Rydberg atoms which are observed to arrange in well defined geometries but random orientations [Schauß *et al.*, 2012]. A theoretical study recently predicted the dynamical formation of floating Rydberg excitation crystals also for *off-resonant* laser driving, allowing an adjustment of the lattice constants

---

[i] In contrast to all other experimental results presented in this thesis, the experiments described in this chapter were obtained with our former experimental apparatus and were still performed at Freiburg University.

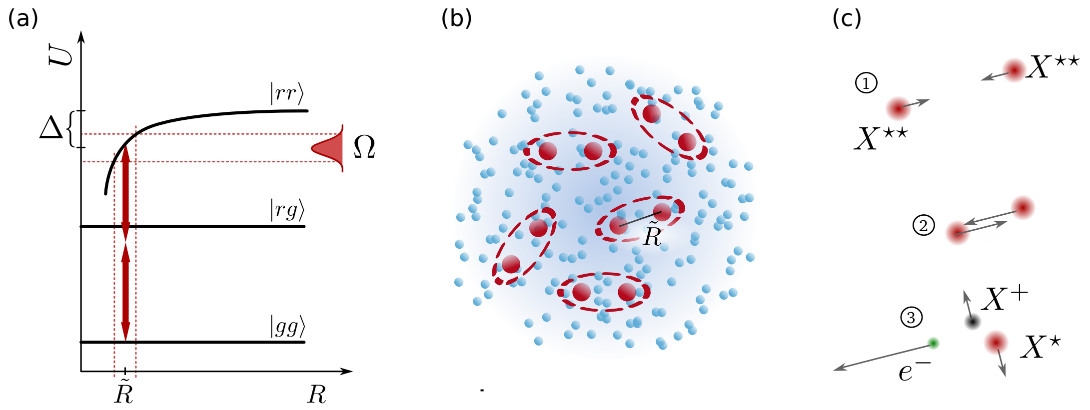

Figure 4.1: Rydberg pair selection in an ultracold gas by detuned laser excitation. (a) The energy level diagram of attractively interacting Rydberg pairs $|rr\rangle$ illustrates that a red detuned ($\Delta < 0$) excitation is exclusive to Rydberg atom pairs with a specific pair distance, approximately given by the radius $\tilde{R}$. (b) This creates structure within an initially unordered gas. Note that this method is also applicable to repulsively interacting Rydberg states for blue detuned excitation. (c) Illustration of the Penning ionization mechanism. Two attractively interacting Rydberg atoms ($X^{\star\star}$) separated by $\tilde{R}$, are accelerated towards each other ①&②. Collisional ionization produces one ion (X^+) and one electron (e^-) and de-excites the other Rydberg atom ($X^\star$) ③. This way the pair separation is translated into an ionization time.

through the laser detuning [Gärttner *et al.*, 2012]. A similar mechanism is illustrated in Fig. 4.1 (a) which shows that negative detunings Δ can partially compensate the attractive interaction, such that certain Rydberg pair separations $\tilde{R}$ are preferred. Making use of detuned excitation, one is thus able to directly manipulate the Rydberg pair distribution and in particular to excite Rydberg atom pairs separated by less than the blockade radius. Appropriately this concept is called 'antiblockade' which has recently been proposed by Ates *et al.* [Ates *et al.*, 2007a].

The antiblockade can be realized via a three-level two-photon Rydberg excitation scheme where the van der Waals interaction energy at a given atomic distance corresponds to the Autler-Townes splitting induced by the lower transition. By exploiting the blockade and antiblockade in a controlled way, spatial correlations can be imposed on the excited atoms in an otherwise randomly arranged ultracold gas. Specific pair distances can thus be preferred or suppressed, which is of particular interest not only for quantum information [Saffman *et al.*, 2010], but for a variety of applications involving controlled interactions, such as resonant energy transfer [Anderson *et al.*, 1998; Mourachko *et al.*, 1998; Westermann *et al.*, 2006; van Ditzhuijzen *et al.*, 2008], or the creation of long-range molecules [Boisseau *et al.*, 2002; Overstreet *et al.*, 2009]. Other experiments used small optical dipole traps to fix the distance between Rydberg atoms [Urban *et al.*, 2009; Gaëtan *et al.*, 2009], but this technique does not allow to prepare a large number of pairs at a specific range of distances simultaneously.

In the characterization of the antiblockade phenomenon Ates *et al.* considered a lattice with fixed lattice constant, while tuning the interaction strength between the Rydberg atoms by changing the principal quantum number n [Ates *et al.*, 2007a]. An increased two-photon Rydberg excitation probability in a three-level scheme was predicted when the interaction energy and the coupling Rabi frequency Ω_c match. In our experimental demonstration of this effect, a complementary approach is followed. Starting from an *unstructured* gas, we show that atomic pairs can be resonantly excited even at inter-atomic separations where the atomic interaction shift is much greater than the excitation linewidth. While keeping the quantum number fixed, the interaction strength is instead matched by picking specific atom pairs with appropriate inter-atomic distances (see Fig. 4.1 (b)). Our method of measuring this pair distribution modification due to the antiblockade is illustrated in Fig. 4.1 (c) and is based on the dynamics of atomic pairs under the influence of the forces exerted by the interactions, as explored in [Amthor *et al.*, 2007b]: Once a pair of Rydberg atoms is excited on an attractive van der Waals potential, the atoms will be accelerated towards each other and collide after a time $t_\mathrm{coll} \propto \sqrt{m_{Rb}/C_6}R^4$, depending on their initial distance R and the interaction strength C_6 [Gallagher and Pritchard, 1989; Amthor, 2008]. These collisions can lead to Penning ionization as explained in Sec. 2.2.2. In particular, the collision times of close pairs are shorter resulting in Penning ionization at shorter times. By measuring the number of ions produced after a variable time Δt we are able to identify even slight modifications in the nearest-neighbor distance distribution without performing a spatially resolved measurement.

4.1 Detuned laser excitation of interacting Rydberg atoms

We describe the system in terms of an interacting two-atom system with the three atomic levels $|g\rangle$, $|e\rangle$, $|r\rangle$, corresponding to the $|5S\rangle$ ground state, the $|5P\rangle$ intermediate state, and the $|62D\rangle$ Rydberg state of ^{87}Rb, respectively. The calculations are based on the two-atom Hamiltonian $\mathcal{H} = \mathcal{H}_\mathrm{al} + \mathcal{H}_\mathrm{int}$, where $\mathcal{H}_\mathrm{al}$ represents the couplings within the three-level systems and $\mathcal{H}_{\text{int}} = U_{\text{int}}(R) \left|rr\right\rangle \left\langle rr\right|$ is the van der Waals interaction between two Rydberg states with $U_{\text{int}}(R) = -C_6^{\text{eff}}/R^6$ (see Sec. 2.3.3). The interaction of atoms with non-vanishing angular momentum leads to a large number of interaction potentials due to the many possible symmetries. We introduce an effective van der Waals interaction coefficient C_6^{eff} to reduce the calculation to a three-level system [Amthor *et al.*, 2007b]. We solve the Master equation for the density matrix, $\dot{\rho} = -\frac{i}{\hbar}[\mathcal{H}, \rho] + \mathcal{L}(\rho) + \mathcal{L}_{\text{d}}(\rho)$, where $\mathcal{L}(\rho)$ contains the decay of the intermediate state $\Gamma_e \approx 2\pi \times 6\,\text{MHz}$ and $\mathcal{L}_{\text{d}}(\rho)$ contains the two laser linewidths ($\approx 2\pi \times 1\,\text{MHz}$) as additional dephasing terms, as explained in Sec. 2.3.1. The spontaneous and blackbody-induced decay of the Rydberg level as well as blackbody photoionization can be neglected here because the timescale of observation is well below the timescale of these processes for the Rydberg state chosen in the experiment [Beterov *et al.*, 2009a; Beterov *et al.*, 2009b].

In the following — as an exception in this thesis — we make use of an inverted system, with the strong coupling Ω_{c} being realized on the lower transition $\left|g\right\rangle \rightarrow \left|e\right\rangle$ as shown in the energy level diagram in Fig. 4.2 (a). We introduce the detuning from the Rydberg state Δ_{p} and the Rabi frequency Ω_{p} for the upper transition with $\Omega_{\text{c}} \gg \Omega_{\text{p}}, \Gamma_e$. The dressed eigenenergies of two interacting three-level systems are given explicitly in Fig. 4.2 (a) for the limiting case of $|\Delta_{\text{p}}| \gg \Omega_{\text{c}}$, and are plotted in Figs. 4.2 (b)-(d) (upper graphs) as a function the probe laser detuning Δ_{p} for three different interaction energies U_{int}. Lines with slope -1 correspond to levels containing one Rydberg excitation, while lines with slope -2 (highlighted in red) are primarily of $\left|rr\right\rangle$ character. At the avoided crossings the Rydberg states are populated, resulting in the Autler-Townes doublet introduced in Sec. 2.3.2.

Calculated Rydberg excitation spectra for pairs at three different separations, i.e. for three different interaction energies, are depicted in Figs. 4.2 (b)-(d) (lower graphs). Without interaction (atoms far apart), a symmetric Autler-Townes spectrum is visible (Fig. 4.2 (b)) and the population of $\left|rr\right\rangle$ (red dotted line) is equal on both peaks. An interaction energy of $U_{\text{int}} = \Omega_{\text{c}}/2$ (Fig. 4.2 (c)) causes a considerable blockade of excitation, with the population of the Rydberg pair state $\left|rr\right\rangle$ being completely suppressed at the two resonances, but slightly enhanced on the red wing of each excitation line. In the corresponding energy diagram, the state having predominantly $\left|rr\right\rangle$ character is shifted. If U_{int} is further increased to match the lower Rabi frequency Ω_{c} (Fig. 4.2 (d)), the doubly excited state $\left|rr\right\rangle$ is again populated at $\Delta_{\text{p}} = -\Omega_{\text{c}}/2$, but is still completely suppressed at $\Delta_{\text{p}} = +\Omega_{\text{c}}/2$. As can be seen in the energy diagram, the state experiencing the interaction shift now crosses zero at $\Delta_{\text{p}} = -\Omega_{\text{c}}/2$, while there is no possible coupling any more for $\Delta_{\text{p}} > 0$. A

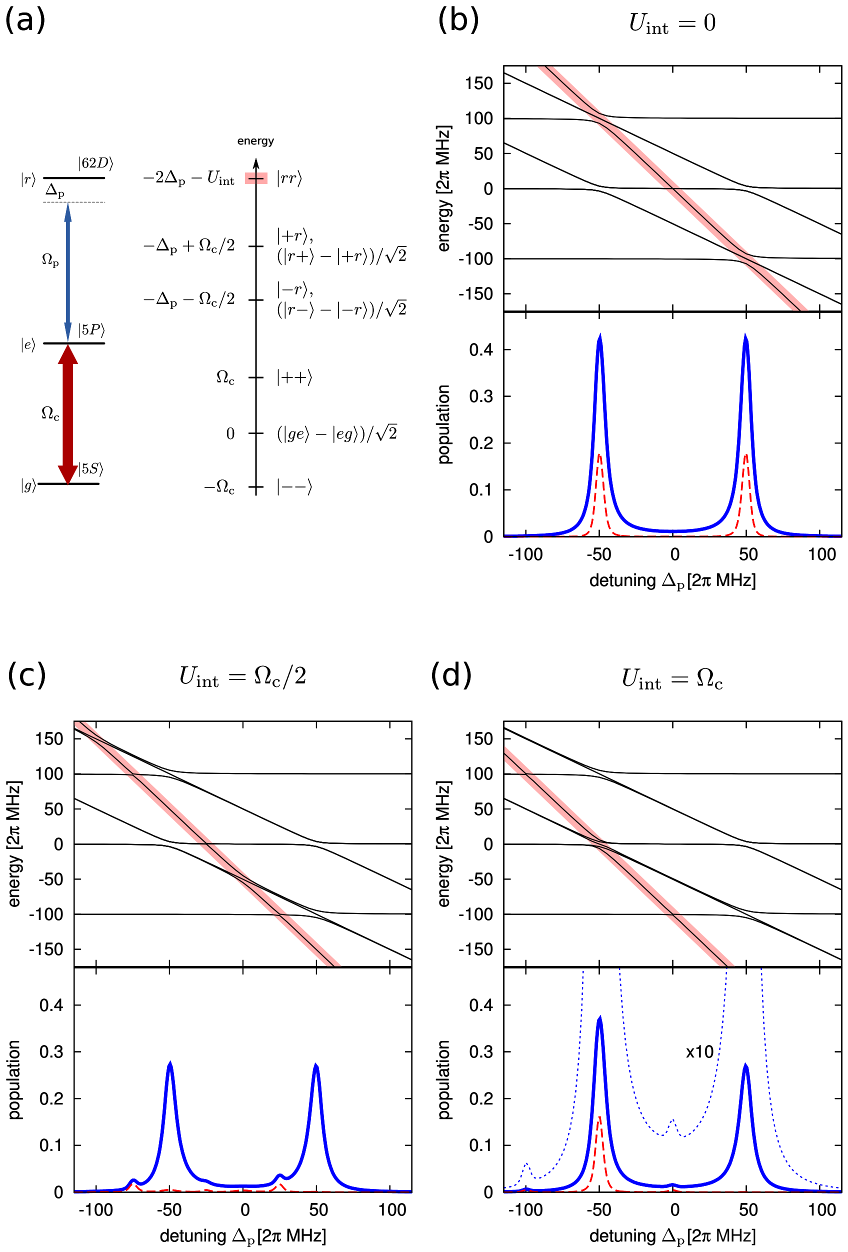

Figure 4.2: Eigenenergies and calculated Rydberg excitation spectra. (a) Energy level diagram and dressed pair state energies for $|\Delta_p| \gg \Omega_c$ with $|\pm\rangle = (|e\rangle \pm |g\rangle)/\sqrt{2}$. (b) - (d) Eigenstates (upper graphs) and calculated Rydberg excitation (lower graphs) as a function of Δ_p for fixed pair distance corresponding to $U_{\mathrm{int}} = 0$, $U_{\mathrm{int}} = \Omega_c/2$, $U_{\mathrm{int}} = \Omega_c$, respectively. The Rabi frequencies are $\Omega_c = 2\pi \times 100\,\mathrm{MHz}$ and $\Omega_p = 2\pi \times 10\,\mathrm{MHz}$. For $|\Delta_p| \gg \Omega_c$ the states approach the ones shown in (a). The states having predominantly $|rr\rangle$ character are highlighted in red. In the excitation spectra, the solid blue lines represent the total Rydberg population per atom, while the dashed red lines show the population of the Rydberg pair state $|rr\rangle$. The dotted line in (d) is the total population scaled by a factor of 10. Parameters and excitation laser pulse shapes used in the model calculations correspond to the experimental settings.

slight enhancement of excitation can also be observed at $\Delta_\mathrm{p} = 0$ (see dotted curve). The antiblockade discussion in [Ates *et al.*, 2007a] is restricted to this peak at zero detuning. Introducing a finite detuning of $\Delta_\mathrm{p} = -\Omega_\mathrm{c}/2$, the antiblockade effect becomes much more pronounced. In addition, it is now possible to directly compare a blockaded regime (accessed with positive detuning) with an antiblockaded regime (accessed with negative detuning) in a *single* spectrum.

In order to predict the outcome of a measurement in an unstructured cloud, one determines weighted averages of spectra at different inter-atomic spacings representing the actual distribution of nearest-neighbor distances [Hertz, 1909]. The results of such a calculation for our experimental parameters is presented in Fig. 4.4 (a) & (c). The same scaling factor is used for all graphs to match the experimental detector signal of the Rydberg excitation. The upper graphs (black) represent the total Rydberg excitation with contributions of atom pairs containing a single Rydberg excitation $|gr\rangle$, $|rg\rangle$, $|er\rangle$, $|re\rangle$, and Rydberg pairs $|rr\rangle$, averaged over all nearest-neighbor distances. The latter ones undergo Penning ionization on a microsecond timescale and are thus sensitive to the applied detection technique. That is why the lower graphs (red) show only the population of $|rr\rangle$ as an average of all pair distances at which the atoms are undergoing Penning ionization within the specified time delay Δ_t. This implicitly assumes that each collision leads to Penning ionization with unity probability. As expected from Fig. 4.2 (d), one finds a pronounced asymmetry of the two Autler-Townes components. Due to the attractive character of the interaction potential, ions appear first on the red-detuned wings of each of the $|62D_{5/2}\rangle$ lines [Amthor *et al.*, 2007b]. The collision time depends mainly on the long-range part of the attractive interaction potentials, where the atom pairs spend most of their time. This is why one does not require exact knowledge of the inner part of the potentials.

4.2 Evidence of antiblockade

In the experiment, atoms confined in a magneto-optical trap are excited to the $|62D\rangle$ state with a 50 ns pulse of the upper transition, while the lower transition laser is turned on with a fixed Rabi frequency $\Omega_\mathrm{c} \gg \Omega_\mathrm{p}$. The 780 nm coupling laser illuminates the whole trapped atom cloud, and the 480 nm probe laser is focussed to a waist of 37 μm, resulting in a peak Rabi frequency of $\Omega_\mathrm{p}^{peak} = 2\pi \times 10.6\,\mathrm{MHz}$ in the center. After a variable delay time Δt, an electric field ramp is applied to drive the ions onto a micro-channel plate detector. Ions already present due to Penning

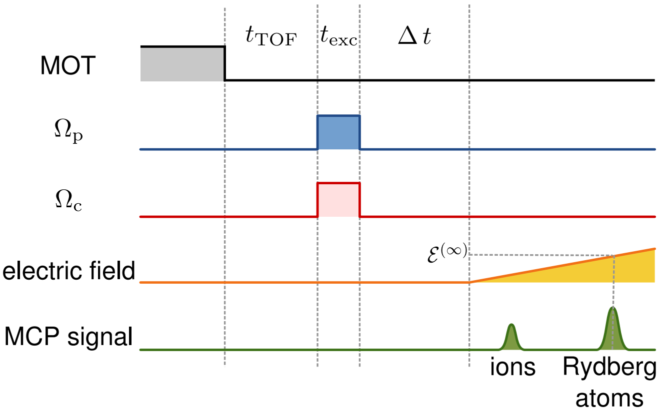

Figure 4.3: Timing of the experiment. Atoms are released from the magneto-optical trap (MOT) and excited to Rydberg states by the two excitation lasers (Ω_{c} and Ω_{p}) after a time-of-flight t_{TOF}. An electric field ramp is applied to guide the ions onto a micro-channel plate (MCP) detector. Ions already present due to Penning ionization are detected first, while the remaining Rydberg atoms are only ionized when the electric field exceeds the ionization threshold $\mathcal{E}^{(\infty)}$.

ionization are detected first, while the remaining Rydberg atoms are only ionized when the field is strong enough and can thus be distinguished in the detector signal, as illustrated in Fig. 4.3. The experimental cycle is repeated every 70 ms. Each cycle yields one data point in the measured Rydberg and ionization spectra presented in Fig. 4.4 (b) & (d). The structure of the $|62D_{3/2}\rangle$ and $|62D_{5/2}\rangle$ lines appears twice in the spectrum, separated by the coupling Rabi frequency Ω_{c}. We restrict our discussion to the spectral features of the $|62D_{5/2}\rangle$ state, as the $|62D_{3/2}\rangle$ state is barely excited. Excellent agreement between our model and the measurements is found for an effective attractive vdW interaction with $C_6^{\mathrm{eff}} = 5 \times 10^{20}$ a.u. This value is consistent with long-range potential calculations for the state $|62D_{5/2}\rangle$ which yield values of the same order of magnitude for all possible molecular symmetries [Singer *et al.*, 2005]. In accordance with theory, there is a clear asymmetry between the two Autler-Townes components. The ionization is stronger and starts earlier on the component which appears for negative detunings ($\Delta_{\mathrm{p}} < 0$), evidencing the antiblockade, which corresponds to the excitation of close — otherwise blocked — Rydberg atom pairs. Clearly, the excitation of close pair states is markedly suppressed for the peak at positive detuning corresponding to the blockaded scenario. The contribution of these Rydberg pairs $|rr\rangle$ at short distances, which are subject to early Penning ionization, is hardly discernible in the total Rydberg signal (upper graphs in Fig. 4.4 (a)-(d)), highlighting the sensitivity of the applied detection technique.

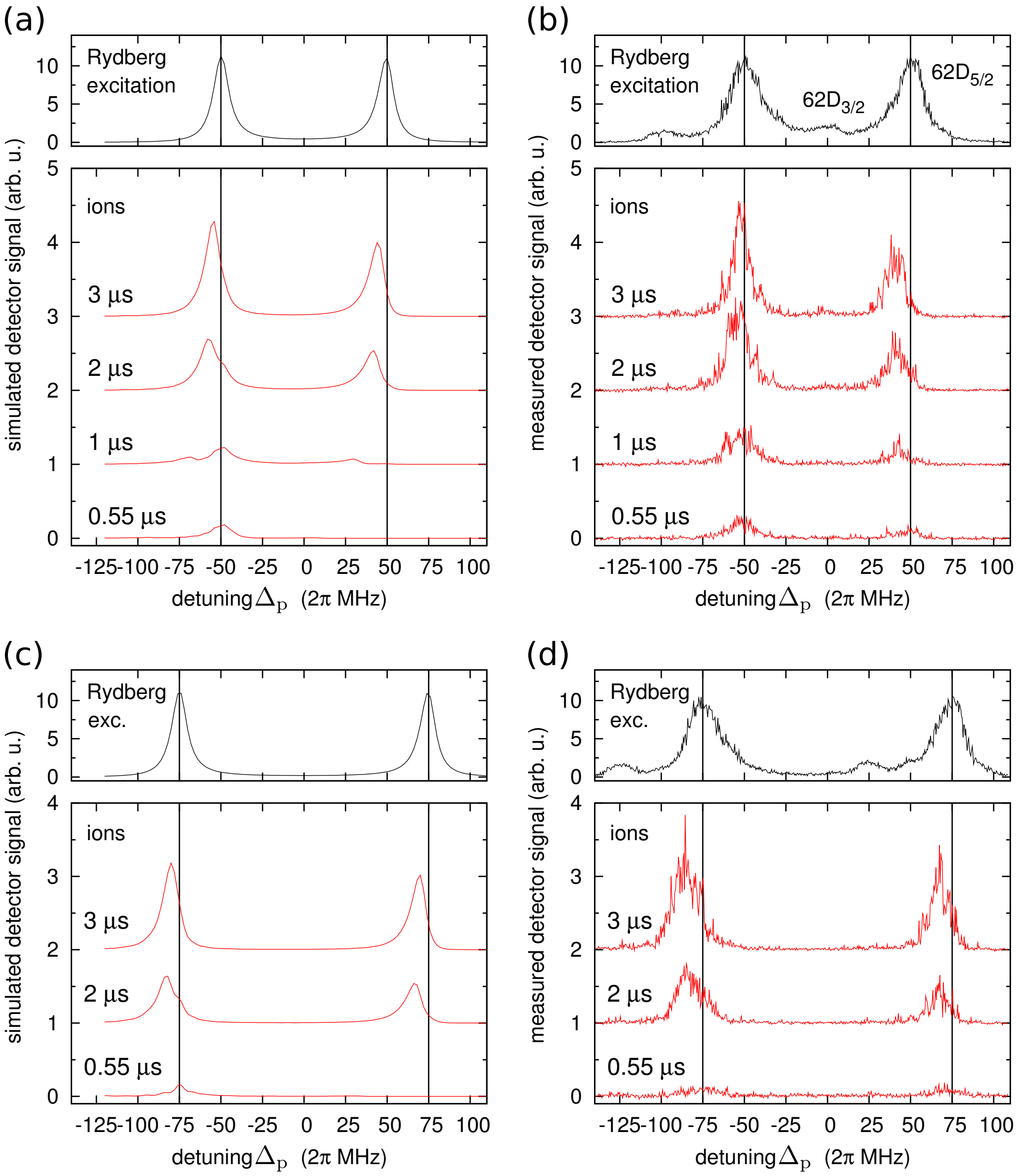

Figure 4.4: Comparison between calculated and measured $|62D\rangle$ Rydberg excitation spectra and ionization spectra. Left column: Model calculations for (a) $\Omega_c = 2\pi \times 100\,\mathrm{MHz}$, and (c) $\Omega_c = 2\pi \times 150\,\mathrm{MHz}$, and a density of the trapped ground state atoms of $n = 7 \times 10^9\,\mathrm{cm}^{-3}$. Right column: measurements for the same parameters, respectively. The upper graphs in each set (black) show the Rydberg population directly after excitation. Below (red) the ion signal at different delay times is shown, offset vertically for clarity. The respective delay Δt is indicated at each trace. In both model and measurement, ions appear earlier on the red-detuned Autler-Townes component, and the asymmetry is more pronounced for smaller Ω_c. A red-shift of the maximum ionization relative to each peak in the excitation spectrum is always clearly visible. Vertical lines have been drawn at $\pm 50\,\mathrm{MHz}$ and $\pm 75\,\mathrm{MHz}$ to emphasize this.

The distinctness of the asymmetry depends on the availability of atom pairs for which the interaction potential corresponds to Ω_c. As the ground state pair density for a separation R is proportional to R^2, more pairs are available at larger distances, which is why the asymmetry becomes more pronounced for smaller Rabi splittings Ω_c [Amthor, 2008]. We have verified this with additional measurements and calculations at $U_\mathrm{int} = 2\pi \times 150\,\mathrm{MHz}$ (see Fig. 4.4 (c) & (d)) and at $U_\mathrm{int} = 2\pi \times 62\,\mathrm{MHz}$ (not shown). In all calculations and measurements, the asymmetry of the two peak heights also consistently decreases as the ion peaks grow with time, since only a small number of close pairs is responsible for the asymmetry observed at short times Δt. As a result of these large Rabi couplings Ω_c we specifically access and probe variations of the pair distances shorter than the average atoms distance in the cloud. This allows us to describe the system in terms of nearest neighbors and to neglect many-body effects.

The underestimation of the peak widths in the simulation can be explained by the fact that we did not consider the spatial intensity profile of the upper excitation laser but instead only used the Rabi frequency present in the center of the beam to minimize calculation time. Averaging over the radial distribution of coupling Rabi frequencies has been found to account for a slight broadening of the excitation peaks [Deiglmayr *et al.*, 2006]. We observe that a small number of ions appear already at very short times ($0.55\,\mu$s), before the first collisions are predicted by our model. This instant ionization might be attributed to a sequence of near-resonant dipole–dipole transitions for which one atom is coupled to the continuum while the other atom looses energy, similar to a molecular auto-ionization process [Tanner *et al.*, 2008].

4.3 Engineering of Rydberg pair correlations

In this chapter, we have observed and modeled the effects of an antiblockade in an interacting Rydberg gas excited with a strong coupling laser at the lower transition of a three-level system. We used time-resolved ionization detection as a method to monitor the distribution of excited pair distances which allowed us to clearly observe additionally excited pairs at small distances out of a large distribution. In this way we could gain spatial information without performing a spatially resolved measurement. Making use of detuned excitation, we are able to directly manipulate the Rydberg pair distribution through long-range interactions and to compare a blocked and an anti-blocked situation in a single spectrum. The asymmetry between

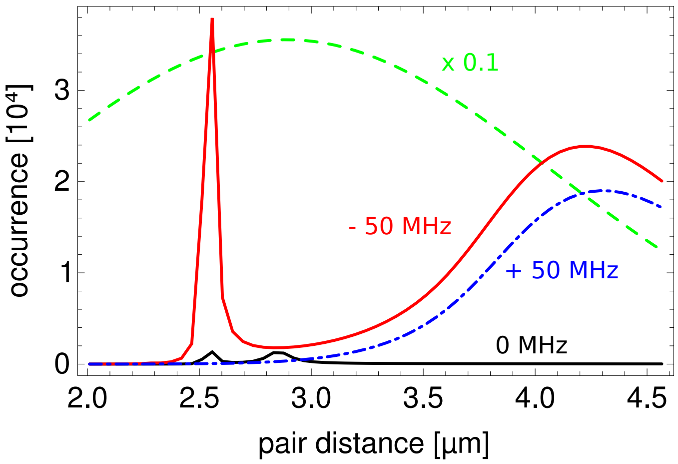

Figure 4.5: Calculated nearest-neighbor pair distribution of $|rr\rangle$ states. The following input parameters were used: $\Omega_\mathrm{c} = 2\pi \times 100\,\mathrm{MHz}$ and $\Delta_\mathrm{p} = 0$ (black, solid), $\Delta_\mathrm{p} = 2\pi \times 50\,\mathrm{MHz}$ (blue, dash-dotted), and $\Delta_\mathrm{p} = -2\pi \times 50\,\mathrm{MHz}$ (red, solid), at $\Delta t = 0$. The dashed green curve above shows the ground state nearest-neighbor distribution, scaled by a factor of 0.1 for better comparison.

the two ionization peaks is a direct probe for the strength of Rydberg interactions. To demonstrate how detuned laser excitation can be employed as a means to tailor correlations between Rydberg atoms, we calculated the difference in the distribution of pair distances at the position of the two Autler-Townes peaks $\Delta_\mathrm{p} = \pm\Omega_\mathrm{c}/2$. The green solid line in Fig. 4.5 represents the distribution of nearest-neighbor distances in the cloud. At zero detuning (solid, black line) there is also a finite excitation probability at small distances, but the excitation is still comparatively small because of the strong Autler- Townes splitting. At $\Delta_\mathrm{p} = +\Omega_\mathrm{c}/2$ (blue, dash-dotted line) the population of $|rr\rangle$ is strongly suppressed at distances below $3.5\,\mu\mathrm{m}$. At $\Delta_\mathrm{p} = -\Omega_\mathrm{c}/2$ (red, solid line) additional antiblockaded pairs at small distances ($\tilde{R} \approx 2.5\,\mu\mathrm{m}$) are present where the pair distance leads to an interaction-induced resonant excitation with $U_\mathrm{int} \approx \Omega_\mathrm{c}$. It should be noted that the antiblockade not only allows precise interaction control but also significantly enhances the interactions in a gas, as it gives rise to pair distances shorter than the blockade radius. Since our method does not require to arrange the atoms but rather creates structure within an initially unordered gas, it may be used in experiments requiring large numbers of atom pairs, e.g. as an initialization or detection step in quantum gate experiments [Saffman *et al.*, 2010].

Chapter 5

Spontaneous avalanche ionization of a strongly blockaded Rydberg gas

This chapter is based on the following manuscript:

Spontaneous avalanche ionization of a strongly blockaded Rydberg gas
M. Robert-de-Saint-Vincent, C. S. Hofmann, H. Schempp, G. Günter,
S. Whitlock, M. Weidemüller
arXiv:1209.4728 (2012); accepted for publication in Physical Review Letters

In the last chapter we studied binary collisions between Rydberg atoms which give rise to Penning ionization; revealing that Rydberg atoms are very fragile objects. In denser samples these ionizing collisions between Rydberg atoms can produce an ion cloud, which traps electrons produced during later collisions. Subsequently the trapped electrons rapidly collisionally ionize the remaining Rydberg atoms, resulting in an ensemble of unbound charged particles, referred to as ultracold plasma [Robinson *et al.*, 2000]. In fact the spontaneous evolution of an attractively interacting Rydberg gas into an ultracold plasma has been observed in several experiments [Li *et al.*, 2004; Walz-Flannigan *et al.*, 2004; Morrison *et al.*, 2008], which initiated in-depth studies on the ionization mechanisms [Amthor *et al.*, 2007b; Beterov *et al.*, 2007; Tanner *et al.*, 2008] and on the electron–ion recombination dynamics towards Rydberg states [Killian *et al.*, 2001; Robicheaux and Hanson, 2002; Gallagher *et al.*, 2003; Fletcher *et al.*, 2007; Saquet *et al.*, 2011]. Rydberg Gases thus offer an alternative approach to study ultracold plasmas, which are usually formed by photo-ionizing ultracold neutral atomic or molecular gases [Killian *et al.*, 1999]. Ultracold plasmas [Killian, 2007] offer an ideal laboratory setting to better understand exotic phases of matter such as dense astrophysical plasmas [Horn, 1991] or laser-induced plasmas [Remington *et al.*, 1999]. Experimental and theoretical progress is driven by the potential to reach the so-called strongly coupled regime [Ichimaru, 1982; Killian *et al.*, 2007], in which the Coulomb interaction energy dominates the kinetic energy of the ions, giving rise to collective effects and strong spatial correlations between particles. It is quantified by the coupling parameter [Killian *et al.*, 2007]

$$G = \frac{q^2}{4\pi\epsilon_0 a k_B T} \gg 1\,, \tag{5.1}$$

where $a = \sqrt[3]{3/(4\pi n)}$ is the Wigner-Seitz radius characterizing the separation between particles in a plasma of density n. The charge and the temperature of the plasma constituents is given by q and T, respectively. In laser-cooled gases, $G \approx 0.1 - 2$ is readily achieved, which has allowed the observation and driving of collective mechanical modes [Fletcher *et al.*, 2006; Twedt and Rolston, 2012; Castro *et al.*, 2010]. Despite the ultralow energy scales accessible with laser cooled gases, reaching deep into the strongly coupled regime has however remained out of reach as rapid temperature rises are observed when forming a plasma, partly due to the initially random distribution of the atoms [Kuzmin and O'Neil, 2002b]. This disorder-induced heating arises as the Coulomb interaction energy is converted into kinetic energy of the ions [Pohl *et al.*, 2004a; Bergeson *et al.*, 2011], posing one of the primary limits to the attainable coupling strengths in current experiments [Simien *et al.*, 2004; Cummings *et al.*, 2005]. In an attempt to overcome this limit, several proposals have been put forward including direct laser cooling of the ions [Kuzmin and O'Neil, 2002a; Killian *et al.*, 2003], or forming a plasma from an initially spatially correlated gas, for example, by introducing order via optical lattice potentials [Gericke and Murillo, 2003; Pohl *et al.*, 2004b], or by exploiting Pauli-blocking in a spin-polarized degenerate Fermi gas [Murillo, 2001].

Another, seemingly natural approach to mitigate disorder-induced heating, is to form a plasma from a Rydberg gas [Gericke and Murillo, 2003], as its constituents can be easily ionized and — given high densities — strong Rydberg–Rydberg interactions naturally result in strong spatial correlations [Robicheaux and Hernández, 2005] in the initial state. However, up until recently [Weber *et al.*, 2012] only attractively interacting Rydberg gases have been considered for plasma formation for which mechanical collapse driven by attractive forces [Amthor *et al.*, 2007b; Pillet *et al.*, 2009] and anisotropic interactions could destroy the correlations.

5.1 Generation of an ultracold plasma from a Rydberg-blockaded gas

In this chapter we report on the formation dynamics of an ultracold plasma from an initially spatially correlated gas of *isotropic* and *repulsively* interacting Rydberg atoms in the blockade regime. Despite the relative stability of repulsively interacting Rydberg ensembles, we observe, after a well defined and controllable time, a spontaneous avalanche ionization, as evidenced by a sudden increase in the number of detected ions, accompanied by a depletion of the ground and Rydberg state populations. We point out the relevant processes leading to plasma formation in this system, and using a simple coupled rate-equation model (see Sec. 5.4) we quantify the relevant formation rates. We observe that repulsive interactions delay the onset of avalanche ionization, leading to a new density dependence. We estimate that the typical timescale for plasma formation is short compared to the motional dynamics of the ions, suggesting that the initial correlations should be preserved in the plasma phase.

The basic principle behind our observations can be understood in three main stages which are illustrated in Fig. 5.1. (I) An initially randomly distributed gas of ultracold neutral atoms is excited to Rydberg states via a continuous two-photon laser coupling. (II) Due to the Rydberg blockade, each Rydberg-excited atom blocks further excitations within the blockade radius R_{bl} leading to density–density correlations which resemble those of a gas of hard spheres as explained in Sec. 2.2.4. After a short time, the Rydberg density reaches steady state, however over time Rydberg atoms start to decay by a combination of blackbody photoionization [Beterov *et al.*, 2007] and ionizing collisions with atoms in the ground and intermediate states [Barbier and Cheret, 1987; Kumar *et al.*, 1999], which leads to a gradual increase in the number of charged particles in the system. (III) Once a critical number of ions N_{crit} accumulates the resulting space charge can trap subsequently produced electrons. At this critical time t_{crit}, rapid electron–Rydberg collisions trigger an ionization avalanche, leading to the formation of an ultracold plasma [Killian *et al.*, 2007]. Since the avalanche is triggered by the fast moving electrons the plasma forms rapidly compared to the motion of the ions. Therefore the original spatially ordered structure of the Rydberg ensemble should be preserved. This is predicted to reduce the effects of disorder-induced heating by several orders of magnitude [Murillo, 2001]. Finally, after this sudden ionization of most of the Rydberg ensemble, the continuous laser excitation feeds the avalanche until the ground state population is fully

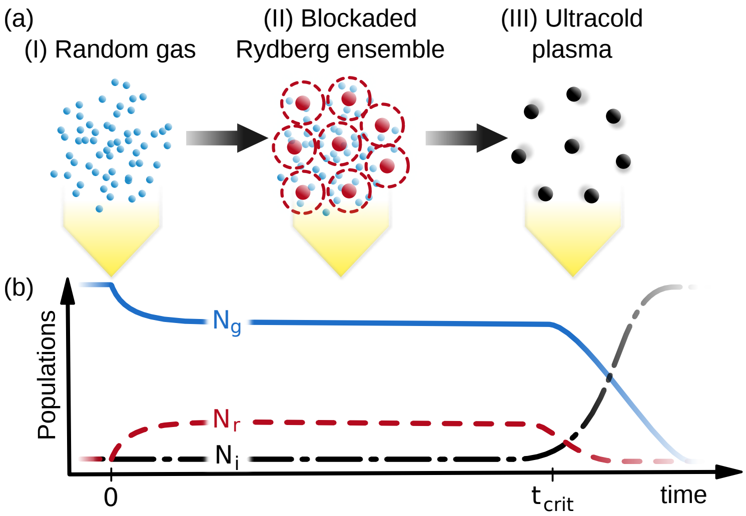

Figure 5.1: Generation of an ultracold plasma from a Rydberg-blockaded gas. (a) An initially uncorrelated gas of ultracold atoms is prepared in an optical dipole trap (I). By coherent laser coupling we excite some atoms to a Rydberg state. The strong Rydberg–Rydberg interactions prevent the excitation of close-by pairs, leading to spatial correlations (II). After a time t_{crit} the Rydberg gas is observed to spontaneously ionize into an ultracold plasma (III). (b) Qualitative dynamics of the involved populations: ground state atoms N_g (solid line), Rydberg atoms N_r (dashed line), and ions N_i (dash-dotted line).

depleted. In our experiments we independently measure the atom number in the ground or intermediate state N_g, the Rydberg atom number N_r, and the ion number N_i in a small excitation volume through a combination of absorption imaging and ionization detection. In a single beam optical dipole trap[i] we prepare dense atomic samples of up to 1.5×10^5 atoms in the $|5S_{1/2}, F=2\rangle$ state which are hold in the trap for a short time to equilibrate at a temperature of $T = 230\pm30\,\mu\mathrm{K}$. After a typical time-of-flight of $t_{\mathrm{TOF}} = 200\,\mu\mathrm{s}$ the cloud has expanded to a radially symmetric Gaussian distribution with $e^{-1/2}$-radii of $r_{\mathrm{radial}} = 28\pm1\mu\mathrm{m}$ and $r_{\mathrm{axial}} = 310\pm10\mu\mathrm{m}$. The peak atomic density is varied between $n_0 = (1-10)\times10^{10}\,\mathrm{cm}^{-3}$ while maintaining an approximately constant cloud shape by reducing the overall atom number during trap loading.

Rydberg atoms in the $|55S_{1/2}\rangle$ state are excited using a doubly resonant narrowband two-photon excitation via the intermediate $|5P_{3/2}\rangle$ state (see Fig. 5.2). Both lasers are aligned perpendicular to the symmetry axis of the cloud. The first excita-

---

[i] In these experiments only the 'dimple' trap was used.

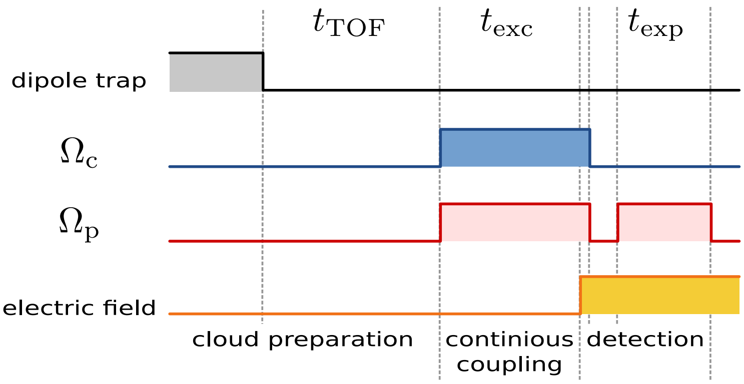

Figure 5.2: Experimental cycle. After trap release the cloud freely expands during a time-of-flight t_{TOF}. The coupling laser (Rabi frequency Ω_{c}) and the probe laser (Ω_{p}) then continuously couple the system during t_{exc}. The coupling is terminated by the switch-on of the electric field which stops the Rydberg excitation dynamics and field ionizes the Rydberg atoms. $1\,\mu$s after the field ionization the sample is once again exposed by the probe laser for $t_{\mathrm{exp}} = 10\,\mu$s to take an absorption image of the ground state atoms.

tion step is realized with a nearly uniform beam at 780 nm wavelength with intensity $I_{\mathrm{p}} = 2.9\,\mathrm{mW/cm^2}$. The second laser, at 480 nm, is aligned counter propagating to the first and is focused onto the center of the cloud with a Gaussian waist $w = 40\,\mu$m and a peak coupling strength $\Omega_{\mathrm{c}}/2\pi = 5.8\,$MHz. The excitation volume V, defined by the intersection of the cloud and coupling beam (see Fig. 3.1 on page 36), is approximated by a cylinder along the coupling beam, of length $L = \sqrt{2\pi} r_{\mathrm{radial}} \approx 70\,\mu$m and radius $R = w/\sqrt{2} \approx 28\,\mu$m. To perform the experiment we simultaneously pulse on both lasers for times t_{exc} ranging from 0 to $38\,\mu$s. During this time, the excitation volume changes by less than $\sim 20\,\%$. To stop the excitation, we switch on an electric field which field ionizes the Rydberg atoms and subsequently guides all ions to a micro-channel plate detector.

5.2 Strongly blockaded Rydberg gas

We first investigate the dependence of the Rydberg population on the peak density n_0 for a short excitation time $t_{\mathrm{exc}} = 3.7\,\mu$s (Fig. 5.3), at which we can rule out the influence of spontaneously formed ions. We observe the characteristic nonlinear dependence and saturation of N_r which is a consequence of Rydberg blockade [Singer *et al.*, 2004; Tong *et al.*, 2004]. The observed scaling is well described using the

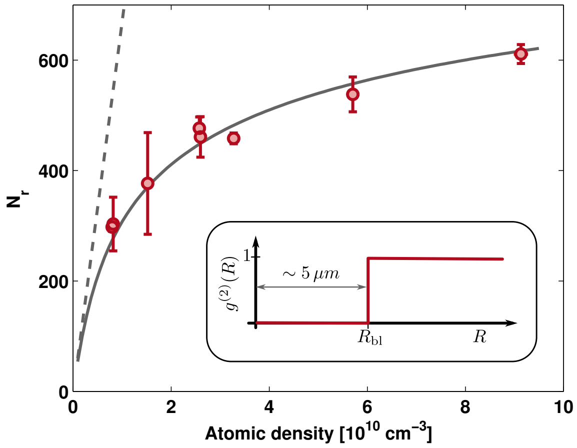

Figure 5.3: Density dependence of the Rydberg number for short times. The atoms in $|55S\rangle$ are field ionized after $3.7\mu s$ of continuous laser coupling. Strong interactions lead to a Rydberg excitation suppression for increasing ground state densities, in contrast to the interaction-free case (dashed line). The data is in good agreement with a hard sphere model (solid line) with a sphere diameter corresponding to the blockade radius $R_{\rm bl} \approx 5\,\mu m$. The inset shows an approximated spatial correlation function $g^{(2)}(R)$ typical for a Rydberg blockaded gas [Robicheaux and Hernández, 2005].

steady state of a classical rate equation model (solid line in Fig 5.3) [Ates *et al.*, 2011]. In this model, each Rydberg-excited atom is assumed to produce an exclusion sphere of radius $R_{\rm bl} \approx \sqrt[6]{(2C_6\Gamma_e)/\Omega_{\rm c}^2}$ which reduces the fraction of ground state atoms available for subsequent excitation. From the strength of the van der Waals interactions, $C_6/2\pi \approx -50$ GHz μm^6 for the $|55S_{1/2}\rangle$ state, and from the intermediate state decay rate, $\Gamma_e/2\pi \approx 6.1$ MHz, we get $R_{\rm bl} \approx 5\,\mu$m. We assume independent excitation $A \times \mathcal{V}$ and de-excitation rates B as introduced in Sec. 2.2.4. Interactions are accounted for through the fraction of available ground state atoms $\mathcal{V} \leq 1$, which decreases for increasing Rydberg density. This is estimated using the Carnahan-Starling expression for hard spheres [Talbot *et al.*, 1991]. The ratio $A/(A+B) = 0.38$ is constrained by the steady state solution to the single-atom, three-level optical Bloch equations for our experimental parameters.

From this model we derive the steady state Rydberg atom number N_r as a function of the ground state peak density n_0 assuming homogeneous density and coupling strength in the excitation volume. As seen in Fig. 5.3 the hard sphere model is in excellent agreement with the data, with the overall detection efficiency $\mathcal{D} \sim 0.4$ as only adjustable parameter. From comparison to the data we find that interactions suppress the number of Rydberg atoms by up to a factor of eight. At the highest densities the fraction of blockaded atoms is $1-\mathcal{V}\approx 0.9$, and the packing fraction $\eta=\pi N_{\mathrm{r}}R_{\mathrm{bl}}^3/6V\approx 0.2$, which indicates the presence of strong correlations in the system.

5.3 Ionization dynamics

To study the evolution of the system we probe the ground state atomic distribution using resonant absorption imaging. This is performed using a second light pulse on the lower transition, applied $1\,\mu s$ after the end of the Rydberg excitation (see Fig. 5.2). Typical results are shown in Fig. 5.4 (a) as a sequence of absorption images of the center of the cloud, recorded for different excitation times, at a density $n_0 = 2.8\times10^{10}\,\mathrm{cm}^{-3}$. For times longer than $\approx 10\,\mu$s we observe the appearance of a hole coinciding with the position of the focused 480 nm excitation laser. Over $10-20$ μs the hole grows until the cloud becomes locally transparent. We estimate the remaining number of atoms N_g in the excitation volume (shown in Fig. 5.4 (b)) by fitting to the images the difference of two peak functions, as explained in Sec. 3.7.2. The time-dependence shows initially a slow decrease of the ground state atom number, until a critical time $t_{\mathrm{crit}}\approx 12$ μs at which point we observe the start of a rapid depletion.

This behavior is a signature of the ionization avalanche of the Rydberg population. To independently measure the Rydberg atom number N_r and ion number N_i, we perform two experiments: in the first, we use an electric field above the Rydberg ionization threshold $\mathcal{E}^{(\infty)}$, and we detect both Rydberg atoms and ions using the micro-channel plate. In a second experiment, we switch a field below the ionization threshold[ii], which has a negligible effect on the Rydberg atoms but is sufficient to guide the ions to the detector. After relative calibration of the detection efficiencies for both experiments, we subtract the two signals to deduce N_r and N_i individually (Fig. 5.4 (c)). The Rydberg population reaches a quasi-steady state value ≈ 500 after $\approx 4\mu$s. Around a critical time $t_{\mathrm{crit}}\approx 12\,\mu$s, the number of ions reaches $N_i = 120$ and starts to increase rapidly. This number is already sufficient to trap electrons, thus leading to the formation of an ultracold plasma [Killian *et al.*, 2007], with lifetime $\approx$ 9 μs. Applying a small electric field during excitation suppresses the avalanche ionization, thereby confirming that the plasma formation is related to an accumulation of charges.

[ii] Contrary to the detection method used in Ch. 4 where we used a slowly rising electric field ramp, we here switch electric fields within a rise time of ≈ 300 ns.

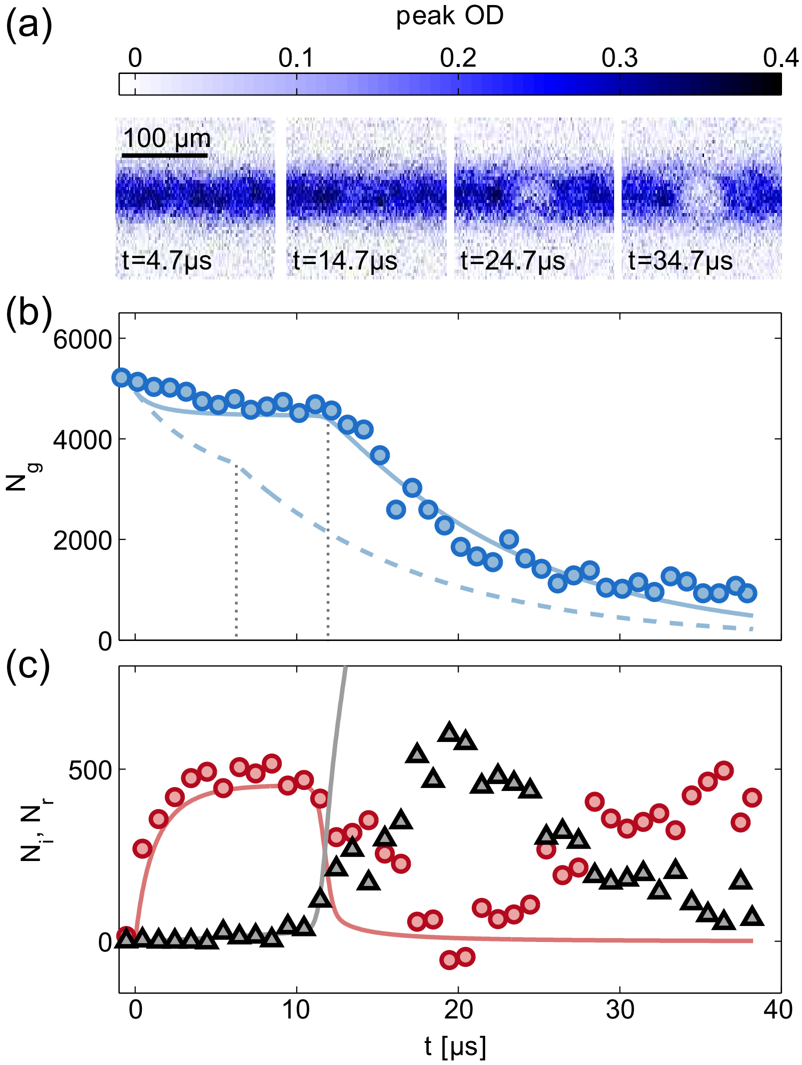

Figure 5.4: Measurement of the complete avalanche ionization dynamics. (a) Absorption images taken after different durations of continuous laser coupling on a cloud of initial peak density $n_0 = 2.8 \times 10^{10}\,\mathrm{cm}^{-3}$. (b) Number of ground state atoms N_g in the excitation volume. The data are compared to a rate equation model (see Sec. 5.4), accounting for (solid line) or neglecting (dashed line) the Rydberg blockade mechanism. Vertical lines highlight the avalanche onset time. (c) Simultaneously recorded Rydberg atom population N_r (circles) and ion population N_i (triangles).

5.4 Coupled rate equation model

The observed dynamics can be described using a simple coupled rate equation model which incorporates the Rydberg blockade effect, seed ionization processes, and an avalanche term driven by ionizing electron–Rydberg collisions. Only two coupled differential equations describe the evolution of the system:

$$\dot{N}_g = -A\mathcal{V}N_g + BN_r \tag{5.2a}$$

$$\dot{N}_r = A\mathcal{V}N_g - BN_r - \gamma_{\mathrm{bbi}}N_r - \gamma_{\mathrm{col}}N_rN_g/V - \gamma_{\mathrm{av}}N_rN_e/V\,. \tag{5.2b}$$

The number of ions N_i and the number of electrons N_e trapped in the plasma are deduced from the conservation of the total particle number N_{tot}

$$N_i = N_{\mathrm{tot}} - N_g - N_r \tag{5.3a}$$

$$N_e = N_i - N_{\mathrm{crit}}\,, \qquad \text{if} > 0\,. \tag{5.3b}$$

Here, N_{tot} and the volume V were assumed to remain constant, corresponding to a neglect of plasma expansion. Furthermore the electron trapping criterion was considered, after which N_{crit} is the critical ion number necessary to form a space charge potential large enough to trap electrons [Killian *et al.*, 2007]. N_{crit} depends on the geometry of the volume and on the kinetic energy of the electrons which we assume to be half of the electron binding energy W_e. Approximating the volume by a homogeneous cylinder of length L and radius R, we evaluate the critical ion number to be

$$N_{\mathrm{crit}} = \frac{8\epsilon_0}{q^2}\,\frac{W_e\pi R^2L}{\left[L(-L+\sqrt{L^2+4R^2}) + 4R^2\mathrm{csch}^{-1}(2\mathrm{R}/\mathrm{L})\right]}\,, \tag{5.4}$$

where ϵ_0 is the vacuum permittivity, q is the electron charge, and csch^{-1} is the inverse hyperbolic cosecant function.

The first two terms on the right hand side of (5.2a) and (5.2b) describe the excitation and de-excitation of Rydberg atoms and their steady state solution was used to fit the data in Fig. 5.3. We attribute the seed processes to a combination of blackbody photoionization [Beterov *et al.*, 2007] and ionizing collisions either with ground state atoms or with the relatively large population in the intermediate state $\left|5P_{3/2}\right\rangle$ [Barbier and Cheret, 1987; Kumar *et al.*, 1999]. The third term in (5.2b) describes the blackbody photoionization with the state dependent rate γ_{bbi} $\approx 150/s$ [Beterov *et al.*, 2007]. The more dominant seed mechanism is described by the nonlinear seed ionization rate γ_{col} which is related to an effective collision cross-section σ_{col} between Rydberg atoms and atoms in either the ground or the intermediate state:

$$\gamma_{\mathrm{col}} = \sigma_{\mathrm{col}} \sqrt{\frac{16 k_B T}{\pi m_{\mathrm{Rb}}}} \,. \tag{5.5}$$

Here T is the temperature of the atomic cloud, k_B is the Boltzmann constant, and m_{Rb} is the mass of ^{87}Rb. It should be mentioned that on the observed timescale, the repulsive $|55S_{1/2}\rangle$ atoms are not expected to undergo ionizing Rydberg–Rydberg collisions at a sufficient rate to seed the avalanche [Amthor *et al.*, 2007a]. The avalanche process itself is described by a nonlinear rate γ_{av} which is related to the electron energy W_e by

$$\gamma_{\mathrm{av}} = \sigma_{\mathrm{geo}} \sqrt{\frac{W_e}{m_e}} \,, \tag{5.6}$$

where the electron mass is given by m_e and $\sigma_{\mathrm{geo}} = \pi \mathsf{n}^{\star 4} a_0^2$ is the geometric cross-section of Rydberg atoms [Vitrant *et al.*, 1982], with $\mathsf{n}^\star$ the effective principal quantum number and a_0 the Bohr radius. This process depends on the number of electrons $N_e = N_i - N_{\mathrm{crit}}$ trapped in the plasma, which collisionally ionize the remaining Rydberg atoms further feeding the avalanche. We neglect the role of ion–Rydberg interactions, assuming the net charge imbalance is relatively small and the ions are effectively screened by the mobile electrons. This assumption is consistent with our experimental observation that the Rydberg resonance does not significantly shift after plasma formation, but only becomes broadened, as recently pointed out by [Weber *et al.*, 2012].

We fit the model results simultaneously to a set of ground state depletion curves, with initial atomic densities ranging from $(0.8 - 9) \times 10^{10}\mathrm{cm}^{-3}$. Typical depletion curves are shown in Fig. 5.5. The introduced model only has three free parameters that are extracted from the model:

(*i*) The overall Rydberg excitation rate A from the ground and intermediate states.

(*ii*) The effective seed collisional ionization cross-section σ_{col}.

(*iii*) And the average energy of trapped electrons W_e, which constrains both N_{crit} and the nonlinear rate for electron–Rydberg collisions γ_{av}.

Typical predictions of the model are shown in Fig. 5.4 (b) & (c). The distinct evolution of ground state atom population N_g is well reproduced, although the model does not completely reproduce Rydberg population N_r and the produced number of ions N_i after the avalanche. We attribute this to three-body recombination towards

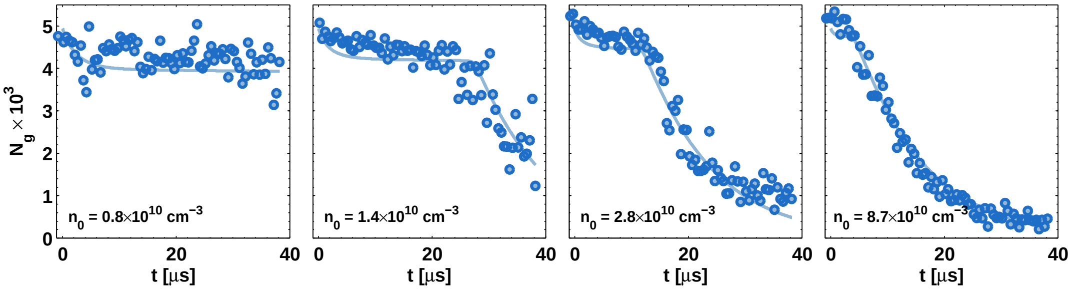

Figure 5.5: Density dependence of the ground state depletion caused by the ionization avalanche. Number of ground state atoms in the excitation volume versus continuous coupling time. The data in each plot is inferred from 81 absorption images, which were acquired during a sequence of consecutive experimental runs. The rate equation model (solid lines) was simultaneously fitted to all displayed data and has only three free parameters (see text). It shows very good agreement with the data illustrating the model validity over one order of magnitude in density.

Rydberg states counted in the detection process, and to plasma expansion, both not included in the model. The best fit parameters and uncertainties are:

(*i*) $A = (8.7 \pm 0.3) \times 10^{-2}\,\mathrm{MHz}$;

(*ii*) $\sigma_{\mathrm{col}} = 0.73{\pm}0.21\,\mu\mathrm{m}^2$, a factor of 8-15 larger than the geometrical cross-section of $|55S\rangle$ Rydberg atoms ($\sigma_{\mathrm{geo}} \approx 0.064\,\mu\mathrm{m}^2$);

(*iii*) finally $W_e = (3.0\,\pm 0.9) \times 10^{-3}\,\mathrm{eV}$, which amounts to approximately 60% of the electron binding energy in $|55S_{1/2}\rangle$, similarly to [Li *et al.*, 2004]. Given our geometry, the obtained electron energy relates to $N_{\mathrm{crit}} = 26 \pm 7$ which corresponds to typically 5 % of the initial Rydberg number. The nonlinear avalanche rate $\gamma_{\mathrm{av}} \approx (1500 \pm 200)\,\mathrm{MHz}\,\mu\mathrm{m}^3$.

To investigate the regimes in which a plasma develops, we extracted the onset time t_{crit} of the ionization avalanche from the data and plotted it as a function of density (Fig. 5.6). We observe a critical dependence, following an approximately power law of $t_{\mathrm{crit}} \propto n_0^{-\beta}$ with $\beta = 1.0 \pm 0.1$ on the considered density range. We have also studied the role of the excitation volume by performing experiments for a shorter time-of-flight of $t_{\mathrm{TOF}} = 100\ \mu\mathrm{s}$, which leads to a reduced excitation volume $V_{\mathrm{reduced}} \approx V/2$. We observe that the onset times are delayed, since the critical ion number N_{crit} required for electron trapping decreases less strongly with V than the total atom number [Killian *et al.*, 2007]. This effect is well reproduced by the model,

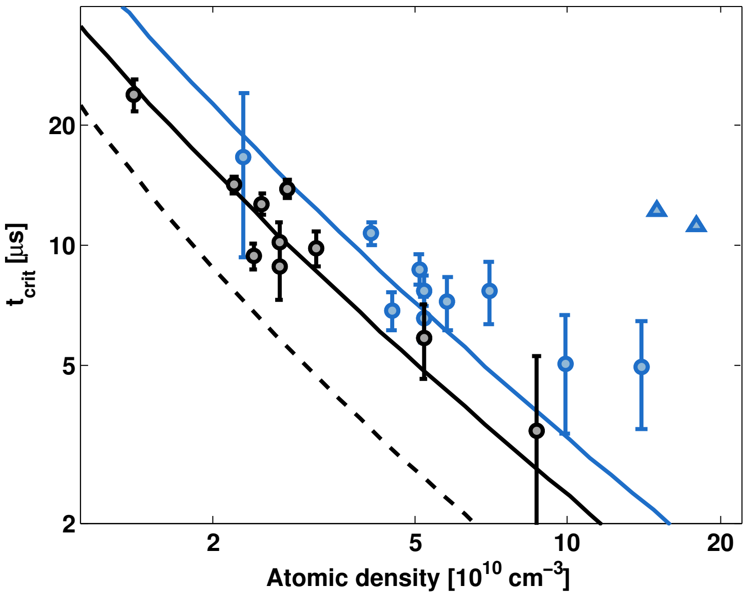

Figure 5.6: Density dependence of the ionization avalanche onset time t_{crit} plotted on a log-log scale. Dark and light symbols correspond to experiments with excitation volumes V and $V_{\mathrm{reduced}} \approx V/2$, respectively. Circles and triangles correspond to measurements performed with $|55S_{1/2}\rangle$ and $|40S_{1/2}\rangle$ states, respectively. The solid lines are the model predictions for $|55S_{1/2}\rangle$ for both excitation volumes V and V_{reduced}, using the same fit parameters. The dashed line shows the model outcome for the excitation volume V with the blockade effect being neglected.

when accounting for the new geometry with conserved rates and cross-sections (see Fig. 5.6).

To further study the effect of Rydberg interactions on the avalanche dynamics, we compared the dynamics from different Rydberg states, while keeping all other experimental parameters (in particular Ω_{c}) approximately constant. In comparison to $|55S_{1/2}\rangle$, the $|40S_{1/2}\rangle$ state appears more stable, exhibiting plasma formation in V_{reduced} only above densities of $n_0 \approx 1 \times 10^{11}\,\mathrm{cm}^{-3}$ (triangles in Fig. 5.6). Rescaling the parameters $\sigma_{\mathrm{col}}, \gamma_{\mathrm{av}} \propto \mathsf{n}^{\star 4}$; $R_{\mathrm{bl}} \propto \mathsf{n}^{\star 11/6}$; and $W_e \propto 1/\mathsf{n}^{\star 2}$ [Li *et al.*, 2004], the model accounts for approximately half of the relative shift in t_{crit}. This discrepancy could be due to a different scaling of the ionization cross-section σ_{col}. For the attractively interacting $|55D_{3/2}\rangle$ state we observe an immediate production of ions ($t_{\mathrm{crit}} \to 0$), presumably due to the anisotropy of $|D\rangle$ state interactions which breaks the blockade effect and leads to an increased rate of ionizing Rydberg–Rydberg collisions [Amthor *et al.*, 2007b].

5.5 Rydberg blockade as a route to strongly coupled plasmas

From the model we conclude that the Rydberg blockade has a significant effect on the formation of the ultracold plasma, delaying the ionization onset time by typically 80 % for the data shown in Fig. 5.6. In such a time, Rydberg interactions are suspected to develop strong spatial correlations [Robicheaux and Hernández, 2005]. These correlations are expected to become more pronounced as the atomic density is increased and more atoms are contained inside each blockade volume [Ates and Lesanovsky, 2012]. Our model predicts a sudden avalanche ionization of the complete Rydberg ensemble within $\approx 2\mu$s. Within this time, the ions only move by at most 600 nm, which is much less than their average spacing ($\gtrsim R_{\text{bl}}$). Thus, the correlations from the Rydberg sample are most likely preserved in the avalanche. The observed packing fraction $\eta \approx 0.2$ is similar to the highest considered in [Murillo, 2001]: provided the laser coupling is turned off immediately after t_{crit}, we expect that the importance of disorder-induced heating as compared to final ion interactions should be strongly reduced.

In this chapter, we have for the first time experimentally investigated the spontaneous evolution from a strongly blockaded and spatially correlated Rydberg gas to an ultracold plasma. The combination of absorption imaging and ion detection allowed us to observe the complete dynamics of this process. In particular we identified a regime in which the ionization avalanche is faster than the motional timescale of the produced ions, suggesting that the Rydberg correlations might have been imprinted onto the plasma ions. This could provide a new route to the production of strongly coupled ultracold plasmas with large ionic coupling parameters. In addition, Rydberg states even offer the possibility to tune of the correlation length given by $R_{\text{bl}} \propto \mathsf{n}^{\star 11/6}$. Using Rydberg states between $\mathsf{n} = 40$ and $\mathsf{n} = 100$, the correlation length can be accurately tailored between $\approx 2.7\,\mu$m and $\approx 15.5\,\mu$m. Future experiments could directly resolve the spatial structure of the resultant plasmas, for example by using atomic species with more than one valence electron [McQuillen *et al.*, 2012], or by using Rydberg states as a sensitive probe [Günter *et al.*, 2012; Olmos *et al.*, 2011]. This would open promising new avenues to experimentally investigate novel effects in ultracold plasmas, such as liquid-vapor phase coexistences, critical points [Shukla and Avinash, 2011] and strongly coupled liquid phases.

Chapter 6

Sub-Poissonian statistics of Rydberg-interacting dark-state polaritons

This chapter is based on the following manuscript:

Sub-Poissonian statistics of Rydberg-interacting dark-state polaritons
C. S. Hofmann, G. Günter, H. Schempp, M. Robert-de-Saint-Vincent,
M. Gärttner, J. Evers, S. Whitlock, M. Weidemüller
arXiv:1211.7265 (2012); submitted for publication

At the few-photon level, electromagnetically induced transparency is characterized by the propagation of coupled excitations of atoms and light called dark-state polaritons [Fleischhauer and Lukin, 2000]. These long-lived quasi-particles simultaneously possess the properties of both the photonic and the atomic degrees of freedom which can be interchanged in a fully coherent and reversible process. As coupled excitations of light and matter, dark-state polaritons acquire many new properties from the atomic system. This has been used, for instance, to slow down or even stop light [Hau *et al.*, 1999; Liu *et al.*, 2001; Phillips *et al.*, 2001; Bajcsy *et al.*, 2003], to imprint a magnetic moment onto light fields [Karpa and Weitz, 2006], or to realize giant electro-optical effects in atomic vapors [Mohapatra *et al.*, 2008]. Qualitatively new many-body effects occur when coupling light to *strongly interacting* atomic systems. Polariton–polariton interactions mediated by the atomic admixture can lead to highly nonlinear [Pritchard *et al.*, 2010; Peyronel *et al.*, 2012; Parigi *et al.*, 2012] and nonlocal optical effects [Sevinçli *et al.*, 2011b] as well as to the emergence of correlations in both the atomic and the light fields [Gorshkov *et al.*, 2011]. The ability to produce and coherently control the propagation of quantum fields using interacting dark-state polaritons will open up new applications including few-photon nonlinear optics [Pritchard *et al.*, 2012], nonclassical light sources [Dudin and Kuzmich, 2012; Peyronel *et al.*, 2012; Maxwell *et al.*, 2012; Pritchard, 2012], photonic quantum logic gates [Friedler *et al.*, 2005; Petrosyan and Fleischhauer, 2008] and the generation of squeezed states of atomic ensembles [Opatrný and Mølmer, 2012].

In this chapter we experimentally study both light and matter aspects of strongly interacting dark-state polaritons in a dense atomic gas involving Rydberg states. An important feature of this system is that the Rydberg blockade gives rise to dissipative hard-core interactions and ultimately to correlations between dark-state polaritons [Gorshkov *et al.*, 2011]. In contrast to the usual approach, in which electromagnetically induced transparency is observed optically, we explore a new approach which benefits from a high detection sensitivity to Rydberg atoms and directly probes the matter-part of the polariton wavefunction. In this way we extend upon recent work which has shown the development of nonclassical photon correlations in the transmitted light field [Petrosyan *et al.*, 2011; Peyronel *et al.*, 2012]. Since the mapping between the properties of the light field and the atomic system is in general nontrivial [Peyronel *et al.*, 2012], it is important to study both aspects to obtain a complete picture of EIT in strongly interacting systems. Our experiments cover four orders of magnitude in atomic density which we use to observe the nonlinear optical response and temporal dynamics of polaritons, as well as to investigate the transition to sub-Poissonian polariton statistics when entering the strongly interacting regime. Using a state-of-the-art theoretical approach for the coupled atom–light system, developed by M. Gärttner and J. Evers [Heeg *et al.*, 2012], we find good agreement with all aspects of the experiment except for the level of sub-Poissonian fluctuations. We observe atomic correlations that are significantly stronger than can be accounted for by assuming the propagation of classical light fields alone. This indicates that the recently observed modification of photon statistics of propagating light fields due to Rydberg interactions [Peyronel *et al.*, 2012] can cause a significant back-action on the Rydberg atom statistics.

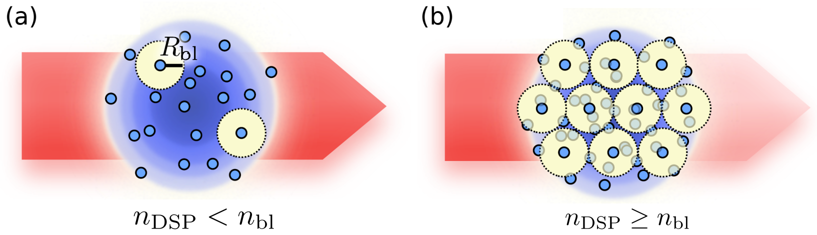

Figure 6.1: Polariton blockade and nonlinear absorption. Cross-section of the atomic cloud (blue) showing the effect of Rydberg blockade on polariton statistics and nonlinear absorption of a weak probe beam (red) for small (a) and large (b) polariton densities.

6.1 Polariton–polariton interactions

In the discussion in Sec. 2.3.4 it was mentioned that in the weak probe limit, a single probe photon will be partially converted into a collective excitation of the medium to become a dark-state polariton [Fleischhauer and Lukin, 2000],

$$|D,1\rangle = \cos\vartheta\,|G,1\rangle - \sin\vartheta\,|R,0\rangle \tag{6.1}$$

where the collective quantum states involving N atoms and the light field are $|G,1\rangle = |g_1,\cdots,r_i,\cdots,g_N\rangle\,|1\rangle$ and $|R,0\rangle = 1/\sqrt{N}\sum_i |g_1,\cdots,r_i,\cdots,g_N\rangle\,|0\rangle$. The mixing ratio $\tan(\vartheta) = \sqrt{n\sigma c\Gamma_e}/\Omega_{\rm c}$ determines the properties of the polariton depending on the atom density n, the resonant scattering cross-section σ, and the speed of light c. The dark-state polariton propagates through the atomic medium with negligible loss and reduced group velocity $v_g \approx c/\tan^2(\vartheta)$.

To understand how interactions between dark-state polaritons arise we provide the following simple physical picture. For weak probe intensities and for low atomic densities (Fig. 6.1 (a)) each incident photon is converted into a dark-state polariton which propagates freely through the EIT medium before being coherently converted back to the original optical mode. If the light field is subsequently detected on a CCD camera this is observed as transparency of the atomic cloud. For increasing atomic density the group velocity drops ($\vartheta \to \pi/2$), effectively compressing the probe field inside the atomic cloud and increasing the density of dark-state polaritons $n_{\rm DSP}$ until several begin to occupy the same volume. Since a single polariton includes a large Rydberg state component, it interacts strongly with the Rydberg states of nearby atoms which become shifted out of resonance, breaking the EIT condition for additional excitations and leading to strong inelastic scattering of excess photons from the cloud [Petrosyan *et al.*, 2011]. This imposes a critical density of dark-state polaritons $n_{\mathrm{bl}} \approx (4\pi R_{\mathrm{bl}}^3/3)^{-1}$ corresponding to approximately one per blockade volume, beyond which the density of dark-state polaritons saturates (Fig. 6.1 (b)).

6.2 Nonlinear optical response of the Rydberg EIT medium

We use ^{87}Rb atoms with states $|g\rangle = \big|5S_{1/2}, F=2\big\rangle$, $|e\rangle = \big|5P_{3/2}, F=3\big\rangle$ with $\Gamma_e/2\pi = 6.1$ MHz, and the Rydberg state $|r\rangle = \big|55S_{1/2}\big\rangle$ which has a lifetime of $\approx 80\ \mu$s. We prepare a cigar shaped cloud of approximately 5×10^4 atoms at a temperature of 5 μK in an optical trap. The atomic cloud is uniformly illuminated from the side by a circularly polarized probe beam with intensity $I_{\mathrm{p}} = 5\,\mu\mathrm{W/cm}^2$ and the transmitted light is imaged onto a CCD camera with an optical resolution of $\approx 12\,\mu$m (Rayleigh criterion). The coupling laser is counter aligned to the probe beam and passed through a diffractive optical element to create an approximately uniform intensity profile with $\Omega_{\mathrm{c}}/2\pi = 5.1\,$MHz over an elliptical region of $\approx 65 \times 130\,\mu\mathrm{m}^2$ which was characterized in Sec. 3.7.3. The frequencies of both lasers are tuned to the atomic resonances. The measured linewidths (including both decay and dephasing terms) for the probe transition and the two-photon transition are $\gamma_{eg}/2\pi \approx 6.4\,$MHz and $\gamma_{gr}/2\pi \approx 1.7\,$MHz respectively, which gives an EIT coupling parameter $\mathcal{C} = \Omega_{\mathrm{c}}^2/(\gamma_{eg}\gamma_{gr}) = 2.4$ and an EIT resonance width of $\mathcal{W} = (1+\mathcal{C})\gamma_{gr} = 2\pi \times 5.8\,$MHz. The anticipated blockade radius is $R_{\mathrm{bl}} = (2C_6/\mathcal{W})^{1/6} \approx 5\,\mu$m with the van der Waals interaction strength $C_6 \approx -50\,\mathrm{GHz}\,\mu\mathrm{m}^6$. To control the atomic density before pulsing on the probe light we switch off the optical trap and vary the time-of-flight between 20 μs and 4.5 ms, varying the peak density (along the line-of-sight) between $n \approx 10^{13} - 10^{9}\,\mathrm{cm}^{-3}$. This is coupled to a change in the cloud length in the probe direction between $\approx 2\,\mu$m and $\approx 100\,\mu$m and a change in the optical density of the cloud between 3 (resolution limited) and 0.1 (see Fig. 6.2 (d)).

Figure 6.2 shows absorption images of the atomic cloud for three different expansion times corresponding to three different peak atomic densities. For long time-of-flights (corresponding to low densities $n \lesssim 10^{10}\,\mathrm{cm}^{-3}$) the cloud has expanded considerably, such that the excitation volume is defined primarily by the intensity profile of the coupling laser. Here we observe a high degree of transparency (*e.g.* Fig. 6.2 (a)), which can be attributed to the low density of dark-state polaritons. By analyzing the images we measure the absorption in both the transparency region and the background region corresponding to the two-level optical response (with susceptibility $\chi^{(2\mathrm{lv})}$). At low densities we find the optical response is linear corresponding

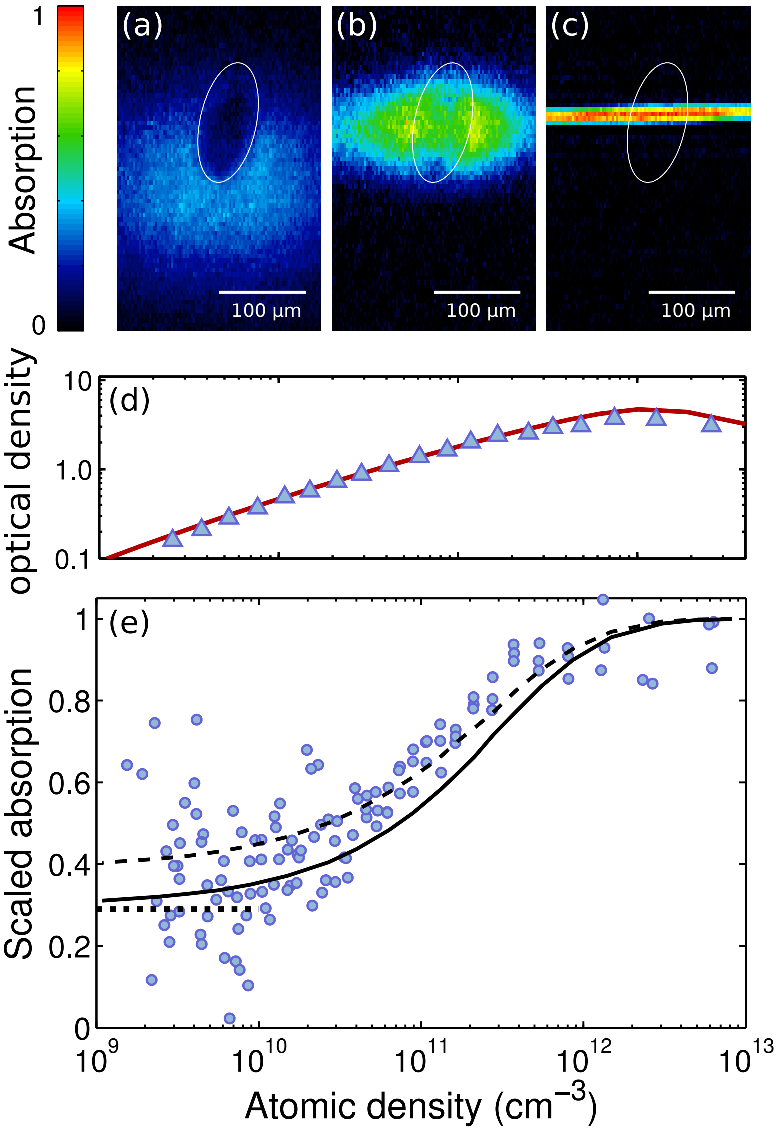

Figure 6.2: Nonlinear optical response of the Rydberg EIT medium. Absorption images of the atomic cloud for three expansion times with a probe intensity of $I_p = 5\ \mu$W/cm^2 and peak densities corresponding to (a) $n = 5 \times 10^9$ cm^{-3}, (b) $n = 5 \times 10^{10}$ cm^{-3} and (c) $n = 3 \times 10^{12}$ cm^{-3}. The EIT region illuminated by the coupling laser is indicated by white ellipses. (d) Measured optical density. The observed decrease at highest atomic densities is due to a limitation in optical resolution. (e) Measured absorption scaled to two level response as a function of peak atomic density. The dotted horizontal line shows the expected low density EIT absorption due to the finite laser linewidths. The solid and dashed curves are the results of the Monte-Carlo simulations of the coupled atom-light system with $\gamma_{gR}/2\pi$=1.7 MHz (solid) and $\gamma_{gR}/2\pi$=2.6 MHz (dashed).

to a scaled optical susceptibility $\chi^{(0)}/\chi^{(2\mathrm{lv})} = 0.31 \pm 0.07$ which is consistent with the expected on-resonant optical susceptibility in the noninteracting EIT regime $\chi^{(0)}/\chi^{(2\mathrm{lv})} = 1/(1+\mathcal{C}) \approx 0.29$. At densities above $n \approx 1 \times 10^{10}$ cm^{-3} we start to observe a decrease in the transparency due to interactions (*e.g.* Fig. 6.2 (b)). Above $n \approx 4 \times 10^{11}$ cm^{-3} the EIT spot vanishes almost completely (*e.g.* Fig. 6.2 (c)).

The full nonlinear optical response as a function of peak atomic density is shown in Fig. 6.2 (e). We observe a transition from transparent to fully absorbing by increasing the density. This characteristic behavior resembles that obtained by full many-body calculations of the optical susceptibility in a Rydberg blockaded gas [Ates *et al.*, 2011]. We use a rate equation model developed by M. Gärttner and J. Evers to make a quantitative comparison between theory and experiment. The model is an optimized version [Heeg *et al.*, 2012] of a rate equation model originally introduced by Ates *et al.* [Ates *et al.*, 2007b]. The simulation treats the full atom number within the coupling volume ($N \approx 5000 - 25000$; compare to Fig. 3.10 on page 52) assuming random positions distributed according to the measured Gaussian cloud shape. Monte-Carlo sampling is then applied to solve for the steady state populations in states $|g\rangle, |e\rangle$ and $|r\rangle$ for each atom, taking into account the level shifts due to interactions with nearby Rydberg atoms. Comparing the simulations to the experiment we find the effect of nonlinear absorption as the probe propagates through the cloud must be accounted for. To include the probe laser attenuation the model first solves for the local Rabi frequency $\Omega_\mathrm{p}^{(i)}$ which is attenuated by all other atoms $j < i$ in a cylindrical volume with cross-section[i] Σ. The degree of attenuation is given by $\Omega_\mathrm{p}^{(j+1)} = \Omega_\mathrm{p}^{(j)} \exp(-\chi^{(j)})$ where $\chi^{(j)}$ is proportional to the $|e\rangle$ state population of atom j. The local $\Omega_\mathrm{p}^{(j)}$ is determined recursively starting with $j = 1$ which is subjected to the total incident probe Rabi frequency $\Omega_\mathrm{p}^{(1)}$. The steady state populations are then solved for iteratively until $j = i$.

We find good agreement between the measured optical response and the results of the Monte-Carlo simulations (solid curve in Fig. 6.2 (d)) using the calculated interaction strength and all other input parameters determined from independent measurements. The simulations qualitatively reproduce the observed scaling of the nonlinear absorption, however we observe a systematic shift to higher densities, by about a factor of 2. The discrepancy could in part be explained by uncertainties in the dephasing of the Rydberg states due to laser fluctuations or atom motion which would effectively increase γ_{gr}. For comparison we show the results of the simulations with $\gamma_{gr}/2\pi$=1.7 MHz (solid curve) and $\gamma_{gr}/2\pi$=2.6 MHz (dashed curve).

---

[i] The outcome of this procedure does not depend on the exact choice of Σ (typically $3-10$ μm^2) as long as Σ is small compared to the size of the atomic cloud.

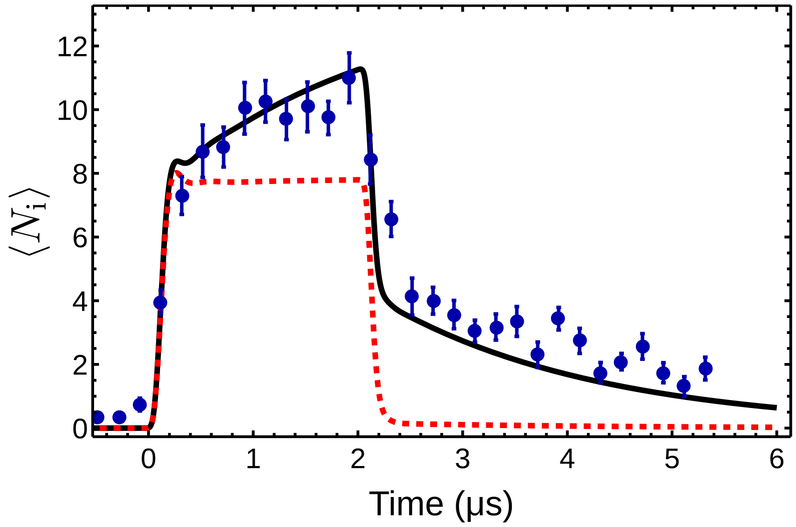

Figure 6.3: Polariton dynamics observed during a $2\,\mu$s probe pulse measured via the Rydberg state population. Measured polariton evolution with each data point which is the average of 20 runs of the experiment. The vertical error bars represent the statistical error of the mean. The solid line is a fit to the data using the numerical solution to the optical Bloch equations, including a coupling to both Rydberg Zeeman sublevels $m_j = \pm 1/2$ which accounts for the slow evolution and residual Rydberg population after $2\,\mu$s. The dashed red line shows the population in the resonantly coupled Zeeman state alone.

6.3 Polariton dynamics

In our experiments the dark-state polaritons are almost entirely matter-like (in eq. (6.1) $\cos^2(\vartheta) \approx 10^{-3} - 10^{-7}$). Therefore, measuring the Rydberg population serves as a projective measurement of the number of polaritons inside the cloud. This is possible by field ionizing the Rydberg states and subsequently detecting the individual ions on a micro-channel plate detector which provides high time resolution and near single particle sensitivity as discussed in Sec. 3.7.1. We apply an electric field just above ionization threshold to field ionize and guide the resultant ions to maximize the spread in arrival times. In a typical experiment we detect ≈ 10 ions. The probability for two ions to arrive simultaneously such that they are miscounted as a single event is less than 1%.

Figure 6.3 shows the measured time evolution of the number of detected ions during a $2\,\mu$s probe pulse in the noninteracting regime. At short times we observe a rapid increase of the detected ions reflecting the entry of dark-state polaritons into the atomic cloud. The observed rise time of $\approx 100\,$ns is compatible with the spectral width of the EIT resonance. After this time the number of detected ions approaches a steady state value of around $\langle N_\mathrm{i}\rangle \approx 10$, which, accounting for our ion detection efficiency ($\mathcal{D} \approx 0.4$) corresponds to ≈ 25 polaritons inside the cloud. After the pulse the Rydberg state population decreases rapidly, which is expected as the polaritons leave the atomic cloud and are coherently mapped back onto the light field. By analyzing the images we confirm that the cloud remains mostly transparent until the electric field is switched on. Over the full pulse duration we estimate a total of ~ 1500 polaritons pass through the atomic cloud. After the pulse we observe a residual population of about 30% of the peak number of ions and a slower time evolution. The dashed line in Fig. 6.3 shows the expected evolution found by solving the three-level optical Bloch equations. The additional slow rise during the pulse and the longer tail observed in the experiment can be attributed to laser coupling to additional Zeeman sublevels assuming polarization dependent coupling strengths (solid line in Fig. 6.3).

6.4 Polariton counting statistics

We now turn to the strongly interacting regime by increasing the atomic density which in turn increases the density of dark-state polaritons. After $2\,\mu$s of probe laser illumination we turn on the ionization field and count the number of detected ions. This is repeated between 150-300 times for each time-of-flight corresponding to different peak densities of the cloud. From these data we construct histograms of the ion number distribution (Fig. 6.4 (a)) which is used to extract the mean and variance of the number of polaritons.

In Fig. 6.4 (b) we show the measured mean ion number $\langle N_\mathrm{i}\rangle$ which is proportional to the number of dark-state polaritons inside the cloud. The low-density behavior is determined by the changing number of atoms in the excitation volume as a function of time-of-flight (dashed line). For $n > 10^{11}$ cm^{-3} we observe a rapid decrease of $\langle N_\mathrm{i}\rangle$ due to probe laser attenuation and polariton–polariton interactions. The solid line is the results of the Monte-Carlo simulation using the same parameters as for Fig. 6.2. To obtain the best agreement we adjust only two parameters in the simulation: the detection efficiency $\mathcal{D}$ and the effective area of the coupling laser ellipse. Optimal agreement is found for a coupling region with major axis radius of 65 μm and $\mathcal{D} = 0.4$.

Simultaneous to the onset of the polariton blockade we also observe a significant narrowing of the statistical distribution of the detected ions (Fig. 6.4 (a)). We

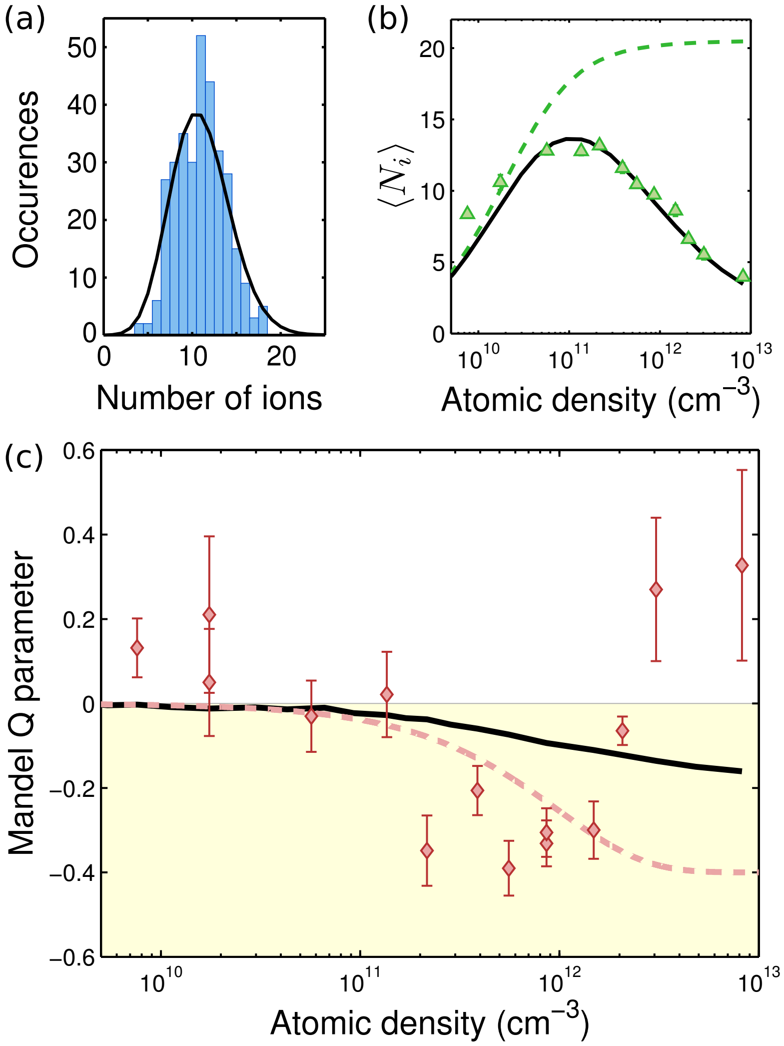

Figure 6.4: Statistical distribution of the detected ions during a $2\,\mu$s probe pulse showing the transition to sub-Poissonian statistics. (a) Typical ion number histogram for $n = 5 \times 10^{11}\,\text{cm}^{-3}$ with $Q = -0.3$ compared to a Poisson distribution with the same mean (solid line). (b) Measured mean number of ions as a function of atomic density which decreases above $n = 10^{11}\,\text{cm}^{-3}$ due to blockade. (c) In this regime the Mandel Q parameter falls to sub-Poissonian. The dashed curve is derived from the hard sphere model assuming an initial Poissonian photon number distribution with $n_{crit} = 1 \times 10^{12}\,\text{cm}^{-3}$. The statistical errors are estimated by dividing the data for each density into 3 subsets of 50 experimental runs each and then calculating the standard error of the mean Q parameter.

quantify this using the Mandel Q parameter

$$Q = \frac{\langle N_i^2 \rangle - \langle N_i \rangle^2}{\langle N_i \rangle} - 1, \tag{6.2}$$

which compares the width of an observed distribution to a Poisson distribution with the same mean as discussed in Sec. 2.2.5. For a Poissonian process $Q = 0$, whereas a sub-Poissonian process yields $Q < 0$ reflecting the emergence of spatial and temporal correlations [Ates *et al.*, 2006; Reinhard *et al.*, 2008b; Viteau *et al.*, 2012].

Figure 6.4 (c) shows the measured Mandel Q parameter as a function of the peak density of the atomic cloud. In the low-density limit, polariton–polariton interactions can be neglected and the measured ion number distributions are close to Poissonian with $Q \approx 0$ which is expected for a coherent input light field. Increasing the density we observe a clear transition to sub-Poissonian statistics with Q reaching a minimum value of -0.32 with a statistical uncertainty of 0.04 calculated in the range $2 \times 10^{11}\,\mathrm{cm}^{-3} < n < 2 \times 10^{12}\,\mathrm{cm}^{-3}$. Including the effect of imperfect ion detection indicates the true distribution of dark-state polaritons is much narrower corresponding to strong spatial and temporal correlations, since $Q_{\mathrm{DSP}} = Q/\mathcal{D}$ [Ates *et al.*, 2006].

Despite the good agreement of the Monte-Carlo model with both the optical response data (Fig. 6.2 (d)) and the mean number of polaritons (Fig. 6.4 (b)), it clearly fails to describe the experimentally measured Q parameters which are much lower than predicted (solid line in Fig. 6.4 (c)). We attribute this to the neglected effect of photon correlations (the Monte-Carlo algorithm assumes a classical field at each step characterized by a Rabi frequency Ω_{p}) which can build up as a consequence of dissipative polariton–polariton interactions [Peyronel *et al.*, 2012].

A complete and rigorous many-body treatment of this problem, including the effects of the quantized electromagnetic field is still lacking. However, we can make a simple estimate for the possible effects of photon correlations by assuming a hard sphere model for polariton interactions. We discretize the excitation volume into elements corresponding to the size of a blockade sphere and assume an initial Poisson distribution for the number of photons per element with a mean of $\langle N_{\mathrm{ph}} \rangle \approx (\Omega_{\mathrm{p}}/\Omega_{\mathrm{c}})^2 (n/n_{\mathrm{bl}})$ [Petrosyan *et al.*, 2011]. For $N_{\mathrm{ph}} \geq 1$ we assume one dark-state polariton is created with unity probability and the excess photons couple to bright states which do not have a Rydberg state component. Therefore the corresponding dark-state polariton statistics range from Poissonian character for $\langle N_{\mathrm{ph}} \rangle \ll 1$ (limited by the classical fluctuations of the laser field) to strongly sub-Poissonian for $\langle N_{\mathrm{ph}} \rangle \gg 1$ above the critical density at which the dark-state polariton density saturates. The atomic density at which correlations become important is when $\langle N_{\rm ph}\rangle = 1$, which for our experimental parameters corresponds to $n_{\rm crit} \approx 1 \times 10^{12}$ cm^{-3}. According to this simple model we find $Q \approx \mathcal{D}\exp(-n/n_{\rm crit}) - \mathcal{D}$, which is in closer agreement with the data (dashed line in Fig. 6.4 (c)), confirming the development of photon number correlations within the cloud plays an important role on the dark-state polariton statistics.

For the largest densities we find the measured Q values increase again to super-Poissonian values. We have not yet identified the cause of this increase, but we note that it coincides with the point when the cloud becomes quasi-1D with respect to the Rydberg excitation which might modify the effects of interactions on the propagating light field. Alternatively it could be due to the presence of a small number of prompt ions which are produced by one of the ionization mechanisms discussed in the previous chapter. Even though their small number is below our detection sensitivity, their presence could dramatically affect the polariton statistics. Spurious ions could also be present in recent experiments studying the effects of Rydberg blockade on photon statistics [Dudin and Kuzmich, 2012; Peyronel *et al.*, 2012; Maxwell *et al.*, 2012] but to our knowledge their effects have not been investigated so far.

6.5 Interplay between atomic and photonic correlations

Our experiments provide a direct observation of strongly interacting dark-state polaritons realized using electromagnetically induced transparency in an ultracold Rydberg gas. Strong polariton–polariton interactions are observed through the density dependent optical response and the polariton counting statistics, which become significantly sub-Poissonian at high densities, reflecting the emergence of spatial and temporal correlations between polaritons. The method presented here in principle allows for studying the full polariton counting statistics, thereby also giving access to higher order correlations [Ates *et al.*, 2006]. Two-photon correlations have recently been observed in the second order intensity correlation function of light $g^{(2)}(\tau)$ retrieved from small Rydberg ensembles [Dudin and Kuzmich, 2012; Maxwell *et al.*, 2012], and via light propagation through dense atomic clouds [Peyronel *et al.*, 2012]. We point out however that in general there is no direct mapping between the correlations on the light field and the atomic correlations. For instance, in a dense but optically thin medium, excess photons may not be efficiently scattered out of the forward direction thereby washing out the $g^{(2)}$ contrast, despite the presence of strong atomic correlations. Alternatively, outside of the blockaded regime, spin-wave dephasing due to atomic interactions can alter the statistics of the emitted light [Dudin and Kuzmich, 2012; Dudin *et al.*, 2012a; Bariani *et al.*, 2012], even though the atomic correlations could remain nearly classical. A complete description of electromagnetically induced transparency in strongly interacting media remains a theoretically challenging problem [Peyronel *et al.*, 2012], therefore it is necessary to study both aspects and to provide more stringent tests to theoretical models. This in turn might enable new studies investigating the effects of quantum correlations between atoms and photons. Ultimately this would open an avenue to study new types of strongly interacting quantum gases [Chang *et al.*, 2008; Fleischhauer *et al.*, 2008; Nikoghosyan *et al.*, 2012] or to the realization of on-demand sources of single photons and other nonclassical states of light [Honer *et al.*, 2011; Petrosyan *et al.*, 2011; Pritchard *et al.*, 2012] which would by major step in the direction of Rydberg based all-optical quantum information processing [Friedler *et al.*, 2005; Han *et al.*, 2010].

Chapter 7

Conclusion and outlook

In the scope of this thesis, I have investigated the effects of strong interactions between Rydberg atoms and their application to vastly different research areas which reaches well beyond the field of Rydberg physics. These studies were made possible by a completely new experimental setup which was designed for Rydberg physics in dense ultracold gases. Among the special features is a 2D-MOT, which serves as an ion free high flux source of cold atoms. Another key element of the setup is an optimized three beam optical dipole trap, which is composed of a large reservoir trap confining up to 5×10^6 Rubidium atoms and a dimple trap for forced evaporative cooling. It is a powerful tool for the rapid and efficient production of dense atomic samples and Bose-Einstein condensates. A specially designed electrode assembly is used to precisely control external electric fields and to field ionize Rydberg atoms for subsequent single ion sensitive detection. This detection technique has been complemented by optical probing of Rydberg states via electromagnetically induced transparency and both techniques have been applied either separately or in combination to give unprecedented access to macroscopic and microscopic properties of strongly interacting Rydberg ensembles.

With the new level of control enabled by the new experimental apparatus, it has been possible to investigate different applications of long-ranged Rydberg interactions as a means to imprint and control correlations in many-body systems. Experimental evidence of antiblockade in an ultracold Rydberg gas was given, which is a paradigm for the excellent control over interactions achievable with far off-resonant Rydberg excitation. It was demonstrated that this technique provides a powerful tool to impose spatial correlations on the excited atoms in an otherwise randomly arranged ultracold gas.

Afterwards the Rydberg blockade was employed as a tool to introduce spatial correlations in a dense, repulsively interacting Rydberg gas. Despite the expected stability of this system, the gas was observed to undergo spontaneous avalanche ionization for atomic densities exceeding $\approx 10^{10}\,\mathrm{cm}^{-3}$, which leads to the formation of an ultracold plasma. When investigating the dynamics of this process, the Rydberg blockade was identified to cause a significant delay of the plasma onset. It was furthermore observed that the plasma forms on a timescale which is short compared to the typical atomic motion, therefore the initial spatial correlations are most likely preserved in the plasma phase. Strongly blockaded Rydberg gases might thus provide a new route to mitigate disorder-induced heating, putting the production of strongly coupled ultracold plasmas within reach.

In the last study the back-action of Rydberg–Rydberg interactions on propagating light fields was studied. To this end we investigated both light and matter aspects of dissipatively interacting Rydberg dark-state polaritons. Our experiments covered over three orders of magnitude in atomic density which were used to observe the nonlinear optical response and the transition to sub-Poissonian polariton statistics when entering the strong interaction regime. By using a state-of-the-art theoretical approach we could show that the atomic correlations are significantly stronger than can be accounted for by assuming the propagation of classical light fields alone. This indicates that the recently observed modification to photon statistics due to Rydberg interactions [Peyronel *et al.*, 2012] can cause a significant back-action on the Rydberg atom statistics.

Rydberg atoms hold great potential for creating new many-body systems. For instance, the Rydberg EIT system in the strong interaction regime opens up other intriguing prospects of future research, since it has many features in common with cavity quantum electrodynamics systems [McKeever *et al.*, 2004; Birnbaum *et al.*, 2005; Dayan *et al.*, 2008; Tanji-Suzuki *et al.*, 2011]. The collectively enhanced response of a Rydberg ensemble to the probe field mimics that of a single atom strongly coupled to a cavity [Pritchard *et al.*, 2012]. This could pave the way for quantum non-demolition measurements of optical photons or — extended to larger ensembles — offer a new platform to study the physics of strongly coupled quantum-optical systems [Hartmann *et al.*, 2006; Greentree *et al.*, 2006] without the requirement of optical cavities.

Our polariton experiments can also be interpreted as Rydberg dressing of photons, in which photon–photon interactions are mediated by the Rydberg state admixture. By detuning from the intermediate state, the dissipative character of the polariton–polariton interactions could be suppressed while maintaining the huge nonlinearities which would give rise to elastic scattering, providing means to implement deterministic quantum logic gates [Shahmoon *et al.*, 2011; Gorshkov *et al.*, 2011]. As the nonlinearity can be controlled via the choice of the Rydberg state, repulsive, attractive and long-range interactions become possible [Sevinçli *et al.*, 2011b]. This could pave the way to create and study new types of quantum gases such as dipolar Bose-Einstein condensates of dark-state polaritons [Fleischhauer *et al.*, 2008; Nikoghosyan *et al.*, 2012]. In a similar fashion, Rydberg atoms could also be used to imprint new types of interactions to gases of ground state atoms by weakly admixing Rydberg character with laser light [Santos *et al.*, 2000; Pupillo *et al.*, 2010]. The resulting dressed states possess soft-core interactions, which in the repulsive case might enable the engineering of new types of quantum gases and strongly correlated phases of matter such as supersolid droplet crystals [Cinti *et al.*, 2010], supersolid vortex crystals [Henkel *et al.*, 2012] or roton excitations in Rydberg dressed Bose-Einstein condensates [Henkel *et al.*, 2010]. Exploiting attractive interactions, three-dimensional self-trapping of matter waves could be explored [Maucher *et al.*, 2011].

A future goal will be to explore some of these correlated phases at the level of single particles. With this in mind we have proposed a new imaging technique, which is based on our new understanding of electromagnetically induced transparency in interacting Rydberg gases [Günter *et al.*, 2012]. This method would make it possible to image individual impurities with high spatial and time resolution. The basic idea is to exploit the strong interactions between impurity atoms and a background gas of atoms coupled to an auxiliary Rydberg state via an EIT resonance. Associated with this is a new characteristic radius within which the impurity–probe interactions break the EIT condition, thereby changing the optical properties for many atoms surrounding each impurity. The potential of this new imaging scheme is illustrated in Fig. 7.1 which compares two *calculated* absorption images of a quasi-two-dimensional Rydberg gas. While Fig. 7.1 (a) depicts a conventional absorption image, Fig. 7.1 (b) clearly shows that spatial correlations between Rydberg atoms become visible when simultaneously applying the coupling laser. While having a lower level of technical sophistication than ‘quantum gas microscopes’ [Bakr *et al.*, 2009; Schauß *et al.*, 2012] this technique can be implemented in current cold atom experiments and is furthermore non-destructive, thus allowing for time-resolved images of many-body states. Numerous applications of the EIT imaging method can be foreseen, for example the possibility to directly image antiblockaded atom pairs or to observe the dynamical crystallization in the dipole blockade of ultracold atoms recently predicted by [Pohl *et al.*, 2010; Schachenmayer *et al.*, 2010; van Bijnen *et al.*, 2011]. Other studies could aim at spatially resolving individual dark-state

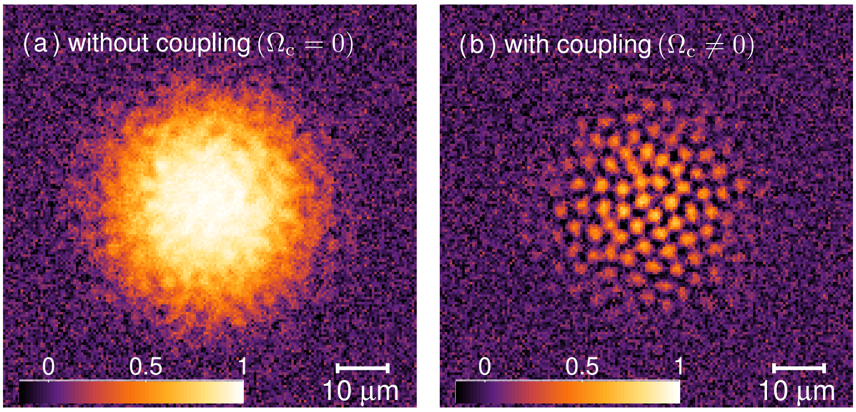

Figure 7.1: Interaction enhanced imaging of individual Rydberg atoms in a dense gas. *Simulated* absorption images of atom distributions including photon shot noise and atomic density fluctuations. In (a), without the coupling beam, a regular absorption image of the bath atoms is obtained. The color code indicates absorption. With the coupling on (b) the bath atoms are rendered transparent, except for those in the vicinity of a Rydberg atom.

polaritons propagating through the EIT medium and to directly reveal the nonlocal character of the dissipative polariton interactions. The technique is also sensitive to ionic impurities, since local Stark shifts can likewise disrupt the EIT condition for the bath atoms. This way it could serve as a powerful tool to image ionic correlations in ultracold plasmas, which would be an unmistakable signature for the strongly coupled plasma phase.

Ultimately, the ability to exploit Rydberg–Rydberg interactions to control both light and atomic fields, and to image the resulting new quantum phases will open a new chapter of Rydberg physics with many new and intriguing possibilities.

Bibliography

[Abel *et al.*, 2009] Abel, R. P., Mohapatra, A. K., Bason, M. G., Pritchard, J. D., Weatherill, K. J., Raitzsch, U., and Adams, C. S. (2009). *Laser frequency stabilization to excited state transitions using electromagnetically induced transparency in a cascade system.* Appl. Phys. Lett **94**, 071107.

[Aikawa *et al.*, 2012] Aikawa, K., Frisch, A., Mark, M., Baier, S., Rietzler, A., Grimm, R., and Ferlaino, F. (2012). *Bose-Einstein Condensation of Erbium.* Phys. Rev. Lett. **108**, 210401.

[Alzetta *et al.*, 1976] Alzetta, G., Gozzini, A., Moi, L., and Orriols, G. (1976). *An experimental method for the observation of r.f. transitions and laser beat resonances in oriented Na vapour.* Il Nuovo Cimento B **36**, 5.

[Amthor, 2008] Amthor, T. (2008). *Interaction-Induced Dynamics in Ultracold Rydberg Gases — Mechanical Effects and Coherent Processes.* PhD thesis Fakultät für Mathematik und Physik; Albert-Ludwigs-Universität Freiburg.

[Amthor *et al.*, 2010] Amthor, T., Giese, C., Hofmann, C. S., and Weidemüller, M. (2010). *Evidence of Antiblockade in an Ultracold Rydberg Gas.* Phys. Rev. Lett. **104**, 013001.

[Amthor *et al.*, 2007a] Amthor, T., Reetz-Lamour, M., Giese, C., and Weidemüller, M. (2007a). *Modeling many-particle mechanical effects of an interacting Rydberg gas.* Phys. Rev. A **76**, 054702.

[Amthor *et al.*, 2009] Amthor, T., Reetz-Lamour, M., and Weidemüller, M. (2009). *Cold Atoms and Molecules: Concepts, Experiments and Applications to Fundamental Physics* chapter Frozen Rydberg gases, , pp. 147 – 174. Wiley-VCH.

[Amthor *et al.*, 2007b] Amthor, T., Reetz-Lamour, M., Westermann, S., Denskat, J., and Weidemüller, M. (2007b). *Mechanical Effect of van der Waals Interactions*

Observed in Real Time in an Ultracold Rydberg Gas. Phys. Rev. Lett. **98**, 023004.

[Anderson *et al.*, 1995] Anderson, M. H., Ensher, J. R., Matthews, M. R., Wieman, C. E., and Cornell, E. A. (1995). *Observation of Bose-Einstein Condensation in a Dilute Atomic Vapor.* Science **269**, 198.

[Anderson *et al.*, 1998] Anderson, W. R., Veale, J. R., and Gallagher, T. F. (1998). *Resonant Dipole-Dipole Energy Transfer in a Nearly Frozen Rydberg Gas.* Phys. Rev. Lett. **80**, 249.

[Anisimov *et al.*, 2011] Anisimov, P. M., Dowling, J. P., and Sanders, B. C. (2011). *Objectively Discerning Autler-Townes Splitting from Electromagnetically Induced Transparency.* Phys. Rev. Lett. **107**, 163604.

[Arimondo, 1996] Arimondo, E. (1996). *Coherent Population Trapping in Laser Spectroscopy.* Prog. in Optics **35**, 259.

[Arimondo and Orriols, 1976] Arimondo, E. and Orriols, G. (1976). *Non-absorbing atomic coherences by coherent two-photon transition in a three-level optical pumping.* Nuovo Cimento **17**, 333.

[Ashkin, 1978] Ashkin, A. (1978). *Trapping of Atoms by Resonance Radiation Pressure.* Phys. Rev. Lett. **40**, 729.

[Ates, 2009] Ates, C. (2009). *Anregungsdynamik ultrakalter Rydberggase.* PhD thesis Institut für Theoretische Physik Fakultät Mathematik und Naturwissenschaften Technische Universität Dresden.

[Ates and Lesanovsky, 2012] Ates, C. and Lesanovsky, I. (2012). *Entropic enhancement of spatial correlations in a laser-driven Rydberg gas.* Phys. Rev. A **86**, 013408.

[Ates *et al.*, 2006] Ates, C., Pohl, T., Pattard, T., and Rost, J. M. (2006). *Strong interaction effects on the atom counting statistics of ultracold Rydberg gases.* J. Phys. B **39**, L233.

[Ates *et al.*, 2007a] Ates, C., Pohl, T., Pattard, T., and Rost, J. M. (2007a). *Antiblockade in Rydberg Excitation of an Ultracold Lattice Gas.* Phys. Rev. Lett. **98**, 023002.

[Ates *et al.*, 2007b] Ates, C., Pohl, T., Pattard, T., and Rost, J. M. (2007b). *Many-body theory of excitation dynamics in an ultracold Rydberg gas.* Phys. Rev. A **76**, 013413.

[Ates *et al.*, 2011] Ates, C., Sevinçli, S., and Pohl, T. (2011). *Electromagnetically induced transparency in strongly interacting Rydberg gases.* Phys. Rev. A **83**, 041802.

[Autler and Townes, 1955] Autler, S. H. and Townes, C. H. (1955). *Stark Effect in Rapidly Varying Fields.* Phys. Rev. **100**, 703.

[Bajcsy *et al.*, 2003] Bajcsy, M., Zibrov, A. S., and Lukin, M. D. (2003). *Stationary pulses of light in an atomic medium.* Nature **426**, 638.

[Bakr *et al.*, 2009] Bakr, W. S., Gillen, J. I., Peng, A., Fölling, S., and Greiner, M. (2009). *A quantum gas microscope for detecting single atoms in a Hubbard-regime optical lattice.* Nature **462**, 74.

[Balmer, 1885] Balmer, J. J. (1885). *Notiz über die Spektrallinien des Wasserstoffs.* Ann. Phys. Chem. **25**, 80.

[Barbier and Cheret, 1987] Barbier, L. and Cheret, M. (1987). *Experimental study of Penning and Hornbeck-Molnar ionisation of rubidium atoms excited in a high s or d level ($5d \leq nl \leq 11s$).* Journal of Physics B Atomic Molecular Physics **20**, 1229.

[Bariani *et al.*, 2012] Bariani, F., Dudin, Y. O., Kennedy, T. A. B., and Kuzmich, A. (2012). *Dephasing of Multiparticle Rydberg Excitations for Fast Entanglement Generation.* Phys. Rev. Lett. **108**, 030501.

[Bellac *et al.*, 2004] Bellac, M. L., Mortessagne, F., and Batrouni, G. G. (2004). *Equilibrium and Non-Equilibrium Statistical Thermodynamics.* Cambridge University Press.

[Benvenuti *et al.*, 1999] Benvenuti, C., Cazeneuve, J., Chiggiato, P., Cicoira, F., Santana, A. E., Johanek, V., Ruzinov, V., and Fraxedas, J. (1999). *A novel route to extreme vacua: the non-evaporable getter thin film coatings.* Vacuum **53**, 219 .

[Bergeson *et al.*, 2011] Bergeson, S. D., Denning, A., Lyon, M., and Robicheaux, F. (2011). *Density and temperature scaling of disorder-induced heating in ultracold plasmas.* Phys. Rev. A **83**, 023409.

[Bergmann *et al.*, 1998] Bergmann, K., Theuer, H., and Shore, B. (1998). *Coherent population transfer among quantum states of atoms and molecules.* Rev. Mod. Phys. **70**, 1003.

[Beterov *et al.*, 2009a] Beterov, I. I., Ryabtsev, I. I., Tretyakov, D. B., and Entin, V. M. (2009a). *Quasiclassical calculations of blackbody-radiation-induced depopulation rates and effective lifetimes of Rydberg nS, nP, and nD alkali-metal atoms with* $n <= 80$. Phys. Rev. A **79**, 052504.

[Beterov *et al.*, 2007] Beterov, I. I., Tretyakov, D. B., Ryabtsev, I. I., Ekers, A., and Bezuglov, N. N. (2007). *Ionization of sodium and rubidium nS, nP, and nD Rydberg atoms by blackbody radiation.* Phys. Rev. A **75**, 052720.

[Beterov *et al.*, 2009b] Beterov, I. I., Tretyakov, D. B., Ryabtsev, I. I., Entin, V. M., Ekers, A., and Bezuglov, N. N. (2009b). *Ionization of Rydberg atoms by blackbody radiation.* New J. Phys. **11**, 013052.

[Birnbaum *et al.*, 2005] Birnbaum, K. M., Boca, A., Miller, R., Boozer, A. D., Northup, T. E., and Kimble, H. J. (2005). *Photon blockade in an optical cavity with one trapped atom.* Nature **436**, 87.

[Bloch *et al.*, 2008] Bloch, I., Dalibard, J., and Zwerger, W. (2008). *Many-body physics with ultracold gases.* Rev. Mod. Phys. **80**, 885.

[Bohr, 1913] Bohr, N. (1913). *On the Constitution of Atoms and Molecules.* Phil. Mag. **26**, 1.

[Boisseau *et al.*, 2002] Boisseau, C., Simbotin, I., and Côté, R. (2002). *Macrodimers: Ultralong Range Rydberg Molecules.* Phys. Rev. Lett. **88**, 133004.

[Bradley *et al.*, 1995] Bradley, C. C., Sackett, C. A., Tollett, J. J., and Hulet, R. G. (1995). *Evidence of Bose-Einstein Condensation in an Atomic Gas with Attractive Interactions.* Phys. Rev. Lett. **75**, 1687.

[Breyel *et al.*, 2012] Breyel, D., Schmidt, T. L., and Komnik, A. (2012). *Rydberg crystallization detection by statistical means.* Phys. Rev. A **86**, 023405.

[Busche, 2011] Busche, H. (2011). *Efficient loading of a magneto-optical trap for experiments with dense ultracold Rydberg gases.* Diploma thesis Department of Physics and Astronomy, University of Heidelberg.

[Carnahan and Starling, 1969] Carnahan, N. F. and Starling, K. E. (1969). *Equation of State for Nonattracting Rigid Spheres.* J. Chem. Phys. **51**, 635.

[Carpenter *et al.*, 2012] Carpenter, D. T., Wood, C. S., Lyngnes, O., and Traggis, N. G. (2012). *Ultra low absorption glasses and optical coatings for reduced thermal focus shift in high power optics.* SPIE Proceedings **8239**.

[Castin and Dum, 1996] Castin, Y. and Dum, R. (1996). *Bose-Einstein Condensates in Time Dependent Traps.* Phys. Rev. Lett. **77**, 5315.

[Castro *et al.*, 2010] Castro, J., McQuillen, P., and Killian, T. C. (2010). *Ion Acoustic Waves in Ultracold Neutral Plasmas.* Phys. Rev. Lett. **105**, 065004.

[Catani *et al.*, 2006] Catani, J., Maioli, P., Sarlo, L. D., Minardi, F., and Inguscio, M. (2006). *Intense slow beams of bosonic potassium isotopes.* Phys. Rev. A **73**, 033415.

[Chang *et al.*, 2008] Chang, D. E., Gritsev, V., Morigi, G., Vuletić, V., Lukin, M. D., and Demler, E. A. (2008). *Crystallization of strongly interacting photons in a nonlinear optical fibre.* Nature Physics **4**, 884.

[Chaudhuri *et al.*, 2006] Chaudhuri, S., Roy, S., and Unnikrishnan, C. S. (2006). *Realization of an intense cold Rb atomic beam based on a two-dimensional magneto-optical trap: Experiments and comparison with simulations.* Phys. Rev. A **74**, 023406.

[Choi *et al.*, 2006] Choi, J.-H., Knuffman, B., Liebisch, T. C., Reinhard, A., and Raithel, G. (2006). *Cold Rydberg Atoms.* Adv. At. Mol. Opt. Phys. **54**, 131.

[Chu, 1998] Chu, S. (1998). *Nobel Lecture: The manipulation of neutral particles.* Rev. Mod. Phys. **70**, 685.

[Cinti *et al.*, 2010] Cinti, F., Jain, P., Boninsegni, M., Micheli, A., Zoller, P., and Pupillo, G. (2010). *Supersolid Droplet Crystal in a Dipole-Blockaded Gas.* Phys. Rev. Lett. **105**, 135301.

[Clément *et al.*, 2009] Clément, J. F., Brantut, J. P., de Saint-Vincent, M. R., Nyman, R. A., Aspect, A., Bourdel, T., and Bouyer, P. (2009). *All-optical runaway evaporation to Bose-Einstein condensation.* Phys. Rev. A **79**, 061406.

[Cohen-Tannoudji, 1996] Cohen-Tannoudji, C. (1996). *Amazing Light: A Volume Dedicated To Charles Hard Townes On His 80th Birthday* chapter The Autler-Townes effect revisited. Springer.

[Cohen-Tannoudji, 1998] Cohen-Tannoudji, C. N. (1998). *Nobel Lecture: Manipulating atoms with photons.* Rev. Mod. Phys. **70**, 707.

[Comparat and Pillet, 2010] Comparat, D. and Pillet, P. (2010). *Dipole blockade in a cold Rydberg atomic sample.* J. Opt. Soc. Am. B **27**, A208.

[Couvert *et al.*, 2008] Couvert, A., Jeppesen, M., Kawalec, T., Reinaudi, G., Mathevet, R., and Guéry-Odelin, D. (2008). *A quasi-monomode guided atom laser from an all-optical Bose-Einstein condensate.* EPL (Europhysics Letters) **83**, 50001.

[Cubel Liebisch *et al.*, 2005] Cubel Liebisch, T., Reinhard, A., Berman, P. R., and Raithel, G. (2005). *Atom Counting Statistics in Ensembles of Interacting Rydberg Atoms.* Phys. Rev. Lett. **95**, 253002.

[Cummings *et al.*, 2005] Cummings, E. A., Daily, J. E., Durfee, D. S., and Bergeson, S. D. (2005). *Fluorescence Measurements Of Expanding Strongly Coupled Neutral Plasmas.* Phys. Rev. Lett. **95**, 235001.

[Davis *et al.*, 1995] Davis, K. B., Mewes, M. O., Andrews, M. R., van Druten, N. J., Durfee, D. S., Kurn, D. M., and Ketterle, W. (1995). *Bose-Einstein Condensation in a Gas of Sodium Atoms.* Phys. Rev. Lett. **75**, 3969.

[Dayan *et al.*, 2008] Dayan, B., Parkins, A. S., Aoki, T., Ostby, E. P., Vahala, K. J., and Kimble, H. J. (2008). *A Photon Turnstile Dynamically Regulated by One Atom.* Science **319**, 1062.

[Deiglmayr *et al.*, 2006] Deiglmayr, J., Reetz-Lamour, M., Amthor, T., Westermann, S., de Oliveira, A. L., and Weidemüller, M. (2006). *Coherent excitation of Rydberg atoms in an ultracold gas.* Opt. Comm. **264**, 293.

[DeMarco and Jin, 1999] DeMarco, B. and Jin, D. S. (1999). *Onset of Fermi Degeneracy in a Trapped Atomic Gas.* Science **285**, 1703.

[Dicke, 1954] Dicke, R. H. (1954). *Coherence in Spontaneous Radiation Processes.* Phys. Rev. **93**, 99.

[Dieckmann *et al.*, 1998] Dieckmann, K., Spreeuw, R. J. C., Weidemüller, M., and Walraven, J. T. M. (1998). *Two-dimensional magneto-optical trap as a source of slow atoms.* Phys. Rev. A **58**, 3891.

[Dubessy *et al.*, 2012] Dubessy, R., Merloti, K., Longchambon, L., Pottie, P.-E., Liennard, T., Perrin, A., Lorent, V., and Perrin, H. (2012). *Rubidium-87 Bose-Einstein condensate in an optically plugged quadrupole trap.* Phys. Rev. A **85**, 013643.

[Dudin *et al.*, 2012a] Dudin, Y. O., Bariani, F., and Kuzmich, A. (2012a). *Emergence of Spatial Spin-Wave Correlations in a Cold Atomic Gas.* Phys. Rev. Lett. **109**, 133602.

[Dudin and Kuzmich, 2012] Dudin, Y. O. and Kuzmich, A. (2012). *Strongly Interacting Rydberg Excitations of a Cold Atomic Gas.* Science **336**, 887.

[Dudin *et al.*, 2012b] Dudin, Y. O., Li, L., Bariani, F., and Kuzmich, A. (2012b). *Observation of coherent many-body Rabi oscillations.* Nature Physics **8**, 790.

[Faber, 2011] Faber, A. (2011). *All-optical formation of a rubidium Bose-Einstein condensate for experiments on interacting Rydberg atoms.* Diploma thesis Department of Physics and Astronomy, University of Heidelberg.

[Fano, 1961] Fano, U. (1961). *Effects of Configuration Interaction on Intensities and Phase Shifts.* Phys. Rev. **124**, 1866.

[Fleischhauer and Lukin, 2000] Fleischhauer, M. and Lukin, M. D. (2000). *Dark-State Polaritons in Electromagnetically Induced Transparency.* Phys. Rev. Lett. **84**, 5094.

[Fleischhauer *et al.*, 2005] Fleischhauer, M., Imamoglu, A., and Marangos, J. P. (2005). *Electromagnetically induced transparency: Optics in coherent media.* Rev. Mod. Phys. **77**, 633.

[Fleischhauer and Lukin, 2002] Fleischhauer, M. and Lukin, M. D. (2002). *Quantum memory for photons: Dark-state polaritons.* Phys. Rev. A **65**, 022314.

[Fleischhauer *et al.*, 2008] Fleischhauer, M., Otterbach, J., and Unanyan, R. G. (2008). *Bose-Einstein Condensation of Stationary-Light Polaritons.* Phys. Rev. Lett. **101**, 163601.

[Fletcher *et al.*, 2006] Fletcher, R. S., Zhang, X. L., and Rolston, S. L. (2006). *Observation of Collective Modes of Ultracold Plasmas.* Phys. Rev. Lett. **96**, 105003.

[Fletcher *et al.*, 2007] Fletcher, R. S., Zhang, X. L., and Rolston, S. L. (2007). *Using Three-Body Recombination to Extract Electron Temperatures of Ultracold Plasmas.* Phys. Rev. Lett. **99**, 145001.

[Friedler *et al.*, 2005] Friedler, I., Petrosyan, D., Fleischhauer, M., and Kurizki, G. (2005). *Long-range interactions and entanglement of slow single-photon pulses.* Phys. Rev. A **72**, 043803.

[Gaëtan *et al.*, 2009] Gaëtan, A., Miroshnychenko, Y., Wilk, T., Chotia, A., Viteau, M., Comparat, D., Pillet, P., Browaeys, A., and Grangier, P. (2009). *Observation of collective excitation of two individual atoms in the Rydberg blockade regime.* Nature Physics **5**, 115.

[Gallagher and Pritchard, 1989] Gallagher, A. and Pritchard, D. E. (1989). *Exoergic Collisions of Cold Na*-Na.* Phys. Rev. Lett. **63**, 957.

[Gallagher, 2008] Gallagher, T. F. (2008). *Rydberg Atoms.* Cambridge University Press.

[Gallagher and Pillet, 2008] Gallagher, T. F. and Pillet, P. (2008). *Dipole–Dipole Interactions of Rydberg Atoms.* Advances In Atomic, Molecular, and Optical Physics **56**, 161.

[Gallagher *et al.*, 2003] Gallagher, T. F., Pillet, P., Robinson, M. P., Laburthe-Tolra, B., and Noel, M. W. (2003). *Back and forth between Rydberg atoms and ultracold plasmas.* J. Opt. Soc. Am. B **20**, 1091.

[Gallagher *et al.*, 1982] Gallagher, T. F., Safinya, K. A., Gounand, F., Delpech, J. F., Sandner, W., and Kachru, R. (1982). *Resonant Rydberg-atom–Rydbert-atom collisions.* Phys. Rev. A **25**, 1905.

[Gärttner *et al.*, 2012] Gärttner, M., Heeg, K. P., Gasenzer, T., and Evers, J. (2012). *Dynamical formation of floating Rydberg excitation crystals.* arXiv:1203.2884.

[Gericke and Murillo, 2003] Gericke, D. O. and Murillo, M. S. (2003). *Disorder-induced heating of ultracold plasmas.* Contributions to Plasma Physics **43**, 298.

[Gorshkov *et al.*, 2011] Gorshkov, A. V., Otterbach, J., Fleischhauer, M., Pohl, T., and Lukin, M. D. (2011). *Photon-Photon Interactions via Rydberg Blockade.* Phys. Rev. Lett. **107**, 133602.

[Götz *et al.*, 2012] Götz, S., Höltkemeier, B., Hofmann, C. S., Litsch, D., DePaola, B. D., and Weidemüller, M. (2012). *Versatile cold atom target apparatus.* Rev. Sci. Inst. **83**, 073112.

[Gounand, 1979] Gounand, F. (1979). *Calculation of radial matrix elements and radiative lifetimes for highly excited states of alkali atoms using the Coulomb approximation.* J. Phys. France **40**, 457.

[Gray *et al.*, 1978] Gray, H., Whitley, R. M., and Jr, C. S. (1978). *Coherent trapping of atomic populations.* Optics letters **3**, 218.

[Greentree *et al.*, 2006] Greentree, A. D., Tahan, C., Cole, J. H., and Hollenberg, L. C. L. (2006). *Quantum phase transitions of light.* Nature Physics **2**, 856 .

[Greiner *et al.*, 2002] Greiner, M., Mandel, O., Esslinger, T., Hänsch, T. W., and Bloch, I. (2002). *Quantum phase transition from a superfluid to a Mott insulator in a gas of ultracold atom.* Nature **415**, 39.

[Griesmaier *et al.*, 2005] Griesmaier, A., Werner, J., Hensler, S., Stuhler, J., and Pfau, T. (2005). *Bose-Einstein Condensation of Chromium.* Phys. Rev. Lett. **94**, 160401.

[Grimm *et al.*, 2000] Grimm, R., Weidemüller, M., and Ovchinnikov, Y. B. (2000). *Optical Dipole Traps for Neutral Atoms.* Advances In Atomic, Molecular, and Optical Physics **42**, 95.

[Günter *et al.*, 2012] Günter, G., de Saint-Vincent, M. R., Schempp, H., Hofmann, C. S., Whitlock, S., and Weidemüller, M. (2012). *Interaction Enhanced Imaging of Individual Rydberg Atoms in Dense Gases.* Phys. Rev. Lett. **108**, 013002.

[Gurian *et al.*, 2012] Gurian, J. H., Cheinet, P., Huillery, P., Fioretti, A., Zhao, J., Gould, P. L., Comparat, D., and Pillet, P. (2012). *Observation of a Resonant Four-Body Interaction in Cold Cesium Rydberg Atoms.* Phys. Rev. Lett. **108**, 023005.

[Han *et al.*, 2006] Han, J., Jamil, Y., Norum, D. V., Tanner, P. J., and Gallagher, T. F. (2006). *Rb nf quantum defects from millimeter-wave spectroscopy of cold* ^{85}*Rb Rydberg atoms.* Phys. Rev. A **74**, 054502.

[Han *et al.*, 2010] Han, Y., He, B., Heshami, K., Li, C.-Z., and Simon, C. (2010). *Quantum repeaters based on Rydberg-blockade-coupled atomic ensembles.* Phys. Rev. A **81**, 052311.

[Haroche and Raimond, 2006] Haroche, S. and Raimond, J.-M. (2006). *Exploring the Quantum: Atoms, Cavities, and Photons.* Oxford University Press.

[Harris, 1997] Harris, S. E. (1997). *Electromagnetically Induced Transparency.* Physics Today **50**, 36.

[Harris *et al.*, 1990] Harris, S. E., Field, J. E., and Imamoglu, A. (1990). *Nonlinear optical processes using electromagnetically induced transparency.* Phys. Rev. Lett. **64**, 1107.

[Hartmann *et al.*, 2006] Hartmann, M. J., Brandao, F. G. S. L., and Plenio, M. B. (2006). *Strongly interacting polaritons in coupled arrays of cavities.* Nature Physics **2**, 849.

[Hattermann *et al.*, 2012] Hattermann, H., Mack, M., Karlewski, F., Jessen, F., Cano, D., and Fortágh, J. (2012). *Detrimental adsorbate fields in experiments with cold Rydberg gases near surfaces.* Phys. Rev. A **86**, 022511.

[Hau *et al.*, 1999] Hau, L. V., Harris, S. E., Dutton, Z., and Behroozi, C. H. (1999). *Light speed reduction to 17 metres per second in an ultracold atomic gas.* Nature **397**, 594.

[Heeg *et al.*, 2012] Heeg, K. P., Gärttner, M., and Evers, J. (2012). *A hybrid model for Rydberg gases including exact two-body correlations.* arXiv:1202.2779.

[Heidemann *et al.*, 2007] Heidemann, R., Raitzsch, U., Bendkowsky, V., Butscher, B., Löw, R., Santos, L., and Pfau, T. (2007). *Evidence for Coherent Collective Rydberg Excitation in the Strong Blockade Regime.* Phys. Rev. Lett. **99**, 163601.

[Henkel *et al.*, 2012] Henkel, N., Cinti, F., Jain, P., Pupillo, G., and Pohl, T. (2012). *Supersolid Vortex Crystals in Rydberg-Dressed Bose-Einstein Condensates.* Phys. Rev. Lett. **108**, 265301.

[Henkel *et al.*, 2010] Henkel, N., Nath, R., and Pohl, T. (2010). *Three-Dimensional Roton Excitations and Supersolid Formation in Rydberg-Excited Bose-Einstein Condensates.* Phys. Rev. Lett. **104**, 195302.

[Hertz, 1909] Hertz, P. (1909). *Über den gegenseitigen durchschnittlichen Abstand von Punkten, die mit bekannter mittlerer Dichte im Raume angeordnet sind.* Math. Ann. **67**, 387.

[Hofmann *et al.*, 2012] Hofmann, C. S., Günter, G., Schempp, H., Robert de Saint Vincent, M., Gärttner, M., Evers, J., Whitlock, S., and Weidemüller, M. (2012). *Sub-Poissonian statistics of Rydberg-interacting dark-state polaritons.* arXiv:1211.7265.

[Höltkemeier, 2011] Höltkemeier, B. (2011). *2D-MOT as a source of a cold atom target.* Diploma thesis Department of Physics and Astronomy University of Heidelberg.

[Honer *et al.*, 2011] Honer, J., Löw, R., Weimer, H., Pfau, T., and Büchler, H. P. (2011). *Artificial Atoms Can Do More Than Atoms: Deterministic Single Photon Subtraction from Arbitrary Light Fields.* Phys. Rev. Lett. **107**, 093601.

[Horn, 1991] Horn, H. M. V. (1991). *Dense Astrophysical Plasmas.* Science **252**, 384.

[Ichimaru, 1982] Ichimaru, S. (1982). *Strongly coupled plasmas: high-density classical plasmas and degenerate electron liquids.* Rev. Mod. Phys. **54**, 1017.

[Jacob *et al.*, 2011] Jacob, D., Mimoun, E., Sarlo, L. D., Weitz, M., Dalibard, J., and Gerbier, F. (2011). *Production of sodium Bose-Einstein condensates in an optical dimple trap.* New Journal of Physics **13**, 065022.

[Jastrow, 1948] Jastrow, R. (1948). *On the Rydberg-Ritz Formula in Quantum Mechanics.* Phys. Rev. **73**, 60.

[Karpa and Weitz, 2006] Karpa, L. and Weitz, M. (2006). *A Stern–Gerlach experiment for slow light.* Nature Physics **2**, 332.

[Ketterle and van Druten, 1996] Ketterle, W. and van Druten, N. J. (1996). *Evaporative cooling of atoms.* Advances in Atomic, Molecular, and Optical Physics **37**, 181.

[Killian, 2007] Killian, T. C. (2007). *Ultracold Neutral Plasmas.* Science **316**, 705.

[Killian *et al.*, 2003] Killian, T. C., Ashoka, V. S., Gupta, P., Laha, S., Nagel, S. B., Simien, C. E., Kulin, S., Rolston, S. L., and Bergeson, S. D. (2003). *Ultracold neutral plasmas: recent experiments and new prospects.* Journal of Physics A: Mathematical and General **36**, 6077.

[Killian *et al.*, 1999] Killian, T. C., Kulin, S., Bergeson, S. D., Orozco, L. A., Orzel, C., and Rolston, S. L. (1999). *Creation of an Ultracold Neutral Plasma.* Phys. Rev. Lett. **83**, 4776.

[Killian *et al.*, 2001] Killian, T. C., Lim, M. J., Kulin, S., Dumke, R., Bergeson, S. D., and Rolston, S. L. (2001). *Formation of Rydberg Atoms in an Expanding Ultracold Neutral Plasma.* Phys. Rev. Lett. **86**, 3759.

[Killian *et al.*, 2007] Killian, T. C., Pattard, T., Pohl, T., and Rost, J. M. (2007). *Ultracold Neutral Plasmas.* Physics Reports **449**, 77.

[Kinoshita *et al.*, 2004] Kinoshita, T., Wenger, T., and Weiss, D. S. (2004). *Observation of a One-Dimensional Tonks-Girardeau Gas.* Science **305**, 1125.

[Knuffman and Raithel, 2006] Knuffman, B. and Raithel, G. (2006). *Emission of fast atoms from a cold Rydberg gas.* Phys. Rev. A **73**, 020704(R).

[Kübler *et al.*, 2010] Kübler, H., Shaffer, J. P., Baluktsian, T., Löw, R., and Pfau, T. (2010). *Coherent Excitation of Rydberg Atoms in Thermal Vapor Microcells.* Nature Photonics **4**, 112.

[Kumar *et al.*, 1999] Kumar, A., Sahaa, B. C., Weatherforda, C. A., and Vermab, S. K. (1999). *A systematic study of Hornbeck Molnar ionization involving Rydberg alkali atoms.* Journal of Molecular Structure Theochem **487**, 1.

[Kuppens *et al.*, 2000] Kuppens, S. J. M., Corwin, K. L., Miller, K. W., Chupp, T. E., and Wieman, C. E. (2000). *Loading an optical dipole trap.* Phys. Rev. A **62**, 013406.

[Kuzmin and O'Neil, 2002a] Kuzmin, S. G. and O'Neil, T. M. (2002a). *Numerical simulation of ultracold plasmas.* Physics of Plasmas **9**, 3743.

[Kuzmin and O'Neil, 2002b] Kuzmin, S. G. and O'Neil, T. M. (2002b). *Numerical Simulation of Ultracold Plasmas: How Rapid Intrinsic Heating Limits the Development of Correlation.* Phys. Rev. Lett. **88**, 065003.

[Lauber *et al.*, 2011] Lauber, T., Küber, J., Wille, O., and Birkl, G. (2011). *Optimized Bose-Einstein-condensate production in a dipole trap based on a 1070-nm multifrequency laser: Influence of enhanced two-body loss on the evaporation process.* Phys. Rev. A **84**, 043641.

[Li *et al.*, 2003] Li, W., Mourachko, I., Noel, M. W., and Gallagher, T. F. (2003). *Millimeter-wave spectroscopy of cold Rb Rydberg atoms in a magneto-optical trap: Quantum defects of the ns, np, and nd series.* Phys. Rev. A **67**, 052502.

[Li *et al.*, 2004] Li, W., Noel, M. W., Robinson, M. P., Tanner, P. J., Gallagher, T. F., Comparat, D., Tolra, B. L., Vanhaecke, N., Vogt, T., Zahzam, N., and Pillet, P. (2004). *Evolution dynamics of a dense frozen Rydberg gas to plasma.* Phys. Rev. A **70**, 042713.

[Li *et al.*, 2005] Li, W., Tanner, P. J., and Gallagher, T. F. (2005). *Dipole-Dipole Excitation and Ionization in an Ultracold Gas of Rydberg Atoms.* Phys. Rev. Lett. **94**, 173001.

[Lindblad, 1976] Lindblad, G. (1976). *On the generators of quantum dynamical semigroups.* Communications in Mathematical Physics **48**, 119.

[Liu *et al.*, 2001] Liu, C., Dutton, Z., Behroozi, C. H., and Hau, L. V. (2001). *Observation of coherent optical information storage in an atomic medium using halted light pulses.* Nature **409**, 490.

[Löw *et al.*, 2007] Löw, R., Raitzsch, U., Heidemann, R., Bendkowsky, V., Butscher, B., Grabowski, A., and Pfau, T. (2007). *Apparatus for excitation and detection of Rydberg atoms in quantum gases.* arXiv:0706.2639.

[Lu *et al.*, 2011] Lu, M., Burdick, N. Q., Youn, S. H., and Lev, B. L. (2011). *Strongly Dipolar Bose-Einstein Condensate of Dysprosium.* Phys. Rev. Lett. **107**, 190401.

[Lukin *et al.*, 2001] Lukin, M. D., Fleischhauer, M., Côté, R., Duan, L. M., Jaksch, D., Cirac, J. I., and Zoller, P. (2001). *Dipole Blockade and Quantum Information Processing in Mesoscopic Atomic Ensembles.* Phys. Rev. Lett. **87**, 037901.

[Lukin and Imamoglu, 2001] Lukin, M. D. and Imamoglu, A. (2001). *Controlling photons using electromagnetically induced transparency.* Nature **413**, 273.

[Mandel, 1979] Mandel, L. (1979). *Sub-Poissonian photon statistics in resonance fluorescence.* Optics Letters **4**, 205.

[Marangos, 1998] Marangos, J. P. (1998). *Electromagnetically induced transparency.* J. Mod. Opt. **45**, 471.

[Maucher *et al.*, 2011] Maucher, F., Henkel, N., Saffman, M., Królikowski, W., Skupin, S., and Pohl, T. (2011). *Rydberg-Induced Solitons: Three-Dimensional Self-Trapping of Matter Waves.* Phys. Rev. Lett. **106**, 170401.

[Maxwell *et al.*, 2012] Maxwell, D., Szwer, D., Barato, D. P., Busche, H., Pritchard, J. D., Gauguet, A., Weatherill, K. J., Jones, M. P. A., and Adams, C. S. (2012). *Quantum state control of stored optical photons.* arXiv:1207.6007.

[Mazets and Matisov, 1996] Mazets, I. E. and Matisov, B. G. (1996). *Adiabatic Raman polariton in a Bose condensate.* JETP Letters **64**, 515.

[McKeever *et al.*, 2004] McKeever, J., Boca, A., Boozer, A. D., Miller, R., Buck, J. R., Kuzmich, A., and Kimble, H. J. (2004). *Deterministic Generation of Single Photons from One Atom Trapped in a Cavity.* Science **303**, 1992.

[McQuillen *et al.*, 2012] McQuillen, P., Zhang, X., Strickler, T., Dunning, F. B., and Killian, T. C. (2012). *Imaging the evolution of an ultracold strontium Rydberg gas.* arXiv:1211.3450.

[Mohapatra *et al.*, 2008] Mohapatra, A. K., Bason, M. G., Butscher, B., Weatherill, K. J., and Adams, C. S. (2008). *A giant electro-optic effect using polarizable dark states.* Nature Physics **4**, 890.

[Mohapatra *et al.*, 2007] Mohapatra, A. K., Jackson, T. R., and Adams, C. S. (2007). *Coherent Optical Detection of Highly Excited Rydberg States Using Electromagnetically Induced Transparency.* Phys. Rev. Lett. **98**, 113003.

[Møller *et al.*, 2008] Møller, D., Madsen, L. B., and Mølmer, K. (2008). *Quantum Gates and Multiparticle Entanglement by Rydberg Excitation Blockade and Adiabatic Passage.* Phys. Rev. Lett. **100**, 170504.

[Morrison *et al.*, 2008] Morrison, J. P., Rennick, C. J., Keller, J. S., and Grant, E. R. (2008). *Evolution from a Molecular Rydberg Gas to an Ultracold Plasma in a Seeded Supersonic Expansion of NO.* Phys. Rev. Lett. **101**, 205005.

[Mourachko *et al.*, 1998] Mourachko, I., Comparat, D., de Tomasi, F., Fioretti, A., Nosbaum, P., Akulin, V. M., and Pillet, P. (1998). *Many-Body Effects in a Frozen Rydberg Gas.* Phys. Rev. Lett. **80**, 253.

[Mülken *et al.*, 2007] Mülken, O., Blumen, A., Amthor, T., Giese, C., Reetz-Lamour, M., and Weidemüller, M. (2007). *Survival Probabilities in Coherent Exciton Transfer with Trapping.* Phys. Rev. Lett. **99**, 090601.

[Müller *et al.*, 2009] Müller, M., Lesanovsky, I., Weimer, H., Büchler, H. P., and Zoller, P. (2009). *Mesoscopic Rydberg Gate Based on Electromagnetically Induced Transparency.* Phys. Rev. Lett. **102**, 170502.

[Müller, 2010] Müller, N. L. M. (2010). *Excitation and detection of Rydberg atoms in an ultracold gas — Electric field design and electromagnetically induced transparency.* Diploma thesis Department of Physics and Astronomy, University of Heidelberg.

[Murillo, 2001] Murillo, M. S. (2001). *Using Fermi Statistics to Create Strongly Coupled Ion Plasmas in Atom Traps.* Phys. Rev. Lett. **87**, 115003.

[Nikoghosyan *et al.*, 2012] Nikoghosyan, G., Zimmer, F. E., and Plenio, M. B. (2012). *Dipolar Bose-Einstein condensate of dark-state polaritons.* Phys. Rev. A **86**, 023854.

[Nipper *et al.*, 2012] Nipper, J., Balewski, J. B., Krupp, A. T., Hofferberth, S., Löw, R., and Pfau, T. (2012). *Atomic Pair-State Interferometer: Controlling and Measuring an Interaction-Induced Phase Shift in Rydberg-Atom Pairs.* Phys. Rev. X **2**, 031011.

[Ockeloen *et al.*, 2010] Ockeloen, C. F., Tauschinsky, A. F., Spreeuw, R. J. C., and Whitlock, S. (2010). *Detection of small atom numbers through image processing.* Phys. Rev. A **82**, 061606.

[O'Hara *et al.*, 2001] O'Hara, K. M., Gehm, M. E., Granade, S. R., and Thomas, J. E. (2001). *Scaling laws for evaporative cooling in time-dependent optical traps.* Phys. Rev. A **64**, 051403.

[Olmos *et al.*, 2011] Olmos, B., Li, W., Hofferberth, S., and Lesanovsky, I. (2011). *Amplifying single impurities immersed in a gas of ultracold atoms.* Phys. Rev. A **84**, 041607.

[Olson, 1979] Olson, R. (1979). *Ionization Cross Sections For Rydberg-Atom–Rydberg-Atom Collisions.* Phys. Rev. Lett. **43**, 126.

[Opatrný and Mølmer, 2012] Opatrný, T. c. v. and Mølmer, K. (2012). *Spin squeezing and Schrödinger-cat-state generation in atomic samples with Rydberg blockade.* Phys. Rev. A **86**, 023845.

[Osterwalder and Merkt, 1999] Osterwalder, A. and Merkt, F. (1999). *Using High Rydberg States as Electric Field Sensors.* Phys. Rev. Lett. **82**, 1831.

[O'Sullivan and Stoicheff, 1985] O'Sullivan, M. S. and Stoicheff, B. P. (1985). *Scalar polarizabilities and avoided crossings of high Rydberg states in Rb.* Phys. Rev. A **31**, 2718.

[O'Sullivan and Stoicheff, 1986] O'Sullivan, M. S. and Stoicheff, B. P. (1986). *Scalar and tensor polarizabilities of* ^{2}D *Rydberg states in Rb.* Phys. Rev. A **33**, 1640.

[Overstreet *et al.*, 2009] Overstreet, K. R., Schwettmann, A., Tallant, J., Booth, D., and Shaffer, J. P. (2009). *Observation of electric-field-induced Observation of electric-field-induced Cs Rydberg atom macrodimers.* Nature Physics **5**, 581.

[Paredes *et al.*, 2004] Paredes, B., Widera, A., Murg, V., Mandel, O., Fölling, S., Cirac, I., Shlyapnikov, G. V., Hänsch, T. W., and Bloch, I. (2004). *Tonks-Girardeau gas of ultracold atoms in an optical lattice.* Nature **429**, 277.

[Parigi *et al.*, 2012] Parigi, V., Bimbard, E., Stanojevic, J., Hilliard, A. J., Nogrette, F., Tualle-Brouri, R., Ourjoumtsev, A., and Grangier, P. (2012). *Observation and Measurement of Interaction-Induced Dispersive Optical Nonlinearities in an Ensemble of Cold Rydberg Atoms.* Phys. Rev. Lett. **109**, 233602.

[Parisi and Zamponi, 2010] Parisi, G. and Zamponi, F. (2010). *Mean-field theory of hard sphere glasses and jamming.* Rev. Mod. Phys. **82**, 789.

[Percival and Richards, 1975] Percival, I. C. and Richards, D. (1975). *The Theory of Collisions between Charged Particles and Highly Excited Atoms* Vol. 11 of *Advances in Atomic and Molecular Physics.* Academic Press London.

[Petrosyan and Fleischhauer, 2008] Petrosyan, D. and Fleischhauer, M. (2008). *Quantum Information Processing with Single Photons and Atomic Ensembles in Microwave Coplanar Waveguide Resonators.* Phys. Rev. Lett. **100**, 170501.

[Petrosyan *et al.*, 2011] Petrosyan, D., Otterbach, J., and Fleischhauer, M. (2011). *Electromagnetically Induced Transparency with Rydberg Atoms.* Phys. Rev. Lett. **107**, 213601.

[Peyronel *et al.*, 2012] Peyronel, T., Firstenberg, O., Liang, Q. Y., Hofferberth, S., Gorshkov, A. V., Pohl, T., Lukin, M. D., and Vuletić, V. (2012). *Quantum nonlinear optics with single photons enabled by strongly interacting atoms.* Nature **488**, 57.

[Phillips *et al.*, 2001] Phillips, D. F., Fleischhauer, A., Mair, A., Walsworth, R. L., and Lukin, M. D. (2001). *Storage of Light in Atomic Vapor.* Phys. Rev. Lett. **86**, 783.

[Phillips, 1998] Phillips, W. D. (1998). *Nobel Lecture: Laser cooling and trapping of neutral atoms.* Rev. Mod. Phys. **70**, 721.

[Pillet *et al.*, 2009] Pillet, P., Vogt, T., Viteau, M., Chotia, A., Zhao, J., Comparat, D., Gallagher, T., Tate, D., Gaëtan, A., Miroshnychenko, Y., et al. (2009). *Controllable interactions between Rydberg atoms and ultracold plasmas.* Journal of Physics: Conference Series **194**, 012066.

[Pohl *et al.*, 2010] Pohl, T., Demler, E., and Lukin, M. D. (2010). *Dynamical Crystallization in the Dipole Blockade of Ultracold Atoms.* Phys. Rev. Lett. **104**, 043002.

[Pohl *et al.*, 2004a] Pohl, T., Pattard, T., and Rost, J. M. (2004a). *Kinetic modeling and molecular dynamics simulation of ultracold neutral plasmas including ionic correlations.* Phys. Rev. A **70**, 033416.

[Pohl *et al.*, 2004b] Pohl, T., Pattard, T., and Rost, J. M. (2004b). *On the possibility of 'correlation cooling' of ultracold neutral plasmas.* J. Phys. B **37**, L183.

[Pritchard, 2012] Pritchard, J. D. (2012). *Cooperative Optical Non-Linearity in a Blockaded Rydberg Ensemble.* Springer Theses.

[Pritchard *et al.*, 2010] Pritchard, J. D., Maxwell, D., Gauguet, A., Weatherill, K. J., Jones, M. P. A., and Adams, C. S. (2010). *Cooperative Atom-Light Interaction in a Blockaded Rydberg Ensemble.* Phys. Rev. Lett. **105**, 193603.

[Pritchard *et al.*, 2012] Pritchard, J. D., Weatherill, K. J., and Adams, C. S. (2012). *Non-linear optics using cold Rydberg atoms.* arXiv:1205.4890.

[Pupillo *et al.*, 2010] Pupillo, G., Micheli, A., Boninsegni, M., Lesanovsky, I., and Zoller, P. (2010). *Strongly Correlated Gases of Rydberg-Dressed Atoms: Quantum and Classical Dynamics.* Phys. Rev. Lett. **104**, 223002.

[Raab *et al.*, 1987] Raab, E. L., Prentiss, M., Cable, A., Chu, S., and Pritchard, D. E. (1987). *Trapping of Neutral Sodium Atoms with Radiation Pressure.* Phys. Rev. Lett. **59**, 2631.

[Raitzsch *et al.*, 2009] Raitzsch, U., Heidemann, R., Weimer, H., Butscher, B., Kollmann, P., Löw, R., Büchler, H. P., and Pfau, T. (2009). *Investigation of dephasing rates in an interacting Rydberg gas.* New J. Phys. **11**, 055014.

[Ramirez-Serrano *et al.*, 2006] Ramirez-Serrano, J., Yu, N., Kohel, J. M., Kellogg, J. R., and Maleki, L. (2006). *Multistage two-dimensional magneto-optical trap as a compact cold atom source.* Opt. Lett. **31**, 682.

[Rebollo-Neira and Lowe, 2002] Rebollo-Neira, L. and Lowe, D. (2002). *Optimized Orthogonal Matching Pursuit Approach.* Signal Processing Letters, IEEE **9**, 137.

[Reetz-Lamour *et al.*, 2008] Reetz-Lamour, M., Deiglmayr, J., Amthor, T., and Weidemüller, M. (2008). *Rabi oscillations between ground and Rydberg states and van der Waals blockade in a mesoscopic frozen Rydberg gas.* New J. Phys. **10**, 045026.

[Reinhard *et al.*, 2007] Reinhard, A., Liebisch, T. C., Knuffman, B., and Raithel, G. (2007). *Level shifts of rubidium Rydberg states due to binary interactions.* Phys. Rev. A **75**, 032712.

[Reinhard *et al.*, 2008a] Reinhard, A., Liebisch, T. C., Younge, K. C., Berman, P. R., and Raithel, G. (2008a). *Rydberg-Rydberg Collisions: Resonant Enhancement of State Mixing and Penning Ionization.* Phys. Rev. Lett. **100**, 123007.

[Reinhard *et al.*, 2008b] Reinhard, A., Younge, K. C., and Raithel, G. (2008b). *Effect of Foerster resonances on the excitation statistics of many-body Rydberg systems.* Phys. Rev. A **78**, 060702(R).

[Remington *et al.*, 1999] Remington, B. A., Arnett, D., Paul, R., Drake, and Takabe, H. (1999). *Modeling Astrophysical Phenomena in the Laboratory with Intense Lasers.* Science **284**, 1488.

[Robert de Saint Vincent *et al.*, 2012] Robert de Saint Vincent, M., Hofmann, C. S., Schempp, H., Günter, G., Whitlock, S., and Weidemüller, M. (2012). *Spontaneous avalanche ionization of a strongly blockaded Rydberg gas.* arXiv:1209.4728.

[Robicheaux, 2005] Robicheaux, F. (2005). *Ionization due to the interaction between two Rydberg atoms.* J. Phys. B **38**, S333.

[Robicheaux and Hanson, 2002] Robicheaux, F. and Hanson, J. D. (2002). *Simulation of the Expansion of an Ultracold Neutral Plasma.* Phys. Rev. Lett. **88**, 055002.

[Robicheaux and Hernández, 2005] Robicheaux, F. and Hernández, J. V. (2005). *Many-body wave function in a dipole blockade configuration.* Phys. Rev. A **72**, 063403.

[Robinson *et al.*, 2000] Robinson, M. P., Tolra, B. L., Noel, M. W., Gallagher, T. F., and Pillet, P. (2000). *Spontaneous Evolution of Rydberg Atoms into an Ultracold Plasma.* Phys. Rev. Lett. **85**, 4466.

[Roman and Majlis, 1983] Roman, E. and Majlis, N. (1983). *Computer simulation model of the structure of ion implanted impurities in semiconductors.* Solid State Communications **47**, 259.

[Ryabtsev *et al.*, 2007] Ryabtsev, I. I., Tretyakov, D. B., Beterov, I. I., and Entin, V. M. (2007). *Effect of finite detection efficiency on the observation of the dipole-dipole interaction of a few Rydberg atoms.* Phys. Rev. A **76**, 012722.

[Ryabtsev *et al.*, 2010] Ryabtsev, I. I., Tretyakov, D. B., Beterov, I. I., and Entin, V. M. (2010). *Observation of the Stark-Tuned Förster Resonance between Two Rydberg Atoms.* Phys. Rev. Lett. **104**, 073003.

[Rydberg, 1890] Rydberg, J. R. (1890). *Recherches sur la constitution des spectres d'émission des éléments chimiques.* Norstedt.

[Saffman *et al.*, 2010] Saffman, M., Walker, T. G., and Mølmer, K. (2010). *Quantum information with Rydberg atoms.* Rev. Mod. Phys. **82**, 2313.

[Santos *et al.*, 2000] Santos, L., Shlyapnikov, G. V., Zoller, P., and Lewenstein, M. (2000). *Bose-Einstein Condensation in Trapped Dipolar Gases.* Phys. Rev. Lett. **85**, 1791.

[Santra *et al.*, 2005] Santra, R., Arimondo, E., Ido, T., Greene, C. H., and Ye, J. (2005). *High-Accuracy Optical Clock via Three-Level Coherence in Neutral Bosonic* ^{88}Sr. Phys. Rev. Lett. **94**, 173002.

[Saquet *et al.*, 2011] Saquet, N., Morrison, J. P., Schulz-Weiling, M., Sadeghi, H., Yiu, J., Rennick, C. J., and Grant, E. R. (2011). *On the formation and decay of a molecular ultracold plasma.* Journal of Physics B: Atomic, Molecular and Optical Physics **44**, 184015.

[Schachenmayer *et al.*, 2010] Schachenmayer, J., Lesanovsky, I., Micheli, A., and Daley, A. J. (2010). *Dynamical crystal creation with polar molecules or Rydberg atoms in optical lattices.* New Journal of Physics **12**, 103044.

[Schauß *et al.*, 2012] Schauß , P., Cheneau, M., Endres, M., Fukuhara, T., Hild, S., Omran, A., Pohl, T., Gross, C., Kuhr, S., and Bloch, I. (2012). *Observation of spatially ordered structures in a two-dimensional Rydberg gas.* Nature **491**, 87.

[Schempp *et al.*, 2010] Schempp, H., Günter, G., Hofmann, C. S., Giese, C., Saliba, S. D., DePaola, B. D., Amthor, T., Weidemüller, M., Sevinçli, S., and Pohl, T. (2010).

Coherent Population Trapping with Controlled Interparticle Interactions. Phys. Rev. Lett. **104**, 173602.

[Schnellbächer, 2010] Schnellbächer, N. D. (2010). *A compact setup for frequency stabilization of diode lasers.* Diploma thesis Department of Physics and Astronomy, University of Heidelberg.

[Schoser *et al.*, 2002] Schoser, J., Batär, A., Löw, R., Schweikhard, V., Grabowski, A., Ovchinnikov, Y. B., and Pfau, T. (2002). *Intense source of cold Rb atoms from a pure two-dimensional magneto-optical trap.* Phys. Rev. A **66**, 023410.

[Schwarzkopf *et al.*, 2011] Schwarzkopf, A., Sapiro, R. E., and Raithel, G. (2011). *Imaging Spatial Correlations of Rydberg Excitations in Cold Atom Clouds.* Phys. Rev. Lett. **107**, 103001.

[Sedlacek *et al.*, 2012] Sedlacek, J., Schwettmann, A., Kübler, H., Löw, R., Pfau, T., and Shaffer, J. P. (2012). *Microwave electrometry with Rydberg atoms in a vapour cell using bright atomic resonances.* Nature Physics **8**, 819.

[Sevinçli *et al.*, 2011a] Sevinçli, S., Ates, C., Pohl, T., Schempp, H., Hofmann, C. S., Günter, G., Amthor, T., Weidemüller, M., Pritchard, J. D., Maxwell, D., Gauguet, A., Weatherill, K. J., Jones, M. P. A., and Adams, C. S. (2011a). *Quantum interference in interacting three-level Rydberg gases: coherent population trapping and electromagnetically induced transparency.* J. Phys. B **44**, 184018.

[Sevinçli *et al.*, 2011b] Sevinçli, S., Henkel, N., Ates, C., and Pohl, T. (2011b). *Nonlocal Nonlinear Optics in Cold Rydberg Gases.* Phys. Rev. Lett. **107**, 153001.

[Shahmoon *et al.*, 2011] Shahmoon, E., Kurizki, G., Fleischhauer, M., and Petrosyan, D. (2011). *Strongly interacting photons in hollow-core waveguides.* Phys. Rev. A **83**, 033806.

[Shukla and Avinash, 2011] Shukla, P. K. and Avinash, K. (2011). *Phase Coexistence and a Critical Point in Ultracold Neutral Plasmas.* Phys. Rev. Lett. **107**, 135002.

[Simien *et al.*, 2004] Simien, C. E., Chen, Y. C., Gupta, P., Laha, S., Martinez, Y. N., Mickelson, P. G., Nagel, S. B., and Killian, T. C. (2004). *Using Absorption Imaging to Study Ion Dynamics in an Ultracold Neutral Plasma.* Phys. Rev. Lett. **92**, 143001.

[Singer *et al.*, 2004] Singer, K., Reetz-Lamour, M., Amthor, T., Marcassa, L. G., and Weidemüller, M. (2004). *Suppression of Excitation and Spectral Broadening Induced by Interactions in a Cold Gas of Rydberg Atoms.* Phys. Rev. Lett. **93**, 163001.

[Singer *et al.*, 2005] Singer, K., Stanojevic, J., Weidemüller, M., and Côté, R. (2005). *Long-range interactions between alkali Rydberg atom pairs correlated to the ns-ns, np-np and nd-nd asymptotes.* J. Phys. B **38**, S295.

[Stanojevic and Côté, 2010] Stanojevic, J. and Côté, R. (2010). *Many-body dynamics of Rydberg excitation using the Ω expansion.* Phys. Rev. A **81**, 053406.

[Stebbings and Dunning, 2011] Stebbings, R. F. and Dunning, F. B. (2011). *Rydberg States of Atoms and Molecules.* Cambridge University Press.

[Talbot *et al.*, 1991] Talbot, J., Schaaf, P., and Tarjus, G. (1991). *Random sequential addition of hard spheres.* Molecular Physics **72**, 1397.

[Tanji-Suzuki *et al.*, 2011] Tanji-Suzuki, H., Chen, W., Landig, R., Simon, J., and Vuletić, V. (2011). *Vacuum-Induced Transparency.* Science **333**, 1266.

[Tanner *et al.*, 2008] Tanner, P. J., Han, J., Shuman, E. S., and Gallagher, T. F. (2008). *Many-Body Ionization in a Frozen Rydberg Gas.* Phys. Rev. Lett. **100**, 043002.

[Tauschinsky *et al.*, 2010] Tauschinsky, A., Thijssen, R. M. T., Whitlock, S., van Linden van den Heuvell, H. B., and Spreeuw, R. J. C. (2010). *Spatially resolved excitation of Rydberg atoms and surface effects on an atom chip.* Phys. Rev. A **81**, 063411.

[Tiecke *et al.*, 2009] Tiecke, T. G., Gensemer, S. D., Ludewig, A., and Walraven, J. T. M. (2009). *High-flux two-dimensional magneto-optical-trap source for cold lithium atoms.* Phys. Rev. A **80**, 013409.

[Tong *et al.*, 2004] Tong, D., Farooqi, S. M., Stanojevic, J., Krishnan, S., Zhang, Y. P., Côté, R., Eyler, E. E., and Gould, P. L. (2004). *Local Blockade of Rydberg Excitation in an Ultracold Gas.* Phys. Rev. Lett. **93**, 063001.

[Townsend *et al.*, 1996] Townsend, C. G., Edwards, N. H., K.P.Zetie, Cooper, C. J., J.Rink, and C.J.Foot (1996). *High-density trapping of cesium atoms in a dark magneto-optical trap.* Phys. Rev. A **53**, 1702.

[Twedt and Rolston, 2012] Twedt, K. A. and Rolston, S. L. (2012). *Electronic Detection of Collective Modes of an Ultracold Plasma.* Phys. Rev. Lett. **108**, 065003.

[Urban *et al.*, 2009] Urban, E., Johnson, T. A., Henage, T., Isenhower, L., Yavuz, D. D., Walker, T. G., and Saffman, M. (2009). *Observation of Rydberg blockade between two atoms.* Nature Physics **5**, 110.

[van Bijnen *et al.*, 2011] van Bijnen, R. M. W., Smit, S., van Leeuwen, K. A. H., Vredenbregt, E. J. D., and Kokkelmans, S. J. J. M. F. (2011). *Adiabatic formation of Rydberg crystals with chirped laser pulses.* Journal of Physics B: Atomic, Molecular and Optical Physics **44**, 184008.

[van Ditzhuijzen *et al.*, 2008] van Ditzhuijzen, C. S. E., Koenderink, A. F., Hernàndez, J. V., Robicheaux, F., Noordam, L. D., and van Linden van den Heuvell, H. B. (2008). *Spatially Resolved Observation of Dipole-Dipole Interaction between Rydberg Atoms.* Phys. Rev. Lett. **100**, 243201.

[van Ditzhuijzen *et al.*, 2006] van Ditzhuijzen, C. S. E., Koenderink, A. F., Noordam, L. D., and van Linden van den Heuvell, H. B. (2006). *Simultaneous position and state measurement of Rydberg atoms.* Eur. Phys. J. D **40**, 13.

[Viteau *et al.*, 2012] Viteau, M., Huillery, P., Bason, M. G., Malossi, N., Ciampini, D., Morsch, O., Arimondo, E., Comparat, D., and Pillet, P. (2012). *Cooperative Excitation and Many-Body Interactions in a Cold Rydberg Gas.* Phys. Rev. Lett. **109**, 053002.

[Vitrant *et al.*, 1982] Vitrant, G., Raimond, J. M., Gross, M., and Haroche, S. (1982). *Rydberg to plasma evolution in a dense gas of very excited atoms.* J. Phys. B **15**, L49.

[Vogt *et al.*, 2007] Vogt, T., Viteau, M., Chotia, A., Zhao, J., Comparat, D., and Pillet, P. (2007). *Electric-Field Induced Dipole Blockade with Rydberg Atoms.* Phys. Rev. Lett. **99**, 073002.

[Vogt *et al.*, 2006] Vogt, T., Viteau, M., Zhao, J., Chotia, A., Comparat, D., and Pillet, P. (2006). *Dipole Blockade at Förster Resonances in High Resolution Laser Excitation of Rydberg States of Cesium Atoms.* Phys. Rev. Lett. **97**, 083003.

[Walker and Saffman, 2008] Walker, T. G. and Saffman, M. (2008). *Consequences of Zeeman degeneracy for the van der Waals blockade between Rydberg atoms.* Phys. Rev. A **77**, 032723.

[Walz-Flannigan *et al.*, 2004] Walz-Flannigan, A., Guest, J. R., Choi, J.-H., and Raithel, G. (2004). *Cold-Rydberg-gas dynamics.* Phys. Rev. A **69**, 063405.

[Weatherill *et al.*, 2008] Weatherill, K. J., Pritchard, J. D., Abel, R. P., Bason, M. G., Mohapatra, A. K., and Adams, C. S. (2008). *Electromagnetically induced transparency of an interacting cold Rydberg ensemble.* J. Phys. B **41**, 201002.

[Weber *et al.*, 2002] Weber, T., Herbig, J., Mark, M., Nägerl, H. C., and Grimm, R. (2002). *Bose-Einstein Condensation of Cesium.* Science **299**, 232.

[Weber *et al.*, 2012] Weber, T. M., Niederprüm, T., Manthey, T., Langer, P., Guarrera, V., Barontini, G., and Ott, H. (2012). *Continuous coupling of ultracold atoms to an ionic plasma via Rydberg excitation.* Phys. Rev. A **86**, 020702.

[Westermann *et al.*, 2006] Westermann, S., Amthor, T., de Oliveira, A. L., Deiglmayr, J., Reetz-Lamour, M., and Weidemüller, M. (2006). *Dynamics of resonant energy transfer in a cold Rydberg gas.* Eur. Phys. J. D **40**, 37.

[Wüster *et al.*, 2010] Wüster, S., Stanojevic, J., Ates, C., Pohl, T., Deuar, P., Corney, J. F., and Rost, J. M. (2010). *Correlations of Rydberg excitations in an ultracold gas after an echo sequence.* Phys. Rev. A **81**, 023406.

[Zaiser *et al.*, 2011] Zaiser, M., Hartwig, J., Schlippert, D., Velte, U., Winter, N., Lebedev, V., Ertmer, W., and Rasel, E. M. (2011). *Simple method for generating Bose-Einstein condensates in a weak hybrid trap.* Phys. Rev. A **83**, 035601.

Acknowledgements

Besonderer Dank gilt meinem Betreuer Prof. Dr. **Matthias Weidemüller**, der mir neben einem interessanten Promotionsthema und einem hervorragenden Forschungsumfeld auch viele Einblicke in die internationale Forschung gegeben hat. Besonders habe ich mich über die vielen Gestaltungsmöglichkeiten gefreut, die du mir im Rahmen meiner Doktorarbeit gegeben hast. Das große Vertrauen, das du mir entgegen gebracht hast und die Verantwortung, die du mir beim Planen und Bauen unseres neuen Experiments übertragen hast, waren für mich besonders motivierend.

Bei Prof. Dr. **Markus Oberthaler** möchte ich mich für die Zweitkorrektur dieser Arbeit und die Unterstützung bei der Bewerbung für das Abschlussstipendium der Graduiertenakademie bedanken.

Ich hatte das große Glück während meiner Doktorarbeit täglich mit wunderbaren Kollegen und Freunden zusammen zu arbeiten, die alle dazu beigetragen haben, dass neben der Physik auch die Chemie an unserem Experiment stimmt.

It has been a privilege to work with **Shannon Whitlock**. Your catching enthusiasm has always been a source of motivation. Your focus on the essential and your support have been a tremendous help.

I thank **Martin Robert-de-Saint-Vincent** for the fantastic collaboration on the plasma project. I appreciate your healthy skepticism and the gazillions of back-of-the-envelope calculations you made for us.

Bei **Thomas Amthor** möchte ich mich für die hervoragende Zusammenarbeit bedanken, die für mich sehr bereichernd war und von der ich viel profitieren konnte.

Hanna Schempp danke ich für die lustigen Jahre, die schon in Freiburg am alten Experiment begannen. Die gute Teamarbeit beim Entwerfen unseres Detektors hat mir sehr viel Spaß gemacht. Besonders dankbar bin ich dir für das stetige Optimieren der Experimentiersteuerung, ohne die wir keine der tollen Messungen hätten machen können.

Bei **Georg Günter** möchte ich mich für unvergessliche Alpentrips, schöne Feste und Kulturveranstaltungen bedanken, die immer tolle Abwechslungen zum arbeitsreichen Alltag boten und mich wieder Kraft für neue Herausforderungen tanken ließen. Besonders dankbar bin ich dir, dass du dich immer allen unsereren Elektronikproblemen angenommen und unsere Anregungslaser schick gemacht hast.

I am happy that my successor **Vladislav Gavryusev** recently joined our project and I hope that this thesis makes a small contribution to becoming acquainted with our experiment.

In den zurückliegenden Jahren haben viele talentierte Diplomanden an unserem Projekt mitgewirkt und damit zum Gelingen unserer Experimente beigetragen. **Nele Müller** danke ich für unzählige Iterationen beim Simulieren des Detektors. Bei **Hannes Busche** bedanke ich mich für die Zusammenarbeit beim Charakterisieren der 2D-MOT und bei **Aline Faber** für das Aufbauen der Dipolfalle. **Henning Labuhn** sei für das Konzipieren der Transfercavity gedankt, die unsere Anregungslaser bestimmt noch viel schmaler machen wird. Ich wünsche euch, dass ihr während eurer Doktorarbeiten mit genau so tollen Diplomanden zusammenarbeiten könnt.

Stephan Helmrich wünsche ich eine spannende Diplomarbeit. Dank gilt auch unseren Bachelorstudenten **Nikolas Schnellbächer** und **Maximilian Argus** sowie unseren Projektstudenten **Yang Yang** und **Stefan Mastel** für ihre Beiträge.

Marc Repp vom A(nderen)-Experiment danke ich für die tolle Zusammenarbeit und die vielen kreativen Ideen beim Konstruieren der neuen Maschinen. Und die Späßle bei dem ein oder anderen kühlen Blonden zum Wochenausklang sollen hier natürlich auch nicht unerwähnt bleiben. Bei **Juris Ulmanis** und **Rico Pires** bedanke ich mich für viele Elektronikentwicklungen, die auch in unserem Experiment hervorragende Dienste geleistet haben. Ein großes Dankeschön geht an **Bastian Höltkemeier** und **Simone Götz** für die gute Kooperation beim Entwickeln der 2D-MOT und für die eine oder andere Squashpartie. Unserer Sekretärin **Claudia Krämer** danke ich für die Hilfe beim Überspringen so mancher Bürokratiehürde. Den übrigen Mitgliedern unserer Arbeitsgruppe möchte ich für das immer gute Arbeitsklima danken.

Ein besonders schöner Aspekt der Promotion ist für mich der Wissensaustausch mit Kollegen gewesen, bei dem ich vieles lernen konnte. So bin ich für die bereichernden Theorie-Diskussionen mit **Thomas Pohl**, **Sevilay Sevinçli**, **Cenap Ates**, **Rick van Bijnen**, **Jörg Evers**, **Martin Gärttner** und **David Breyel** dankbar.

Special thanks go to Prof. Dr. **Brett DePaola** with whom I had fantastic times during his visits in Freiburg and Heidelberg.

Mein ganz großer Dank gilt der **mechanischen Werkstatt des Physikalischen Instituts** für ihre Unterstützung bei unserem Laborumzug nach Heidelberg und für das Fertigen hunderter maßgeschneiderter Bauteile für unser Experiment und dem damit verbundenen Meistern jeder noch so großen technischen Herausforderung. **Ralf Ziegler** danke ich für das Koordinieren all dieser Arbeiten. Insbesondere möchte ich hier die fantastische Unterstützung von **Dominic Litsch**, **Simon Rabenecker**, **Jessica Riedinger** und **Maximilian von Klot** erwähnen. Genauso dankbar bin ich für die vielen Konstruktionspläne von **Jürgen Gerhäuser**, **Kevin Stumpf** und Dr. **Bernd Windelband**. In unserer langen Zusammenarbeit konnte ich viel von euch lernen.

Eine Besonderheit an einer Promotion in Heidelberg ist das fantastische wissenschaftliche Umfeld, das einem durch die vielen Graduiertenschulen geboten wird: Der **HGSFP** und der **IMPRS-QD** danke ich für viele inspirierende Veranstaltungen. Besonders möchte ich dabei die finanzielle Unterstützung der **HGSFP** hervorheben, die mir die Teilnahme an der Sommerschule in Varenna und etliche Laborbesuche ermöglicht hat, die zum Gelingen dieser Arbeit beigetragen haben. Der **Graduiertenakademie der Universität Heidelberg** danke ich für das Abschlussstipendium, in der letzten Phase meiner Doktorarbeit, in der die in Kapitel 5 & 6 beschriebenen Experimente durchgeführt wurden. Zu großem Dank bin ich auch der **Studienstiftung des deutschen Volkes** verpflichtet, die mich mit einem Promotionsstipedium finanziell wie auch ideell gefördert hat.

Der größte Dank gilt meinen Eltern und meiner Schwester für unser wunderbares Familienleben und für ihr stetes Interesse an meinen Vorhaben. Eure grenzenlose Unterstützung schätzte ich sehr. Meiner Freundin Anne danke ich für unser schönes gemeinsames Leben, das mich zu einem so glücklichen Menschen macht.